In vivo diffusion tensor imaging (DTI) for the human heart under free-breathing conditions

Hongjiang Wei

Numéro d'ordre: 2013ISAL0127 **Année 2013**

THÈSE

présentée devant

L'Institut National des Sciences Appliquées de Lyon

pour obtenir

LE GRADE DE DOCTEUR

ÉCOLE DOCTORALE: ÉLECTRONIQUE, ÉLECTROTECHNIQUE, AUTOMATIQUE
FORMATION DOCTORALE : SCIENCES DE L'INFORMATION, DES DISPOSITIFS ET DES SYSTÈMES

par

WEI Hongjiang

In vivo diffusion tensor imaging (DTI) for the human heart under free-breathing conditions

Soutenue le 20 Novembre 2013

Jury :

Frédérique FROUIN	Chargé de Recherches INSERM/UPMC Paris	Rapporteur
Wanyu LIU	Professeur de HIT	Rapporteur
Pierre CROISILLE	Professeur CHU St-Etienne	Examinateur
Magalie VIALLON	MR physicist CHU St-Etienne	Examinateur
Jacques FELBLINGER	Professeur CHU Nancy	Examinateur
Nicolas ROUGON	Matire de Conférences TELECOM-SudParis	Examinateur
Yuemin ZHU	Directeur de Recherche CNRS	Directeur de thèse

INSA Direction de la Recherche

SIGLE	ECOLE DOCTORALE	NOM ET COORDONNEES DU RESPONSABLE
CHIMIE	**CHIMIE DE LYON** **http://www.edchimie-lyon.fr** Insa : R. GOURDON	M. Jean Marc LANCELIN Université de Lyon – Collège Doctoral Bât ESCPE 43 bd du 11 novembre 1918 69622 VILLEURBANNE Cedex Tél : 04.72.43 13 95 directeur@edchimie-lyon.fr
E.E.A.	**ELECTRONIQUE, ELECTROTECHNIQUE, AUTOMATIQUE** **http://edeea.ec-lyon.fr** Secrétariat : M.C. HAVGOUDOUKIAN eea@ec-lyon.fr	M. Gérard SCORLETTI Ecole Centrale de Lyon 36 avenue Guy de Collongue 69134 ECULLY Tél : 04.72.18 60 97 Fax : 04 78 43 37 17 Gerard.scorletti@ec-lyon.fr
E2M2	**EVOLUTION, ECOSYSTEME, MICROBIOLOGIE, MODELISATION** **http://e2m2.universite-lyon.fr** Insa : H. CHARLES	Mme Gudrun BORNETTE CNRS UMR 5023 LEHNA Université Claude Bernard Lyon 1 Bât Forel 43 bd du 11 novembre 1918 69622 VILLEURBANNE Cédex Tél : 04.72.43.12.94 e2m2@biomserv.univ-lyon1.fr
EDISS	**INTERDISCIPLINAIRE SCIENCES-SANTE** **http://ww2.ibcp.fr/ediss** Sec : Safia AIT CHALAL Insa : M. LAGARDE	M. Didier REVEL Hôpital Louis Pradel Bâtiment Central 28 Avenue Doyen Lépine 69677 BRON Tél : 04.72.68 49 09 Fax : 04 72 35 49 16 Didier.revel@creatis.uni-lyon1.fr
INFOMATHS	**INFORMATIQUE ET MATHEMATIQUES** **http://infomaths.univ-lyon1.fr**	M. Johannes KELLENDONK Université Claude Bernard Lyon 1 INFOMATHS Bâtiment Braconnier 43 bd du 11 novembre 1918 69622 VILLEURBANNE Cedex Tél : 04.72. 44.82.94 Fax 04 72 43 16 87 infomaths@univ-lyon1.fr
Matériaux	**MATERIAUX DE LYON** Secrétariat : M. LABOUNE PM : 71.70 –Fax : 87.12 Bat. Saint Exupéry **Ed.materiaux@insa-lyon.fr**	M. Jean-Yves BUFFIERE INSA de Lyon MATEIS Bâtiment Saint Exupéry 7 avenue Jean Capelle 69621 VILLEURBANNE Cédex Tél : 04.72.43 83 18 Fax 04 72 43 85 28 Jean-yves.buffiere@insa-lyon.fr
MEGA	**MECANIQUE, ENERGETIQUE, GENIE CIVIL, ACOUSTIQUE** Secrétariat : M. LABOUNE PM : 71.70 –Fax : 87.12 Bat. Saint Exupéry **mega@insa-lyon.fr**	M. Philippe BOISSE INSA de Lyon Laboratoire LAMCOS Bâtiment Jacquard 25 bis avenue Jean Capelle 69621 VILLEURBANNE Cedex Tél :04.72.43.71.70 Fax : 04 72 43 72 37 Philippe.boisse@insa-lyon.fr
ScSo	**ScSo*** M. OBADIA Lionel Sec : Viviane POLSINELLI Insa : J.Y. TOUSSAINT	M. OBADIA Lionel Université Lyon 2 86 rue Pasteur 69365 LYON Cedex 07 Tél : 04.78.69.72.76 Fax : 04.37.28.04.48 Lionel.Obadia@univ-lyon2.fr

- Écoles Doctorales – Quinquennal 2011-2015

In Vivo Diffusion Tensor Imaging for Cardiac Fibers of the Human Heart

Abstract

The orientation of cardiac fibers underlies the electro-mechanical behavior of the heart, and it is known to be altered in various cardiac diseases such as ischemic heart disease and ventricular hypertrophy. This thesis mainly focuses on in vivo diffusion tensor imaging (DTI) to obtain the myocardial fiber structure of the human heart under free-breathing conditions. The use of DTI for studying the human heart in vivo is challenging due to cardiac motion. In particular, free-breathing DTI acquisition without resorting to respiratory gating is very difficult due to both respiratory and cardiac motion. To deal with this problem, we propose novel approaches that combine multiple shifted trigger delay (TD) acquisitions and post-processing methods. First, we perform multiple shifted TD acquisitions at end diastole. Then, we focus on two different post-processing methods. The first method addresses physiological motion effects on in vivo cardiac DTI using image co-registration and PCATMIP (Principal Components Analysis filtering and Temporal Maximum Intensity Projection). The second method is a wavelet-based image fusion (WIF) algorithm combined with a PCA noise removing method. Finally, a comparison of DTI measurements between the PCATMIP and WIF methods is also performed; tensor fields are calculated, from which the in vivo fiber architecture properties are compared. The results show that using the proposed approaches, we are able to study the cardiac motion effects on diffusion tensor parameters, and investigate the underlying relationship between the measured diffusion tensor properties and the cardiac motion. We also find that the combination of multiple shifted TD acquisitions and dedicated image post-processing can compensate for physiological motion effects, which allows us to obtain 3D fiber architectures of the human heart under free-breathing conditions. The findings suggest new solutions to signal loss problems associated with bulk motion, which are promising for obtaining in vivo human myocardial fiber architecture properties in clinical conditions.

Résumé

L'orientation des fibres myocardiaque est à la base du comportement électro-mécanique du cœur, et connue pour être altérée dans diverses maladies cardiaques telles que la cardiopathie ischémique et l'hypertrophie ventriculaire. Cette thèse porte principalement sur l'imagerie in vivo du tenseur de diffusion (diffusion tensor imaging—DTI) en vue d'obtenir la structure des fibres myocardiques du cœur humain dans des conditions de respiration libre. L'utilisation de DTI pour l'étude du cœur humain in vivo est un grand défi en raison du mouvement cardiaque. En particulier, l'acquisition DTI avec respiration libre sans recourir au gating respiratoire est très difficile à cause des mouvements à a fois respiratoire et cardiaque. Pour aborder ce problème, nous proposons de nouvelles approches consistant à combiner des acquisitions à retards de déclenchement multiples (trigger delay—TD) et des méthodes de post-traitement. D'abord, nous réalisons des acquisitions avec multiples TD décalés en fin de diastole. Ensuite, nous développons deux méthodes de post-traitement. La première méthode s'attaque au problème d'effets de mouvement physiologique sur DTI cardiaque in vivo en utilisant les techniques de recalage et de PCATMIP (Principal Components Analysis filtering and Temporal Maximum Intensity Projection). La deuxième méthode traite le problème de mouvement par l'utilisation d'un algorithme de fusion d'images basé sur l'ondelette (wavelet-based image fusion-WIF) et d'une technique de débruitage PCA (Principal Components Analysis). Enfin, une comparaison des mesures DTI entre la méthode PCATMIP et la méthode WIF est réalisée ; les champs de tenseurs sont calculés, à partir desquels les propriétés de l'architecture des fibres in vivo sont comparées. Les résultats montrent qu'en utilisant les approches proposées, il est possible d'étudier l'impact du mouvement cardiaque sur les paramètres de tenseur de diffusion, et d'explorer les relations sous-jacentes entre les propriétés de tenseur de diffusion mesurées et le mouvement cardiaque. Nous trouvons aussi que la combinaison des acqusiitions avec des TD multiples décalés and des post-traitements d'images peut compenser les effets de mouvement physiologique, ce qui permet d'obtenir l'architecture 3D du cœur humain dans des conditions de respiration libre. Les résultats suggèrent de nouvelles solutions au problème de perte du signal due au mouvement, qui sont prometteuses pour obtenir les propriétés de l'architecture des fibres myocardiques du cœur humain in vivo, dans des conditions cliniques.

.

Remerciement

I am grateful for the past three years of my Ph.D. study in the laboratory CREATIS at INSA de Lyon. The excellent education and research environment in the institute has benefited me a lot. All I want to say is that the three years study constitutes the most precious wealth in my life.

I would like to express my sincere gratitude to my advisor Professor Yuemin Zhu. His extraordinary insightful and inspiring guidance, his continuous support and encouragement, are indispensable to the accomplishment of this thesis, which I can not express in words. He cultivates my appreciation for sciences, and shows me through his own life how to be a researcher for truth.

I thank Magalie Viallon and Pierre Croisille. Their inspiring guidance for this thesis and their continuous support are indispensable to the success. Their experiences in physical, medicine and MRI are an indispensable part for the success of this thesis.

I thank my colleagues Stan and Benedicte. Their experiences in the pulse programming and their supports are an indispensable part for the success of this project. I also appreciate their helps that familiarize me with the MR machine and data acquisitions.

I specially thank Professor Wanyu LIU and Frédérique FROUIN for reviewing my thesis and Professor Jacques FELBLINGER and Nicolas ROUGON accepting as the jury of my thesis.

I thank all my colleagues in the laboratory for their helps and companions during my life in France. I must thank my close and deep friends who gave me the courages to pursue the Ph.D. when times were darker.

I sincerely thank all my family for their endless love support and influence in my life that made the man I am today. My family is the greatest power for me to finish this thesis.

I would like to thank my dearest Yuyao for being very understanding and supportive during our life living in Lyon, France.

Thank you everyone, my Ph.D. is also yours!

Hongjiang WEI

是故聪与敏，可恃而不可恃也；自恃其聪与敏而不学者，自败者也。昏与庸，可限而不可限也；不自限其昏与庸而力学不倦者，自力者也。

-为学-

Hongjiang WEI

Contents

Introduction

Heart disease is a leading cause of death in the world. Cardiovascular disease (CVD) is caused by disorders of the heart and blood vessels, and includes coronary heart disease (heart attacks), cerebrovascular disease (stroke), raised blood pressure (hypertension), peripheral artery disease, rheumatic heart disease, congenital heart disease and heart failure. An estimated 17 million people die of CVDs every year, particularly heart attacks and strokes (World Health Organization). A substantial number of these deaths can be attributed to tobacco smoking, which increases the risk of dying from coronary heart disease and cerebrovascular disease 2-3 fold. Each year CVD causes over 4 million deaths in Europe and over 1.9 million deaths in the European Union (Oxford report). Due to their high mortality, heart disease became the most costly disease. According to the American Heart Association (AHA), all CVDs together were projected to cost $444.2 billion in 2010, including health care services, medications, and lost productivity. Therefore, from the point of view of health and economic opportunities, it is essential and important to develop techniques that allow a better understanding of the heart structure and function in order to prevent cardiac heart failure. MRI provides unique capabilities to investigate cardiac function and structure, and characterize myocardial tissue non-invasively.

Myocardial function is fundamentally linked to specific fiber architecture. The analysis of the structure of myocardial fibers is considered as an important factor in understanding the underlying disease and associated arrhythmias. This is due to the fact that the structural fibers is altered over time by various cardiomyopathies. In the healthy heart, it is generally accepted that cardiac muscle fibers or myofibers are arranged in spirals surrounding the ventricles and the orientation of the fibers depends on their transmural location. Recently, the study on the human atlas of cardiac fiber architecture on a healthy population has shown that the helix angle of the average fiber orientation is highly correlated to the transmural depth and ranges from -41° on the epicardium to +66° on the endocardium . In addition, myofibers are mainly organized in the bottom-up direction to the endocardial and epicardial surface and turn in a circumferential direction in the middle of the mid wall. This helical structure is responsible for the twisting motion of the left ventricle (LV) and main mechanical functions. Therefore, detailed 3D structures of myocardial fiber information can provide important clues for understanding the physiological and functional properties of the heart and for the diagnosis of heart diseases.

Our first understanding of the cardiac fiber architecture is derived from histological study on the interesting areas of the tissue. The histological techniques are known to suffer from distortion and misalignment, and it does not allow the 3D reconstruction of fibrous structures. To solve these problems, polarized light imaging (PLI) has been proposed for the fiber orientations in fetal ex vivo hearts (Jouk et al. 2007). It can provide a high spatial resolution with $0.1 \times 0.1 \times 0.5$ mm^3 3D orientation of myocardial fibers. Compared to dissection and histological methods, it is more objective because it does not involve any human operation

during the measurement process. However, both histological techniques and PLI are ex vivo and can not be used to study the fiber architecture of in vivo human heart.

Today, the magnetic resonance tensor imaging (DTI) (Basser et al. 1994b) is the only non-destructive and non-invasive way to observe the architecture of in vivo cardiac fibers and provides further guidance directly in 3D. Ex vivo cardiac DTI on fiber atlas study has been reported (Lombaert et al. 2012). However, the in vivo DTI is much more diffcult because of the bulk motion. The overall motion of the heart is a complex mixture of cardiac motion associated with its cyclic pumping and respiratory motion which results in an additional twisting and volumetric distortion. The respiratory motion is relatively unpredictable and can vary considerably from person to person and from time to time. A moving object will change both the phase and magnitude of its k-space components when we do the acquisitions. Motion during image acquisition will therefore introduce artefacts, and these can be divided into two categories, motion during the acquisition of one phase-encode line intra-view, and motion between different phase-encode lines inter-view. For most sequences, intra-view motion at typical myocardial and respiratory speeds can be ignored. Inter-view motion artefacts can be caused by cardiac motion or breathing motion and are very dependent on the nature of the motion in relation to the k-space coverage. First attempt to collect in vivo human diffusion data on the heart was achieved using a stimulated echo acquisition mode (STEAM) (Edelman et al. 1994). Cardiac diffusion imaging using a STEAM preparation presents the advantage of having much shorter scan time per RR interval, thus reducing the intrascan motion, but inherently doubles the total scan time compared to spin-echo sequences (Gamper et al. 2007) since encoding and decoding must take place in two consecutive cardiac cycles. The study (Reese et al. 1996) showed the feasibility of mapping fiber orientations quantitatively in human subjects; they found that cardiac DW imaging has a significant sensitivity to myocardial deformation due to the motion. The authors (Tseng et al. 2000) presented a method of obtaining accurate diffusion data by requiring an additional sequence measurement and defining a “sweet spot” in the cardiac cycle where the net effect of strain on the observed diffusion approximates zero. The authors in (Dou et al. 2009) developed a stimulated-echo acquisition mode technique for cardiac DW imaging in vivo, which has the major drawback of an inherently low signal-to-noise ratio (SNR) efficiency. In a spin echo approach with bipolar diffusion encoding gradient (Gamper et al. 2007) was proposed to make the sequence insensitive to systolic bulk motion of the heart. Several implementations (Edelman et al. 1994; Reese et al. 1996; Gamper et al. 2007) were used to compensate for motion induced signal loss including retrospective navigators and breath-holding, which required acquisition times of about 7 minutes per slice. In the majority of these studies, however, either a single (Tseng et al. 2000; Gamper et al. 2007; Dou et al. 2009) or three (Nielles-Vallespin et al. 2012) slices could be acquired. A 3D reconstruction of cardiac fiber architecture to derive in vivo human atlas using conformal mapping schemes (Toussaint et al. 2010) was proposed. Nevertheless, either three or five (Toussaint et al. 2013) slices are not adequate for the whole 3D fiber architecture reconstruction due to the low spatial resolution (6 or 8 mm slice thickness). The 3D cardiac fiber architecture construction using streamline would benefit from a higher number of slices.

The aim of this study is to investigate the feasibility of in vivo cardiac DTI and 3D fiber tracking of the entire heart under free-breathing conditions and without resorting to respiratory gating. Our method to tackle the motion issues is a special acquisition strategy combined with post-processing methods. To this end, motion-reduced in vivo cardiac DTI datasets were first acquired at end-diastole using a multiple shifted trigger delay (TD) acquisition strategy. Then a non-rigid registration method (Guetter et al. 2011) was used to correct interscan motion caused by respiration. Then two different post-processing methods were performed on the multiple-time-point DW images to compensate for the signal loss. One is the robust PCATMIP method (Pai et al. 2010; Delattre et al. 2012) based on principal component analysis (PCA) and temporal maximum intensity projection (TMIP). Actually, if we intend to apply this technique to clinical applications, we still need more accurate diffusion measurements. So we also need to quantify motion effects on diffusion parameters and to evaluate the accuracy of our motion correction method. In this study, we introduced a simulation study based on ex vivo heart acquired by PLI and in vivo motion data acquired by DENSE technique. Then at last, for the in vivo cardiac DTI, another method is developed that concerns the wavelet-based image fusion (WIF) combined with a PCA denoising method. The final corrected DW images were used to calculate the tensor field, from which the diffusion parameters such as fractional anisotropy (FA), mean diffusivity (MD), helix angle (HA), and in vivo fiber architecture (3D fiber tracts) were derived and compared.

The presentation of this thesis is organized as below.

The first part of this thesis is devoted to the presentation of medical foundations of cardiac imaging and methodology of our work:

Chapter 1 describes the concepts of anatomy and physiology of heart and the architectural organization of the human heart.

Chapter 2 describes in detail the cardiac imaging including the PLI processing scheme, the principle of magnetic resonance imaging and DTI. Then we discuss the current challenges of in vivo cardiac DTI about free-breathing acquisitions and long scan time.

The second part is dedicated to the simulation study and in vivo cardiac DTI contributions:

The work presented in Chapter 3 focuses on a simulation study about how heart motion affects diffusion parameters and therefore we can quantify motion effects on diffusion parameters and evaluate the accuracy of our motion correction method. In this simulation, first of all, we need to build a real model on the signal loss caused by motion. For this purpose, we acquire multiple phase diffusion images and DENSE images on 6 volunteers. Totally, we acquired 20 phases through the entire cardiac cycle. Using the two kinds of information, we can estimate signal loss as a function of the cardiac longitudinal displacement. Then, we calculate the average of the 6 curves. The average is based on sector calculation according to AHA segmentation of the LV. In this simulation study, the ground truth is the ex vivo heart acquired by PLI. Knowing the fiber orientation, we can derive simulated multiple directional DW images by Monte-Carlo simulation. In these simulated DW images, we can inject motion information according to the proposed motion model. By estimating the signal loss in each sector, we can add the motion into these images. Then we add the Rician noise into these images. Finally, we calculate the diffusion parameters, such as FA, MD, and fiber angles. By comparing to the ground truth, we can quantify the effects of cardiac motion. Meanwhile the

images with motion and noise are processed by PCATMIP. Diffusion parameters are calculated again and the results are compared to the ground truth, which allows us to investigate the efficiency of the motion correction method. This chapter provides a theoretical basis on in vivo cardiac DTI for the following chapter.

To demonstrate that our multiple shifted TD acquisitions combined with PCATMIP post-processing can tackle motion effects, we apply this scheme to in vivo cardiac DTI data acquired under free-breathing in chapter 4. As described in chapter 3, our method to cope with the bulk motion consists in using shifted acquisitions with retrospective motion correction registration. The heart is much more stable at end diastole as known from a previous study (Rapacchi et al. 2011). Therefore, we acquire 10 TD DW images at end-diastole using a bipolar sequence. Then the multiple TD images are registered by a non-rigid image registration method. In the end, diffusion information is retrieved by PCATMIP post-processing: PCA (as a filter to remove noise) and in line TMIP (to pick the largest signal intensity from the 10 TD images, pixel by pixel, as an image fusion method). Totally, we acquired 10 slices covering the whole heart in 12 directions, and the scan time under free breathing is less than 25 min.

Based on our special multiple shifted DW images, we propose another image fusion method based on wavelet reconstruction in chapter 5. Wavelet fusion techniques are commonly used to combine multiple images into a single one, while retaining important local features from each image and providing a more accurate description of the object. In our case, ideally, we would like to collect all the meaningful diffusion information from the input images (multiple TDs), while discarding the parts strongly affected by the bulk motion. In chapter 5, we propose a fusion rule for fusing the wavelet coefficients and then obtain the fused image by performing the inverse wavelet transform. Then we use a PCA denoising method. At last, we also calculate the diffusion parameters and 3D fiber architectures. With this processing scheme, much smoother fiber tractographies are obtained. In this chapter, we also compare the in vivo cardiac DTI results between PCATMIP and WIF methods.

In chapter 6, we give the conclusions and the perspectives.

Introduction (en français)

Les maladies cardiaques sont la principale cause de décès dans le monde. Les maladies cardiovasculaires (English, CVD) sont causées par des troubles du coeur et des vaisseaux sanguins, et comprennent les maladies coronariennes (crise cardiaque), la maladie cérébrovasculaire, la pression artérielle élevée (hypertension), la maladie artérielle périphérique, les cardiopathies rhumatismales, les maladies cardiaques congénitales et l'insuffisance cardiaque. On estime que 17 millions de personnes meurent de maladies cardiovasculaires chaque année, notamment les crises cardiaques et les accidents vasculaires cérébraux. Un nombre important de ces décès peuvent être attribués au tabagisme, qui augmente le risque de mourir de maladies coronariennes et de maladies cérébrovasculaires 2 à 3 fois plus élevé. Chaque année CVD provoque plus de 4 millions de décès en Europe et plus de 1.9 million de décès dans l'Union européenne (rapport Oxford). En raison de leur taux élevé de mortalité, les maladies cardiaques sont devenues la maladie la plus coûteuse. Selon l'American Heart Association (AHA), les maladies cardiovasculaires étaient amenées à coûter 444.2 milliards de dollars en 2010, y compris les services de soins de santé, les médicaments et la perte de productivité. Par conséquent, du point de vue des possibilités de santé et d'économie, il est essentiel et important de développer des techniques qui permettent une meilleure compréhension des structures et des fonctions du cœur avant sa défaillance.

La fonction myocardique est fondamentalement liée à son architecture de fibres spécifique. L'analyse de la structure des fibres du myocarde est considérée comme un facteur important dans la compréhension de la maladie sous-jacente et les arythmies associées. Cela est dû au fait que la structure de fibres myocardiques est modifiée au fil du temps par diverses cardiomyopathies. Dans un coeur en bonne santé, il est généralement admis que des fibres musculaires cardiaques ou myofibres sont disposées en spirales autour des ventricules et l'orientation des fibres dépend de leur emplacement transmural. Récemment, l'étude sur l'atlas de l'architecture des fibres cardiaques chez l'homme sur une population saine a montré que l'angle d'hélice de l'orientation moyenne des fibres est fortement corrélé à la profondeur transmurale et varie de -41° sur l'épicarde à +66° sur l'endocarde (Lombaert et al. 2012). En outre, les fibres musculaires sont principalement organisées dans la direction ascendante à la surface endocardique et épicardique et tourner dans une direction circonférentielle dans le milieu de la paroi médiane. Cette structure hélicoïdale est responsable du mouvement de torsion du ventricule gauche et les principales fonctions mécaniques. Par conséquent, la structure 3D des fibres myocardiques peut fournir des indices importants pour comprendre les propriétés physiologiques et fonctionnelles du cœur et pour le diagnostic des maladies du cœur. La première compréhension de l'architecture de fibres cardiaques est dérivée de l'étude histologique sur les zones intéressantes du tissu (Streeter et al. 1969). La technique histologique est connue pour souffrir de distorsion et de désalignement, et elle ne permet pas la reconstruction 3D des structures fibreuses. Pour résoudre ces problèmes, l'imagerie à lumière polarisée (PLI) a été proposée pour étudier les orientations des fibres dans les cœurs fœtaux ex vivo (Jouk et al. 2007). Elle peut fournir l'orientation 3D des fibres myocardiques avec une résolution spatiale élevée de $0.1 \times 0.1 \times 0.5$ mm^3. Par rapport aux méthodes de

dissection et histologique, PLI est plus objective car elle ne comporte aucune opération humaine durant le processus de mesure. Cependant, la technique histologique et PLI sont ex vivo et ne peuvent être utilisées pour étudier l'architecture de fibres du cœur humain in vivo.

Plus récemment, l'imagerie par résonance magnétique du tenseur de diffusion (DTI) (Basser & Pierpaoli 1996) apparaît comme la seule façon non destructive et non invasive pour observer l'architecture de fibres cardiaques in vivo et fournit des informations directement en 3D. L'étude des atlas de fibres du cœur ex vivo en utilisant la technique DTI a été rapportée (Lombaert et al. 2012). Cependant, l'imagerie DTI in vivo est beaucoup plus diffcile en raison du mouvement lors des acquisitions. Le mouvement global du coeur est un mélange complexe de mouvement cardiaque associé à son cycle de pompage et le mouvement respiratoire qui entraîne une torsion supplémentaire et la distorsion volumétrique. Le mouvement respiratoire est relativement imprévisible et peut varier considérablement d'une personne à l'autre et d'un instant à l'autre. Un objet en mouvement va changer à la fois la phase et l'amplitude de ses composantes dans l'espace k. Le mouvement lors de l'acquisition de l'image va donc introduire des artefacts, et ceux-ci peuvent être divisés en deux catégories, le mouvement lors de l'acquisition d'une phase-encoder ligne intra-vue, et le mouvement entre les différentes lignes de codage de phase inter-view. Pour la plupart des séquences intra-view, le mouvement à des vitesses myocardiques et respiratoires typiques peut être ignoré. Les artéfacts de mouvement inter-view peuvent être causés par le mouvement cardiaque et la respiration sont très dépendants de la nature du mouvement par rapport à la couverture de l'espace k. La première tentative d'acquerir des données de diffusion sur le coeur humain in vivo a été réalisée en utilisant une séquence STEAM (stimulated echo acquisition mode) (Edelman et al. 1994). L'imagerie de diffusion cardiaque en utilisant une préparation de STEAM présente l'avantage d'avoir le temps de balayage plus court par intervalle RR, réduisant ainsi le mouvement intrascan, mais double le temps de balayage total par rapport à des séquences d'écho de spin (Gamper et al. 2007) car l'encodage et le décodage doivent se faire en deux cycles cardiaques consécutifs. L'étude dans (Reese et al. 1996) a montré la faisabilité de cartographier les orientations des fibres quantitativement sur des sujets humains; ils ont constaté que l'imagerie cardiaque par pondération de diffusion est sensible à la déformation du myocarde due au mouvement. Dans (Tseng et al. 2000), les auteurs ont proposé une méthode d'obtenir des données de diffusion précises en exigeant la mesure d'une séquence supplémentaire et en définissant un "sweet spot" dans le cycle cardiaque où l'effet de déformation net sur la diffusion observée se rapproche de zéro. Dou et al ont développé une technique en mode d'acquisition par écho stimulé pour l'imagerie cardiaque in vivo par pndération de diffusion, qui présente l'inconvénient majeur d'avoir intrinsèquement un faible rapport signal sur bruit (SNR). Dans (Gamper et al. 2007), une approche d'écho de spin avec un gradient d'encodage bipolaire de diffusion a été proposée afin de rendre la séquence insensibleau mouvement systolique du cœur. Plusieurs implémentations (Edelman et al. 1994; Reese et al. 1996; Gamper et al. 2007) ont été utilisées pour compenser la perte du signal induite par le mouvement, y compris les navigateurs rétrospectifs et l'apnée, qui nécessitaient des temps d'acquisition d'environ 7 minutes par coupe. Dans la majorité de ces études, cependant, que ce soit un seul (Tseng et al. 2000; Gamper et al. 2007; Dou et al. 2009) ou trois (Nielles-Vallespin et al. 2012) coupes pourraient être acquises. Une reconstruction 3D de

l'architecture des fibres cardiaques à établir pour l'atlas humain in vivo en utilisant des schémas de transformation conforme (Toussaint et al. 2010) a été proposée. Néanmoins, que ce soit trois (Nielles-Vallespin et al. 2012) ou cinq (Toussaint et al. 2013) coupes ne sont pas suffisantes pour construire l'architecture 3D entière de fibres en raison de la faible résolution spatiale (épaisseur de coupe de 6 ou 8 mm). La construction de l'architecture 3D de fibres cardiaques utilisant streamline bénéficierait d'un plus grand nombre de coupes.

Le but de cette étude est d'étudier la faisabilité de l'magerie DTI cardiaque in vivo et de la tractographie des fibres 3D du cœur entier dans des conditions de respiration libre et sans recourir au gating respiratoire. Notre méthode pour s'attaquer aux problèmes de mouvement est une stratégie d'acquisition spéciale combinée avec des méthodes de post-traitement. À cette fin, des données DTI cardiaques in vivo avec des mouvements réduits ont d'abord été acquises à la fin de la diastole à l'aide des retards de déclenchement multiples décalés (TD). Ensuite, une méthode de recalage non-rigide (Guetter et al. 2011) a été utilisée pour corriger le mouvement interscan causé par la respiration. Ensuite, deux méthodes de post-traitement ont été étudiées pour des séquences temporelles d'images correspondant aux différents instants d'acquisition afin de compenser la perte de signal. La première est la méthode de PCATMIP (Pai et al. 201; Delattre et al. 2012) qui repose sur l'analyse en composantes principales (PCA) et sur la projection d'intensité maximale dans le temps (TMIP). Afin d'évaluer cette technique pour des applications cliniques, de quantifier les effets de mouvement sur les paramètres de diffusion, et d'évaluer la précision de notre méthode de correction de mouvement, nous avons d'abord réalisé des simulations basées sur des données réelles de fibres cardiaques provenant de PLI et des données de mouvement in vivo acquises par la technique de DENSE. A partir des résultats ainsi obtenus, nous avons développé la deuxième méthode pour l'imagerie DTI in vivo, qui est basée sur la fusion d'images via ondelettes (WIF), combinée avec une méthode de débruitage PCA. Les images DW finalement ainsi obtenues sont ensuite utilisées pour calculer le champ de tenseurs, à partir duquel les paramètres de diffusion tels que l'anisotropie fractionnelle (FA), la diffusivité moyenne (MD), l'angle d'hélice (HA), et l'architecture de fibres in vivo (faisceaux de fibres 3D) sont calculés et comparés.

La présentation de cette thèse est organisée comme suit.

La première partie de cette thèse est consacrée à la présentation des bases médicales de l'imagerie cardiaque et la méthodologie de notre travail:

Le chapitre 1 décrit les notions d'anatomie et de la physiologie du cœur et de l'organisation architecturale du cœur humain.

Le chapitre 2 décrit en détail l'imagerie cardiaque, y compris le système d'imagerie PLI, le principe de l'imagerie par résonance magnétique et l'imagerie du tenseur de diffusion (DTI). Ensuite sont discutés les défis actuels de l'imagerie DTI cardiaque in vivo en acquisitions avec respiration libre et en temps de balayage long.

La deuxième partie est consacrée à l'étude de la simulation et de l'imagerie DTI cardiaque in vivo. Le travail présenté dans le chapitre 3 porte sur l'étude des effets de mouvement sur les paramètres de diffusion, sur la quantification de ces effets, et sur l'évaluation de la performance de notre méthode de correction du mouvement. Pour la simulation, tout d'abord, nous avons besoin de construire un modèle sur la perte de signal causée par le mouvement. À

cette fin, nous acquérons des images de diffusion sur plusieurs phases cardiaques et des images DENSE sur 6 volontaires. En total, nous avons acquis 20 phases par cycle cardiaque entier. En utilisant les deux types d'informations, nous pouvons estimer la perte de signal en fonction du déplacement longitudinal. Ensuite, nous calculons la moyenne des 6 courbes, en raison de la grande différence en résolution entre les données PLI et DWI. La moyenne est basée sur le calcul dans des secteurs du LV segmentés selon AHA. Dans la simulation, la vérité-terrain est le cœur ex vivo cœur acquis par PLI. Connaissant l'orientation des fibres, nous pouvons dériver des images DW multidirectionnelles simulées par Monte-Carlo. Dans ces images DW simulées, nous pouvons injecter des informations de mouvement selon le modèle de mouvement (la courbe moyenne de mouvement). En calculant la perte de signal dans chaque secteur, nous pouvons ajouter le mouvement correspondant dans ces images. Ensuite, nous ajoutons du bruit dans ces images. Enfin, on calcule les paramètres de diffusion, tels que FA, MD et les angles de fibres. En comparant ces paramètres avec la vérité-terrain, nous pouvons quantifier les effets de mouvement cardiaque. En même temps, les images corrompues par le mouvement et le bruit sont traitées par PCATMIP. Des paramètres de diffusion sont calculés de nouveau et les résultats sont comparés avec la vérité-terrain, ce qui nous permet d'étudier l'efficacité de la méthode de correction de mouvement. Les résultats révèlent que PCATMIP améliore la précision de mesure de FA and MD, et peut également préserver la sensibilité de la diffusion et l'architecture de fibres. Ce chapitre fournit une base théorique sur DTI cardiaque in vivo pour le chapitre suivant.

Pour montrer que notre acquisition de TD multiples et décalés combinée avec le post-traitement PCATMIP peut s'attaquer aux effets de mouvement, dans le chapitre 4, nous appliquons ce schéma de combinaison à l'imagerie DTI cardiaque in vivo acquises avec respiration libre. Comme décrit dans le chapitre 3, notre méthode pour faire face au mouvement est d'utiliser des acquisitions décalées avec des corrections de mouvement rétrospectives par recalage. Le cœur est beaucoup plus stable à la fin de diastole comme démontré dans une étude précédente (Rapacchi et al. 2011). Pour cette raison, nous acquérons 10 images DW avec TD différents à la fin de la diastole en utilisant une séquence bipolaire. Ensuite, ces images multiples sont recalées par une méthode non-rigide. Enfin, les informations de diffusion sont récupérées par le post-traitement PCATMIP: PCA (comme un filtre pour éliminer les parasites) et TMIP (prendre la plus grande intensité du signal à partir des 10 images TD, pixel par pixel, comme une méthode de fusion d'images). En total, nous avons acquis 10 coupes couvrant l'ensemble du coeur dans 12 directions, et le temps d'acquisition avec respiration libre est moins de 25 min. Les calculs des paramètres de diffusion avec PCATMIP et avec un TD (une seule acquisition) montrent que la surestimation de FA et MD peut être réduite par PCATMIP, ce qui est cohérent avec les résultats de simulation présentés dans le chapitre 3. Les résultats montrent que l'architecture 3D de fibres obtenue est en bon accord avec les études rapportées dans la littérature pour des DTI cardiaques humaines aussi bien in vivo et qu'ex vivo.

En nous appuyant sur nos images DW multiples correspondant à des TD décalés, nous avons proposé une autre méthode de post-traitement, basée sur la fusion d'images au moyen de la transformée en ondelettes (WIF), comme décrit au chapitre 4. Les techniques de fusion via ondelettes sont généralement utilisées pour combiner plusieurs images en une seule, tout

en conservant les caractéristiques locales importantes de chacun des images et fournir une description plus précise de l'objet. Dans notre cas, idéalement, nous aimerions préserver toutes les informations utiles dans les images de diffusion d'entrée (multiple TDs), tout en rejetant les parties fortement affectées par le mouvement. Dans le chapitre 5, nous proposons une règle de fusion pour fusionner les coefficients d'ondelettes puis obtenir l'image fusionnée en effectuant la transformée en ondelettes inverse. Ensuite, nous utilisons une méthode de débruitage basée sur PCA. Enfin, nous calculons les paramètres de diffusion et de l'architecture de fibres 3D. Avec ce schéma de traitement, des tractographies de fibres beaucoup plus lisses et cohérentes sont obtenues. Dans le chapitre 5, nous comparons les résultats de DTI cardiaque in vivo entre les méthodes PCATMIP et WIF. En comparant les champs de tenseurs et les faisceaux de fibres 3D, le schéma de traitement WIF fournit de meilleurs résultats que PCATMIP.

Dans le chapitre 6, nous donnons les conclusions générales et les perspectives.

Part I

Introduction and background

Chapter 1

Human heart function and structure

Contents

Abstract

To understand the context of this thesis, in the first chapter we introduce the structures of the heart and some characteristics of fiber structures in cardiac pathology.

The heart is divided into two cavities (left cavity and right cavity) by a wall of muscle called septum. The heart wall is composed of three layers of the tissues (outer epicardium, middle myocardium, and inner endocardium). Knowing the architecture of the myocardium, we can understand the cardiac pathologies related structures of the heart wall. We are interested by the arrangement of cardiac fibers. In this chapter, we present several models describing the structure of the myocardium as follows.

a) The band model
   Torrent-Guasp considered the myocardium structure with a hierarchy of helical ropes whose length varies with the position in the base-apex direction.
b) The geodetic model
   Streeter described the myocardium as a continum in which the orientation of myocytes varies smoothly across the ventricular wall from epicardium to the endocardium, his conjecture on the architecture of the heart: the myocardial fibers run like geodesics on a nested set of toroidal bodies of revolution.
c) Laminar structure model
   The above models belong to the class of continuum model which assumed that the material properties of the ventricular myocardium are transversely isotropic with respect to the myofiber axis, reflecting the view that neighboring myocytes are uniformly coupled. However, LeGrice and his colleagues demonstrated that the ventricular myocardium is structurally orthotropic with myocytes arranged in layers that are typically four cells thick separated by a network of extracellular collagen.

We present the structure of cardiac fibers. They are the main component of the heart muscle. Then we present the relation between cardiac fiber structure and heart function. At last, we introduce the cardiovascular disease of the heart.

Résumé en français

Afin de bien comprendre le contexte de cette thèse, dans ce chapitre, nous introduisons les structures du cœur et certaines caractéristiques des structures musculaires en cas de pathologie cardiaque. Le cœur est divisé en deux cavités (*ventricule gauche, ventricule droit*) par une paroi appelée septum. La paroi du cœur est composée de trois couches (l'endocarde, le myocarde et l'épicarde). Sachant que la plupart des pathologies cardiaques concernent les structures de la paroi, en particulier l'architecture du myocarde. Ces structures de muscles cardiaques sont présentées en détail. On s'intéresse uniquement à l'arrangement des fibres cardiaques. De nombreux modèles décrivant la structure du myocarde existent, dans ce chapitre nous en présentons trois.

a) Le modèle de bande de l'infarctus
   Torrent - Guasp considère les parois ventriculaires comme une bande orientée dans l'espace suivant une hélice formée par des boucles basale et apicale, qui se replient pour former les cavités ventriculaires.
b) Le modèle géodésique
   Streeter décrit le myocarde ventriculaire comme un continuum dans lequel l'orientation des myocytes varie doucement à travers la paroi ventriculaire de l'épicarde à l'endocarde, Sa conjecture sur l'architecture du cœur : les fibres du myocarde courent comme des géodésiques sur un ensemble imbriqué de corps torique de révolution.
c) La modèle de feuilles laminaires
   Les modèles ci-dessus appartiennent à la classe des modèles continus qui supposent que les propriétés matérielles du myocarde ventriculaire sont transversalement isotropes par rapport à l'axe des myofibrilles, traduisant l'opinion selon laquelle les myocytes voisines sont couplées de manière uniforme. Cependant, LeGrice et ses collaborateurs ont démontré que le myocarde ventriculaire est structurellement orthotrope, avec les myocytes disposées en couches distinctes connues sous le nom de feuilles laminaires, d'environ quatre cellules d'épaisseur et séparées par un réseau de collagène extracellulaire.

On présente la structure des fibres cardiaques. Elles sont le composant principal du muscle cardiaque. Et nous présentons la relation entre la fibre et la fonction cardiaque. Enfin, nous introduisons la maladie cardio-vasculaire du cœur.

The heart is an amazing organ. It continuously pumps oxygen and nutrient-rich blood throughout the body to sustain life. This fist-sized powerhouse beats (expands and contracts) 100,000 times per day, pumping five or six quarts of blood each minute. Because of its importance to the human health, the heart has been extensively studied.

1.1 Human heart anatomy

Location: The heart is located in the middle of the chest - anterior to the spine and posterior to the breastbone (long flat bone in the center of the chest). The heart lies slightly to the left, from the center of the thorax (region between head and abdomen).

Structure: The heart is divided into two cavities (left cavity and right cavity) by a wall of muscle called septum. The two cavities consist of two chambers each. Upper chambers are called atriums and the lower ones are called ventricles. The right cavity receives de-oxygenated blood from various parts of the body (except the lungs) and pumps it to the lungs, whereas the left cavity receives oxygenated blood from the lungs, which is pumped throughout the body. Let us discuss the anatomy of this amazing organ in detail.

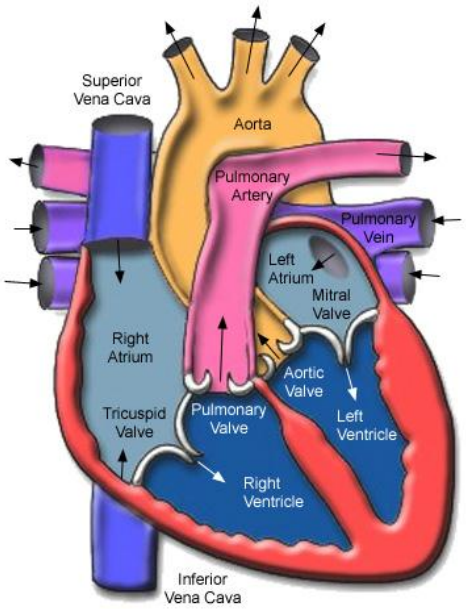

Figure 1.1. Heart anatomical structure at macroscopic scale.
http://healthinformation1.4arabs.com/heart/2.html

Outer Covering - Pericardium: The heart and the roots of its major blood vessels are surrounded and enclosed by a sac-like structure called pericardium. It comprises two parts - the outer fibrous pericardium, made of dense fibrous connective tissue and an inner double-layered membrane (parietal and visceral pericardium). The fibrous pericardium is attached to the spinal column, diaphragm and other parts of the body by ligaments. The double-layered membrane consists of an inner layer called visceral pericardium, outer layer called parietal pericardium (fused to fibrous pericardium) and a pericardial cavity (between the two layers), which contains serous fluid - pericardial fluid. This fluid helps in reducing the friction caused by the contractions of the heart.

Chambers of the Heart: As presented in Figure 1.1, the human heart has four chambers, the upper chambers known as the left and right atria, and the lower chambers called left ventricle (LV) and right ventricle (RV). Two blood vessels called the superior vena cava and the inferior vena cava, brings deoxygenated blood to the right atrium from the upper half and the lower half of the body, respectively. The right atrium pumps this blood to the RV through tricuspid valve. RV pumps this blood through pulmonary valve to the pulmonary artery, which carries it to the lungs (to get re-oxygenated). The left atrium receives oxygenated blood from the lungs through the pulmonary veins, and pumps it to the LV through the bicuspid or mitral valve. The LV pumps this blood through the aortic valve to various parts of the body via aorta, which is the largest blood vessel in the body. The heart muscles are also supplied with oxygenated blood through coronary arteries. The atria are thin-walled, as compared to the ventricles. The LV is the largest of the four chambers of the heart, and its walls have a thickness of half-inch.

Right atrium: It situates in the upper right section of the heart, receiving the de-oxygenated blood from the other parts of the body though two major veins, the superior vena cava and the inferior vena cava. The superior vena cava returns de-oxygenated blood mainly from the head, neck, arm and chest regions of the body to the right atrium. The inferior vena cava returns de-oxygenated blood from the lower body regions such as legs, back, abdomen and pelvis to the right atrium. The right atrium also pumps blood through the tricuspid valve into the RV situated below.

Right ventricle: Located below the right atrium, this chamber has a form of triangle and extends from right atrium to near the apex of the heart. It receives blood from the right atrium and pumps it to the main pulmonary artery. The main pulmonary artery extends from the RV and branches into left and right pulmonary arteries, which extend to the lungs, here oxygen-poor blood picks up oxygen and is returned to the heart via the pulmonary veins.

Left atrium: This chamber sits opposite to the right atrium. The blood goes through the lung becomes oxygenated, it returns into the left atrium via the right and left pulmonary veins and then the left atrium pumps this oxygen-rich blood into the LV through the bicuspid valve or mitral valve.

Left ventricle: It is the lower part of the heart in the left side. Compared with the RV, it is much longer and looks like a cone. It receives oxygen-rich blood from the left atrium above it, and pumps it through the aortic valve to be distributed throughout the entire body via the aorta, including to the heart muscle itself through the coronary arteries.

The left side of the heart is thicker than the right one because of the requirement to pump blood from the left side throughout the body, as opposed to the right side pumping only through the lungs.

Valves of the Heart: Basically, the valves in the heart can be classified into two types - atrioventricular or cuspid valves and semilunar valves. The former are the valves between the atria and ventricles, whereas the latter are located at the base of the ventricles. Tricuspid and bicuspid (mitral) valves are atrioventricular valves, and pulmonary and aortic valve are semilunar valves. These valves allow the blood to flow only in one direction and prevent reverse flow. The human heart pumps around five liters of blood per minute.

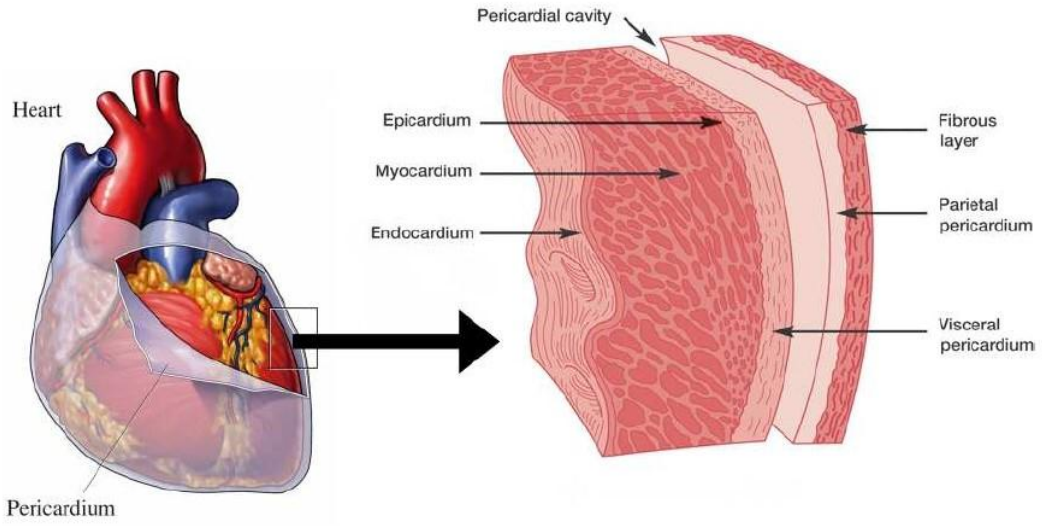

Figure 1.2. Heart wall structure.
http://www.beltina.org/health-dictionary/pericardium-function-definition.html

Heart Wall: The wall of the heart is made up of three layers of tissues - outer epicardium, middle myocardium and inner endocardium Figure 1.2. The outer epicardium functions as a protective outer layer, which includes blood capillaries, lymph capillaries and nerve fibers. It is similar to the visceral pericardium, and consists of connective tissues covered by epithelium (membranous tissue covering internal organs and other internal surfaces of the body). The inner layer called myocardium, which forms the major part of the heart wall, consists of cardiac muscle tissues. These tissues are responsible for the contractions of the heart, which facilitates the pumping of blood. Here, the muscle fibers are separated with connective tissues that are richly supplied with blood capillaries and nerve fibers. The inner layer called endocardium, is formed of epithelial and connective tissue that contains many elastic and collagenous fibers (collagen is the main protein of connective tissues). These connective tissues contain blood vessels and specialized cardiac muscle fibers called Purkinje fibers. This layer lines the chambers of the heart and covers heart valves. It is similar to the inner lining of blood vessels called endothelium.

Epicardium

Epicardium describes the outer layer of heart tissue, where is considered as a part of pericardium, it is the inner layer and called visceral pericardium. It is composed of a single sheet of squamous epithelial cells overlying delicate connective tissue. Epicardium serves as a protection layer because it can produce a pericardial fluid, which lubricates motion between the inner and outer layer of pericardium

Myocardium

The myocardium is the basic muscle that makes up the heart. This muscle is striated in nature. The cardiac muscle structure consists of basic units of cardiac muscle cells known as

myocyte. Coordinated contraction of the cardiac muscles is what makes the heart propel blood to various parts of the body. It is the function of the coronary arteries to supply blood and oxygen to the cardiac muscles. This is the thickest of all the layers. As is common knowledge, the cardiac muscle function is to ensure that the heart beats around 72 times per minute. Thus, the cardiac muscles cannot afford to rest even for a single second. Therefore, it is essential that these muscles get blood supply and nutrition continuously, as any kind of disruption in the blood and nutrition supply to these muscles can result in death of a part of the cardiac muscle, which is known as myocardial infarction or heart attack. This could in turn lead to a complete cessation of functioning of the heart muscles, known as cardiac arrest.

Endocardium

The endocardium is the innermost, thin and smooth layer of epithelial tissue that lines the inner surface of all the heart chambers and valves, which is responsible for prolonging myocardial contraction.

1.2 Cardiac function

Since the heart has a periodic motion, the description of the cardiac function can be limited to one cardiac cycle. The cardiac cycle is divided into two general categories: systole and diastole.

The heartbeat: The heartbeat is made up of systole and diastole (Figure 1.3), which are the two stages of a heartbeat. A heartbeat is a two-part pumping action that takes about a second. As blood collects in the upper chambers (the right and left atria), the heart's natural pacemaker (the SA node) sends out an electrical signal that causes the atria to contract. This contraction pushes blood through the tricuspid and mitral valves into the resting lower chambers (the right and LVs). This part of the two-part pumping phases (the longer of the two) is called diastole. The second part of the pumping phase begins when the ventricles are full of blood. The electrical signals from the SA node travel along a pathway of cells to the ventricles, causing them to contract. This is called systole. As the tricuspid and mitral valves shut tight to prevent a back flow of blood, the pulmonary and aortic valves are pushed open. While blood is pushed from the RV into the lungs to pick up oxygen, oxygen-rich blood flows from the LV to the heart and other parts of the body.

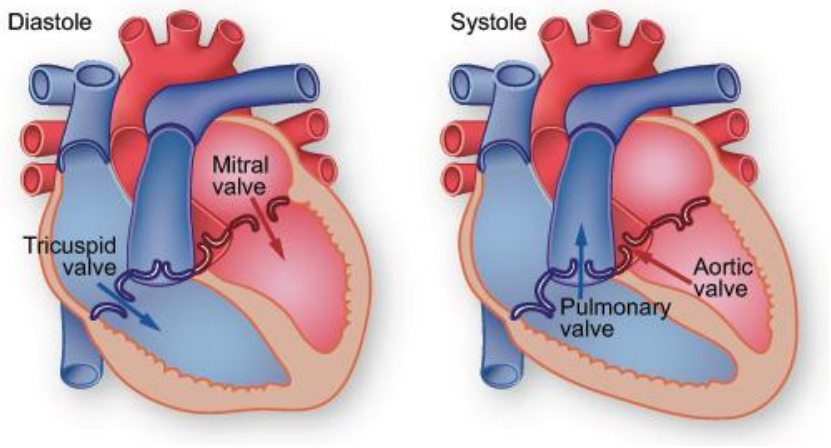

Figure 1.3. Heart diastole and systole.
http://www.texasheartinstitute.org/HIC/anatomy/systole.cfm

Usually, the cardiac cycle is described from end of diastole (ED) of the previous cycle to the end of diastole of the current cycle. The cardiac cycle is further divided into seven phases:

1. the *atrial systole*: It refers to the contraction of the atrial muscle. As the atria contract, the pressures within the atrial chambers increase, this drives blood from the atria, across the open atrio-ventricular valves, and into the ventricles. This phase starts when the P wave occurs on the ECG.
2. the *isovolumetric* contraction: This phase includes the contraction of the ventricle with all valves closed. The pressure in the ventricle increases. It is during this phase that the first heart sound is heard when the atrio-ventricular valves close. This phase starts when the R wave occurs in the ECG.
3. the *rapid ejection*: When the intraventricular pressures exceed the pressures within the aorta and pulmonary artery, the aortic and pulmonary valves open and blood is ejected out of the ventricles. While blood is ejected and ventricular volumes decrease, the atria continue to fill with blood from their respective venous inflow tracts. The opening of healthy valves is silent.
4. the *reduced ejection*: During this phase ventricular pressure falls slightly below out fow tract pressure; however, outward flow still occurs owing to kinetic energy of the blood that helps to propel the blood into the aorta and pulmonary artery. Atria pressures gradually rise during this phase owing to continued venous return into the atrial chamber. This phase is characterized by the end of the T wave on the ECG.
5. the *isovolumetric relaxation*: In this phase the ventricles relax, the intraventricular pressure decreases. When this occurs, a pressure gradient reversal causes the aortic and pulmonary valves to abruptly close, causing the second heart sound.
6. the *rapid inflow*: When the ventricular pressures fall below atrial pressures, the atrio-ventricular valves open and ventricular filling begins. The ventricles briefly continue to relax, which causes intraventricular pressures to continue to fall despite on-going ventricular filling. Filling is very rapid because the atria are maximally filled just

prior to atrio-ventricular valve opening. Once the valves open, the elevated atrial pressures coupled with the low resistance of the opened atrio-ventricular valves results in rapid, passive filling of the ventricle.

7. the *diastasis*: This reduced filling phase is the period during diastole when passive ventricular filling is nearing completion. Increased intraventricular pressure reduces the pressure gradient across the atrio-ventricular valves so that the rate of filling declines, even though atrial pressures continue to increase slightly as venous blood continues to flow into the atria. Aortic pressure and pulmonary arterial pressure continue to fall during this period as blood flows into the systemic and pulmonary circulations.

These phases can be detected by the temporal evolution of different parameters, such as, the ECG, sound of the heartbeat, volume curves, and pressure curves. The Figure 1.4 summarizes the evolution of these parameters over a cardiac cycle. The most common and simple parameters used to assess the cardiac function are the left ventricular (LVEF) and right ventricular (RVEF) ejection fractions. They represent the fraction of blood pumped out of a ventricle with each heartbeat.

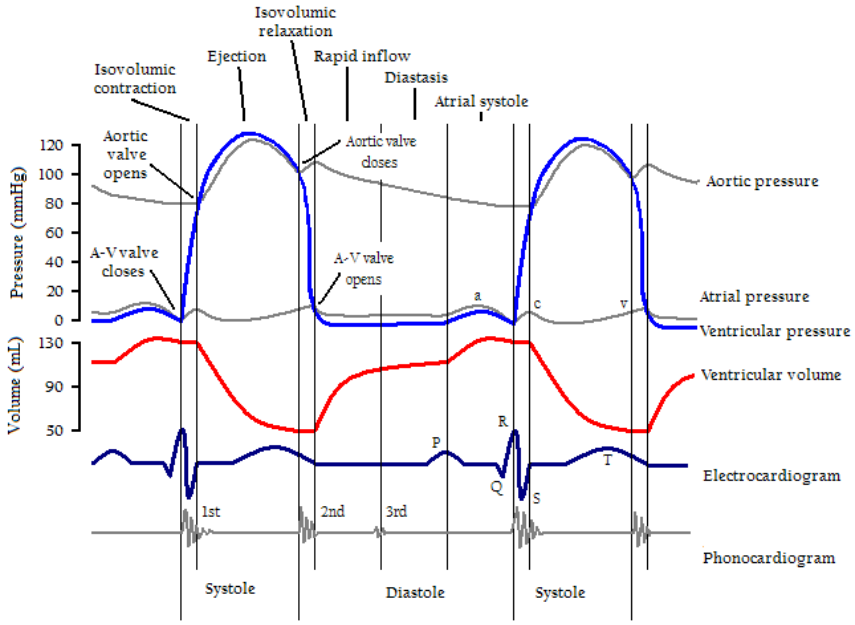

Figure 1.4. Wiggers diagram. It shows different parameters of the cardiac function during a cardiac cycle.
http://en.wikipedia.org/wiki/Cardiac_cycle

1.3 Cardiac fiber architecture

The heart, likewise any muscle, is mostly composed by muscular fibers. They are locally organized as laminar sheets (Streeter et al. 1969; Legrice et al. 1995), and have different orientations on the inner surface (endocardium) and outer surface (epicardium) of the cardiac muscle. This complex fiber architecture determines various cardiac mechanical functions

(Costa et al. 2001) and cardiac electrophysiology patterns (Hooks et al. 2002) since the torsion of the LV is directly related to the orientation of these cardiac fibers (Rüssel et al. 2009) and electrical conductivity is greatest along these fibers (Hooks et al. 2007). The exact description of this fiber architecture is not fully known in humans. Its understanding has been limited by tedious histological studies and is largely speculated from observations in other species. Different theories exist and are surveyed (Buckberg et al. 2008). The hypothesis is that the cardiac muscle may be formed by 4 myocardial bundles (Mall 1911), by a spiral muscle sandwiched onto itself (Rushmer et al. 1953), by toroidal surfaces resembling doughbuts (Streeter et al. 1969; Torrent-Guasp et al. 2005), or by a unique band folded around itself (Torrent-Guasp et al. 2005).

In the three layers of the heart wall, the myocardium layer is the most important one for maintaining the heart normal functions. There are numerous models describing the structure of myocardium, here we present several well-known ones.

1.3.1 **Myocardial band model**

The helical ventricular myocardial band (HVMB) concept, proposed in 1972 by the Spanish scientist Francisco Torrent-Guasp (Torrent-Guasp 1973), brings a new insight on the architecture of ventricular myocardium. This idea is presented based on the helical rope model, which provides an elegant way to demonstrate the configuration of myocardium. The HVMB of Torrent-Guasp is a revolutionary new concept in understanding global, 3D, functional architecture of the ventricular myocardium.

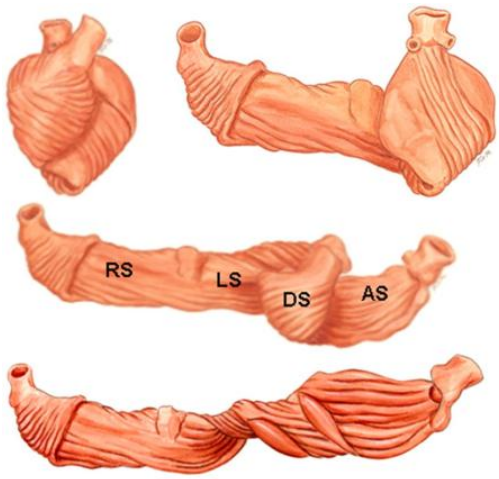

Figure 1.5. Torrent-Guasp's myocardial band model
http://jtcs.ctsnetjournals.org/cgi/figsearch?fulltext=torrent&resourcetype=3

Figure 1.5 depicts successive steps of the dissection technique applied in unraveling the ventricular mass into the HVMB. The HVMB is divided in two loops, each of them comprised of two segments. The central 180° fold of the HVMB defines two loops: the basal loop (from the root of the pulmonary artery to the beginning of the central fold; ie, to the anterior papillary muscle) and the apical loop (from the beginning of the central fold to the root of the aorta). Each of these two loops can be further divided into two segments.

The posterior interventricular sulcus, which coincides topographically with the posterior linear border of the right ventricular cavity, divides the basal loop into two segments: the right segment (RS), coinciding with the RV free wall; and the left segment (LS), coinciding with the LV. It is interesting to note here that the right and the left segments of the basal loop define the outer (non-septal) border of the tricuspid and the mitral orifices, respectfully. The apical loop can be also divided into two segments. After the 180° twist (at the central fold of the HVMB), the descendant (DS) fibers of the apical loop, make a 90° turn around the apex becoming the ascendant (AS) fibers. The posterior papillary muscle (belonging to the descendant segment) demarcates the border between the descendent and the ascendant segments of the HVMB apical loop.

HVMB provides us recognition about the myocardium muscular trajectories by the dissection means and gives some reasonable explanations about the heart electrical and mechanical properties and functions. It is very important for evaluating the other means for investigating the myocardium muscle orientations.

1.3.2 **Geodesic model**

Geodesic cardiac fiber model is firstly proposed by Streeter (Streeter 1979), he stated that the myocardial fibers run like geodesics on a nested set of toroidal bodies of revolution. This mathematical expression is a little obscure for anatomist and cardiologist. Therefore a few years ago, Jouk (Jouk et al. 2007) made a clear explanation about this model using the Figure 1.6.

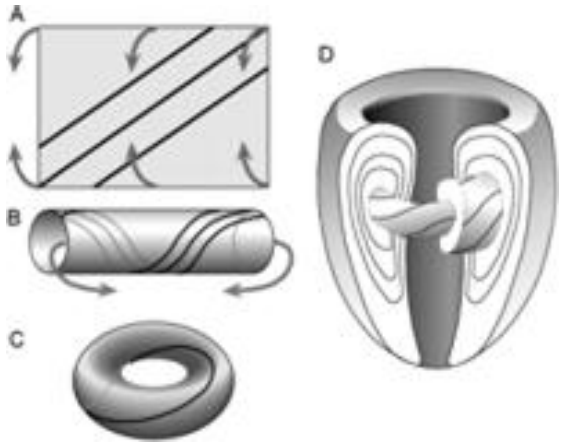

Figure 1.6. Geodesic model

Firstly, take a piece of paper and draw three parallel lines, these lines could be considered as the geodesics of the plane surface. Secondly, roll the paper making the superior border against the inferior border and forms a cylinder, the drawn lines in the first step becomes the geodesics of the cylinder. Thirdly, bend the cylinder until the left reaches the right, a torus will be generated and the lines are still geodesics. Finally, Streeter's conjecture supposed that from inner to outer the myocardial muscle nested by the elongated tori like Russian dolls, as shown in Figure 1.6D.

Streeter's model gives only the cardiac fiber map of LV. As an extension of Streeter's conjecture, Jouk proposed the pretzel model (Jouk et al. 2007) which describes the fiber architecture of the whole ventricular mass, illustrated in Figure 1.7.

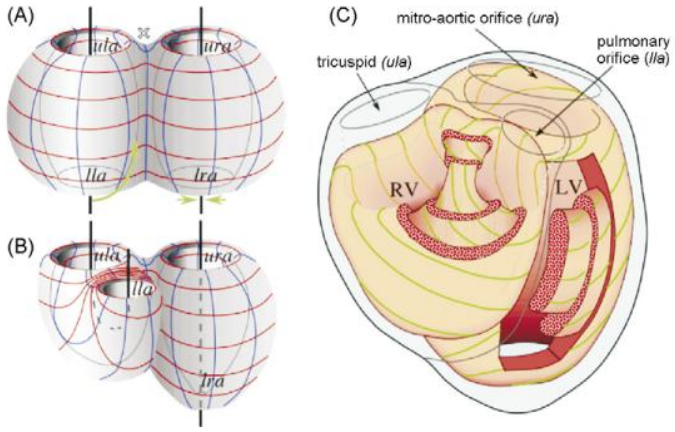

Figure 1.7. An extension of geodesic model: pretzel model. Like the pretzel cookies, two joined torus form a pretzel in this model. (A). Four special positions are defined: lower left aperture (lla), lower right aperture (lra), upper left aperture (ula) and upper right aperture (ura). For mimicking the right ventricle structure, the torus on the left was bent in such a way that the lower aperture comes up to the upper aperture. However, for the left ventricle, it is mimicked by shrinking the lower right aperture into a point, as shown in subfigure (B). In subfigure (C), it explains how LV and RV could nest together and form a pretzel model, where the green lines represent the geodesic on the nested pretzels (Jouk et al. 2007)

Compared to the Streeter's conjecture, this model gives not only the same description for the LV myocardial structure, but also provides a new recognition about the fiber arrangement of the RV. The upper left aperture would correspond to the tricuspid orifice and the lower left aperture to the pulmonary orifice. Between these apertures is the supraventricular crest. In this representation, it is given by the narrow part of the nested bent tori, while the wide part of the bent tori corresponds to the septal and lateral walls of the RV. Up to now, this model still requires the mathematical and experimental validations.

1.3.3 **Laminar structure model**

The both two models above belong to continuum model which assumed that the material properties of ventricular myocardium are transversely isotropic with respect to the myofiber axis, reflecting the view that neighboring myocytes are uniformly coupled. However, LeGrice and coworkers (Legrice et al. 1997) demonstrated that ventricular myocardium is structurally orthotropic, with myocytes arranged in layers that are typically four cells thick, as shown in Figure 1.8. Adjacent layers are separated by cleavage planes which have a characteristic radial orientation in base-apex ventricular section and are significant in extent, particular in the LV mid-wall. Cardiac microstructure is assumed to have three axes of symmetry: one aligned with the muscle fiber orientation (the fiber axis); a second set orthogonal to the fiber

direction and lying in the newly identified myocardial sheet plane (the sheet axis); and a third set orthogonal to the first two, in the sheet-normal direction.

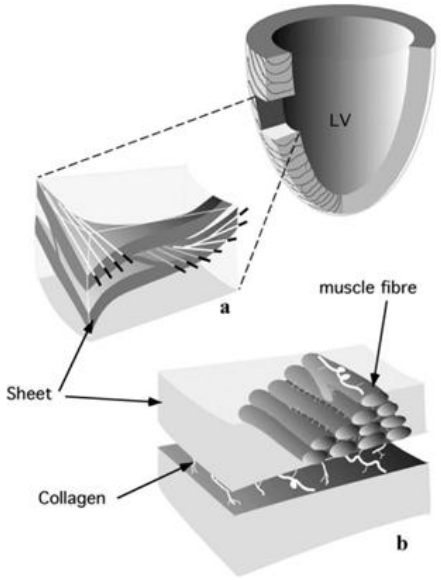

Figure 1.8. Organization of cardiac fibers as laminar sheets (Jouk et al. 2007)

1.3.4 **Relation between fiber structure and heart function**

The extension, thickening and radial reorientation of the myofiber structure allows the myocardium to contract and relax and function as a pump but the exact mechanism is still unclear. Several techniques have been used to compensate for cardiac motion and cardiac DTI data have been successfully acquired both at systole and diastole. Recent results obtained by Nielles and co-workors have shown that there is a reorganization of cardiac fibers i.e. variation in orientation of the diffusion tensor over the cardiac cycle (Figure 1.9). The ability to map myocardial fiber structure and its dynamics, especially combined with myocardial strain imaging techniques, could provide novel insights into the structure-function relation in the heart.

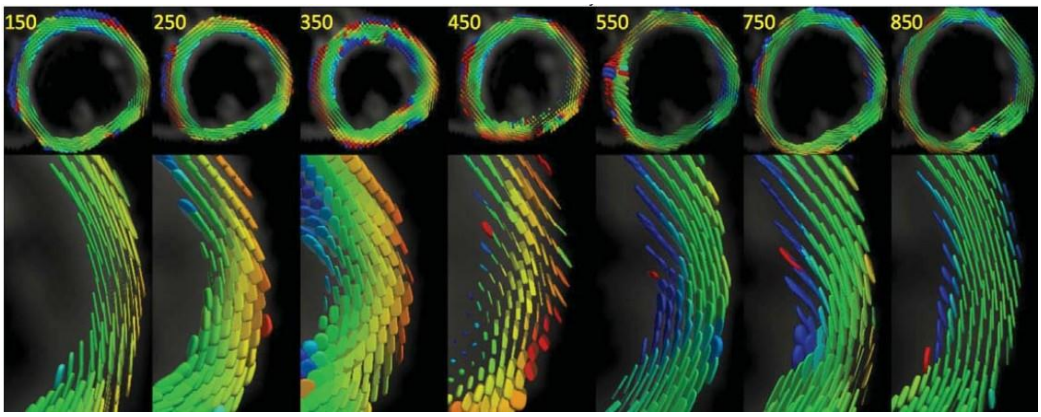

Figure 1.9. Cardiac diffusion tensors at different time points of the cardiac cycle. (Nielles-vallespin et al. 2013)

1.4 Cardiovascular disease

Cardiovascular diseases are a large group of pathologies of the heart and blood vessels including hypertension, coronary heart disease, cerebrovascular disease, peripheral vascular disease, rheumatic heart disease, congenital heart disease, heart failure, and cardiomyopathies. The most frequent cardiovascular causes of death are heart attacks due to coronary heart diseases and strokes due to cerebrovascular diseases. Each year heart diseases cause almost 25% deaths (Roger et al. 2011), thus it is very critical to learn about the heart structure, function impairements as well as tissue changes in pathologies in order to understand the heart disease. Cardiac MRI plays here a unique role, since it is the preferred modality to investigate and follow-up cardiac function, structure and characterizes myocardial tissue non-invasively in myocardial pathologies. It therefore represents an important field of research and investment.

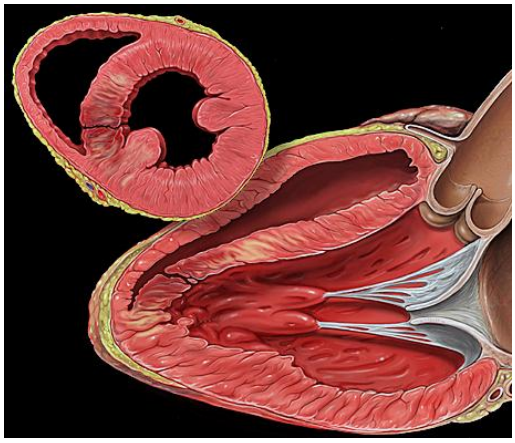

Figure 1.10. An example of infarct human heart.
http://commons.wikimedia.org/wiki/File:Heart_post_infarct_vsd_views.jpg

Cardiovascular diseases are the largest cause of death over the world. From 1998 to 2008, the rate of death attributable to cardiovascular disease (CVD) declined 30.6%. Mortality data shows that CVD accounted for 32.8% (811 940) of all 2 471 984 deaths in 2008 in the United States. It remains the major cause of premature death in Europe, even though CVD mortality has fallen considerably over recent decades in many European countries. If current trends continue, World Health Organization (WHO) estimates that more than 20 million people will die from CVD by 2020, representing 31.5% of all deaths. CVDs are not only a cause of mortality, but also a cause of morbidity (diseased state, disability, or poor health) that is more diffcult to measure. The main measure of the burden of diseases is the Disability Adjusted Life Year (DALY) combining years of life lost due to premature death and years of healthy life lost due to disability. In Europe, 23% of all DALYs are due to CVDs and only 10% over the world. It is estimated that 80% of all CVD mortality now occurs in developing countries. Let us introduce some types of the cardiac disease.

Dilated cardiomyopathy

Dilated cardiomyopathy (DCM) (Figure 1.11) is the most common form of cardiomyopathy accounting for one third of cases. DCM is often the result of damage to the myocardium produced by a variety of insults (e.g. ischemia, virus, toxins such as alcohol and chemotherapeutic agents). In a significant portion of cases of DCM, a definitive etiology can not be established by standard testing and among these patients; a substantial percentage may have an underlying genetic cause. In general, approximately 20-50% of DCM patients have familial forms of the disease, with mutations of genes encoding cytoskeleton, contractile, or other proteins present in myocardial cells. The incidence of DCM has been estimated to be five to eight cases per 100,000 with a prevalence of 1/2,700 individuals. However, these figures may underestimate the frequency of the disorder because so many patients with DCM are asymptomatic.

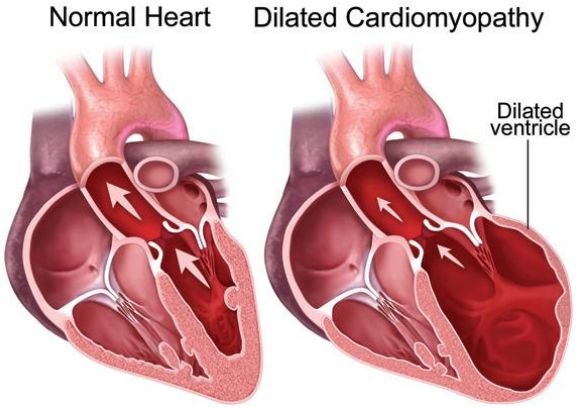

Figure 1.11. Dilated cardiomyopathy
http://www.genedx.com/test-catalog/cardiology/dilated-cardiomyopathy/

Hypertrophic cardiomyopathy

Hypertrophic cardiomyopathy (HCM) (Figure 1.12) is a form of cardiomyopathy. The heart muscle thickens due to genetic problems with the muscle's structure. As the muscle thickens, it must work harder to pump blood. This strains the heart muscle. Sometimes the thickened muscle gets in the way of the blood leaving the heart and causes a blockage. This blockage can cause a nearby valve to become leaky. HCM can cause uneven muscle growth. This can cause the heart to pump in a disorganized way. Rarely, it can cause abnormal heart rhythms that can be fatal.

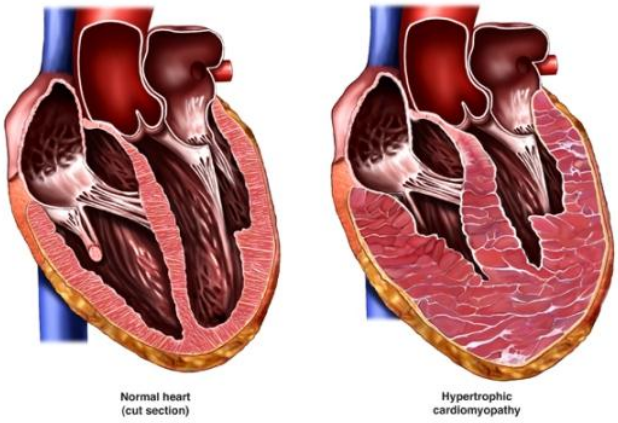

Figure 1.12. Hypertrophic cardiomyopathy
http://www.beliefnet.com/healthandhealing/getcontent.aspx?cid=615222

CVDs are strongly connected to lifestyle, especially the use of tobacco, unhealthy diet habits, physical inactivity, and psychosocial stress. CVD prevention remains a major challenge for the general population, politicians, and healthcare workers. The bases of prevention are rooted in cardiovascular epidemiology and evidence-based medicine. The high incidence of CVDs is a major financial burden. Overall CVD is estimated to cost the EU economy almost €196 billion per year. Therefore, the heart structure should be studied in order to improve health care and raise public awareness.

1.5 Conclusion

In this chapter, the heart structures have been presented, especially, the architecture of heart wall and the cardiac fiber arrangement patterns have been described in detail. It has been illustrated that most of cardiomyopathies affect the structure of ventricles, thus investigating the cardiac fiber architecture in the ventricles before and after heart disease becomes so significant for the clinical diagnosis and treatment.

Chapter 2

Cardiac imaging

Contents

Abstract

As described in the first chapter, analyzing the architecture of cardiac fibers is one of the most important ways to study cardiomyopathy. Our first understanding of cardiac fiber architectures is from the histology of cardiac tissue in a selected region. This technique is known to suffer from distortion and misalignment and does not allow the 3D reconstruction of fibrous structures. To solve this problem, polarized light imaging (PLI) was proposed. It measures the orientation of ex vivo heart fibers. This technique provides a map of 3D myocardial fiber orientations with a high spatial resolution (0.1 mm × 0.1 mm × 0.5 mm). However, both histological and PLI techniques cannot be used for in vivo studies of the human heart.

More recently, diffusion magnetic resonance imaging (dMRI), which includes the diffusion tensor imaging (DTI) and high angular resolution diffusion imaging (HARDI), has been proposed as a new technique to analyze the structure of fibers in vivo. We present a detailed imaging (PLI and DTI) methods in this chapter, highlighting their advantages and disadvantages for ex vivo and in vivo measurements.

a) Polarized Light Imaging (PLI)

PLI produces images whose contrast is based on light scattering by the structure of tissues. Generally, the PLI system is composed of the following elements: a white light source, a first linear polarizing filter served as the polarizer, a stage to hold the birefringent specimen, another linear polarizing filter acting as the analyzer whose vibration axis is perpendicular to that of the polarizer and finally a CCD camera that measures the amount of transmitted light. When a birefringent sample is positioned in the path of polarized light, it interferes with the axis of polarization of the light. Thus the amount of light transmitted is a function of the birefringence of the sample and its orientation with respect to the light.

b) Magnetic Resonance Imaging (MRI)

In this chapter, we introduce the general principle of MRI and the phenomenon of diffusion and finally the theory of DTI. Measurements of tissue properties are due to the difference of relaxation times and spin density of protons following a radio frequency magnetic excitation. To understand the physical basis of MRI, we introduce briefly the concepts of precession, resonance and relaxation. Obtaining an image signal from the magnetic relaxation requires a spatial coding based on the successive application of diffusion gradients in different spatial direction (slice selection gradient, phase encoding gradient, and frequency encoding gradient). The water molecules in the tissue carry a lot of information about the anatomical underlying architecture by applying diffusion encoding gradients. Diffusion-weighted imaging (DWI) is used to describe how water diffuses in the tissues, and subsequently obtain structure information.

At last, we present the current challenges in in vivo cardiac DTI.

Résumé en français

Comme nous l'avons précisé dans le premier chapitre, analyser l'architecture des fibres cardiaques est l'un des plus importants moyens pour étudier la cardiomyopathie. Notre première compréhension de l'architecture des fibres cardiaques proviennent de l'histologie des tissus cardiaques dans une région sélectionnée. Cette technique est connue pour souffrir de distorsion et de désalignement, et ne permet pas la reconstruction des structures fibreuses en 3D. Pour résoudre ce problème, l'imagerie par lumière polarisée (PLI) a été proposée. Elle permet de mesurer l'orientation des fibres du cœur ex vivo. Cette technique fournit une carte d'orientations des fibres myocardiques avec une haute résolution spatiale en 3D (0.1 mm × 0.1 mm × 0.5 mm). Cependant, les deux techniques histologiques et PLI sont ex vivo et ne peuvent pas être utilisées pour des études in vivo du cœur humain.

Plus récemment, l'imagerie par résonance magnétique de diffusion (IRMd), qui comprend l'imagerie du tenseur de diffusion (DTI) et l'imagerie de diffusion à haute résolution angulaire (HARDI), a été proposée comme une technique nouvelle et prometteuse pour analyser la structure des fibres in vivo. Nous présentons en détail les méthodes d'imagerie PLI et IRMd dans ce chapitre, en soulignant leurs avantages et inconvénients pour les mesures ex vivo et in vivo.

a) L'imagerie en lumière polarisée (PLI).

PLI produit des images dont le contraste est basé sur la diffusion de la lumière par l'ultrastructure des tissus. En général, le système de PLI se compose des éléments suivants: une source de lumière blanche, un premier filtre polarisant linéaire utilisé comme polariseur, un support pour maintenir le spécimen de tissu biréfringent à analyser, un autre filtre de polarisation linéaire qui agit comme analyseur et dont l'axe de polarisation est perpendiculaire à celui du polariseur et enfin une caméra CCD qui mesure la quantité de lumière transmise. Quand un échantillon biréfringent est positionné dans le trajet de la lumière polarisée, il interfère avec l'axe de polarisation de la lumière. Ainsi la quantité de lumière transmise est une fonction de la biréfringence de l'échantillon et de son orientation par rapport à la lumière.

b) L'imagerie par résonance magnétique (IRM)

Dans ce chapitre nous introduisons d'abord le principe général de l'IRM, puis le phénomène de diffusion, et enfin la théorie de l'IRMd. L'IRM mesure les propriétés magnétiques des tissus (principalement de l'eau et de la graisse) grâce à la différence des temps de relaxation et de densité de spins des protons suite à une excitation magnétique radio fréquence. Afin de bien comprendre les fondements physiques de l'IRM, nous introduisions brièvement les concepts de précession, de résonance et de relaxation. L'obtention d'une image à partir du signal magnétique de relaxation nécessite un codage spatial qui repose sur l'application successive de gradients de champ magnétique dans chaque direction spatiale, à savoir un gradient de sélection de coupe, le codage de phase, et le codage par la fréquence. Le trajet parcouru par les molécules d'eau dans les tissus porte beaucoup d'informations sur l'architecture anatomique sous-jacente. L'imagerie par résonance magnétique pondérée en diffusion (DWI) est utilisée pour détecter la façon dont l'eau diffuse dans les tissus afin d'obtenir de précieuses informations sur les structures sous-jacentes.

Enfin, nous présentons les défis actuels de l'imagerie in vivo du tenseur de diffusion cardiaque.

2.1 Polarized Light Imaging (PLI)

PLI is a contrast-enhancing technique, well adapted to imaging birefringent materials. This technique is used in a broad range of disciplines, including medicine, biology, geology, materials science, and food industry etc. Recently, many works focus on fiber tracking. For instance, the white matter architecture was imaged by means of PLI (Larsen et al. 2007; Palm et al. 2010). The 3D fiber structure of the brain with high spatial resolution using PLI was mapped (Axer et al. 2011; Dammers et al. 2012). Reconstruction and signal enhancement methods for PLI used in fiber tracking were proposed (Dammers et al. 2010; Wang et al. 2012). An attempt to using PLI to investigate the cardiac fiber architecture was also raised (Jouk et al. 1995; Jouk et al. 2007). This section briefly introduces the PLI principle, its advantages, limitations, and the way used to measure cardiac fiber orientations.

2.1.1 Introduction to polarized light

Sunlight and almost every other form of natural and artificial illumination produces light waves whose electric field vectors vibrate in all planes that are perpendicular with respect to the direction of propagation. If the electric field vectors are restricted to a single plane by filtration of the beam with specialized materials, then the light is referred to as linearly polarize with respect to the direction of propagation, and all waves vibrating in a single plane are termed plane parallel or plane-polarized.

The basic concept of polarized light is illustrated in Figure 2.1 for a non-polarized beam of light incident on two linear polarizers. Electric field vectors are depicted in the incident light beam as sinusoidal waves vibrating in all directions (360°; although only six waves, spaced at 60° intervals, are included in the figure). In reality, the incident light electric field vectors are vibrating perpendicular to the direction of propagation with an equal distribution in all planes before encountering the first polarizer.

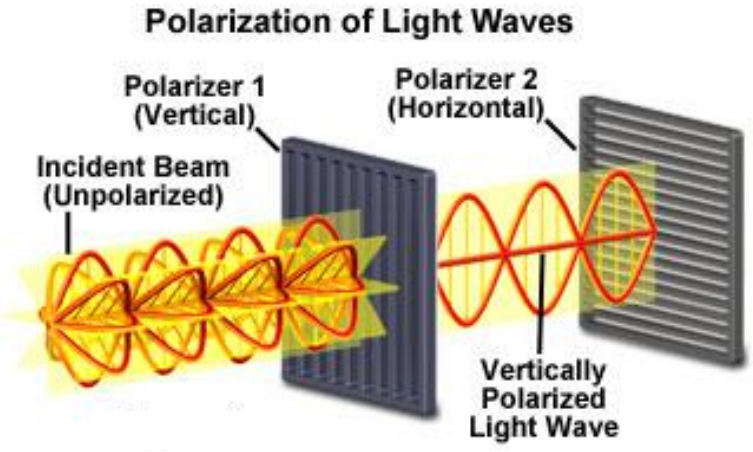

Figure 2.1. Polarization by filter

The polarizers illustrated in Figure 2.1 are actually filters containing long-chain polymer molecules that are oriented in a single direction. Only the incident light that is vibrating in the

same plane as the oriented polymer molecules is absorbed, while light vibrating at right angles to the polymer plane is passed through the first polarizing filter. The polarizing direction of the first polarizer is oriented vertically to the incident beam so it will pass only the waves having vertical electric field vectors. The wave passing through the first polarizer is subsequently blocked by the second polarizer, because this polarizer is oriented horizontally with respect to the electric field vector in the light wave. The concept of using two polarizers oriented at right angles with respect to each other is commonly termed crossed polarization and is fundamental to the concept of polarized light microscopy.

2.1.2 **Polarization by reflection**

When considering the incidence of non-polarized light on a flat insulating surface, there is a unique angle at which the reflected light waves are all polarized into a single plane. This angle is commonly referred to as Brewster's angle, and can be easily calculated utilizing the following equation for a beam of light traveling through air:

$$n = \frac{\sin\theta_i}{\sin\theta_r} = \frac{\sin\theta_i}{\sin\theta_{90-i}} = \tan\theta_i \quad (2.1)$$

where n is the refractive index of the medium from which the light is reflected, $\theta(i)$ is the angle of incidence, and $\theta(r)$ is the angle of refraction. By examining the equation, it becomes obvious that the refractive index of an unknown specimen can be determined by the Brewster angle. This feature is particularly useful in the case of opaque materials that have high absorption coefficients for transmitted light, rendering the usual Snell's Law formula inapplicable. Determining the amount of polarization through reflection techniques also eases the search for the polarizing axis on a sheet of polarizing film that is not marked

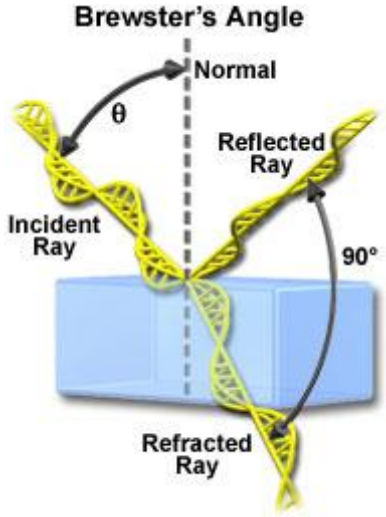

Figure 2.2. Polarization by reflection

The principle behind Brewster's angle is illustrated Figure 2.2 for a single ray of light reflecting from the flat surface of a transparent medium having a higher refractive index than air. The incident ray is drawn with only two electric vector vibration planes, but is intended to

represent light having vibrations in all planes perpendicular to the direction of propagation. When the beam arrives on the surface at a critical angle (Brewster's angle; represented by the variable θ in Figure 2.2), the polarization degree of the reflected beam is 100 percent, with the orientation of the electric vectors lying perpendicular to the plane of incidence and parallel to the reflecting surface. The incidence plane is defined by the incident, refracted, and reflected waves. The refracted ray is oriented at a 90° angle from the reflected ray and is only partially polarized.

2.1.3 **Cardiac fiber measurements using PLI**

The principle of PLI is to use the polarization property of light to detect the birefringence of a material under study and consequently to infer its spatial structure. The fibre orientation maps were generated by means of polarized light microscopy (Jouk et al. 1995). Generally, the PLI system is composed of the following elements: a white light source (S), a first linear polarizing filter served as the polarizer (P), a stage to hold the birefringent specimen (O), another linear polarizing filter acting as the analyzer whose vibration axis is perpendicular to that of the polarizer (A), and finally a CCD camera that measures the amount of transmitted light, as shown in Figure 2.3. The myocardial fibre is birefringent when embedded in MMA. Thus, the velocity of the light is slower (slow ray) when travelling along the long axis of the fibre than along its short axis (fast ray).

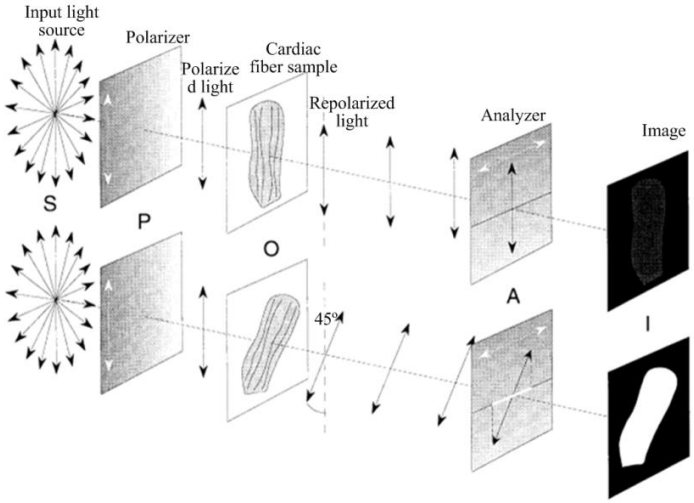

Figure 2.3. Principle of PLI system for detecting the cardiac fiber orientation. From left to right along the optical path: S is the unpolarized input light source, when it passes through the polarizer P (one polarization filter with a vertical polarization axis), the unpolarized light becomes vertical polarized light, it goes through the object O under detection, here it represents cardiac fiber sample, the light is repolarized and is transmitted into the analyzer A (the other polarization filter with a polarization axis perpendicular to that of P), the light after A is received by the camera and finally forms one image I. At the top, because the orientation of the fiber is parallel to the polarization axis of P, the vibration axis of the repolarized light is not modified by the cardiac fiber, thus the light is totally blocked by A, and the image formed is black. At the bottom, conversely, the fiber orientation is 45º related to the polarizer axis, the light transmitted from the cardiac fiber is modified, the light transmits the analyzer and forms a bright image.

When placed between crossed polars (Figure 2.3), the amount of transmitted light for a single fiber of known maximal birefringence is a function of the 3D orientation of the fibre. The amount of monochromatic light that reaches the analyzer (upper polar) is given by the Fresnel equation:

$$\frac{I}{I_0} = \sin^2 \pi \frac{\Delta}{\lambda} \times \sin^2 2\tau \tag{2.2}$$

where Δ is the retardation (the difference of time of travel across the fibre between the slow and the fast ray), λ the wavelength of the monochromatic light, λ the angle between the direction of the fibre and the closest direction of either polarizer or analyzer, and I_0 the intensity of light when unretarded (Δ=0). In practice, we do not deal with a single fibre, but with a tissue made of numerous fibres with different orientations that are to be measured. These orientations can be considered in terms of elevation angle and azimuth angle (Figure 2.4). The elevation angle corresponds to the angle between the fiber and the short-axis plane, while the azimuth angle represents the angle between the projection of the fiber in the short-axis plane and the +y axis.

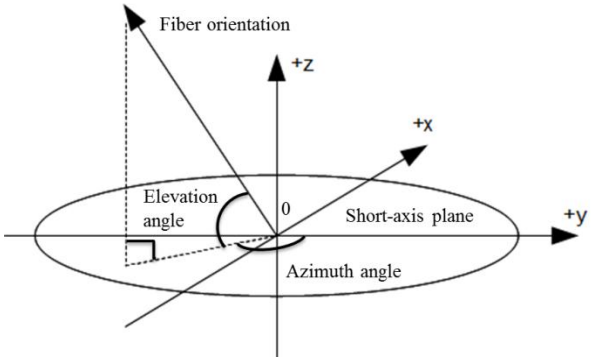

Figure 2.4. Definition of the elevation and azimuth angles of a fiber.

The experimental sample is a 40 weeks human fetus heart. We stated that for removing the influence of the collagen on the cardiac fiber uni-axial birefringence, the cardiac muscle sample must be processed with following specific steps according to the work of Jouk (Jouk et al. 2007):

1. The heart was immerged in a solution of 10% neutral buffered formalin for one week;
2. Infiltrated at room temperature with 2 solutions of glycol methacrylate (GMA) for one week;
3. Infiltrated again for another one week in a series of mixtures of GMA and MMA (methyl methacrylate), in which the concentration of MMA was gradually increased until reaching 100% MMA;
4. Embedded by polymerization of MMA at a temperature of 32ºC;
5. Drill 4 holes in the embedding resin for providing a 3D anatomical reference used in the further fiber orientation analysis;

6. Cut 43 heart sections of thickness 500 µm with a rotary microtome (1600, Leica).The rate of penetration of the rotatory saw is set to a low speed (15 min per section) in order to avoid mechanical stress and distortions.

Using the obtained images for different polarizer rotation angles, it is possible to calculate the azimuth and elevation angles of each cardiac fiber. The detection results are given in the form of selected maps of the elevation and azimuth angles of the myocardial muscles, as illustrated in Figure 2.5.

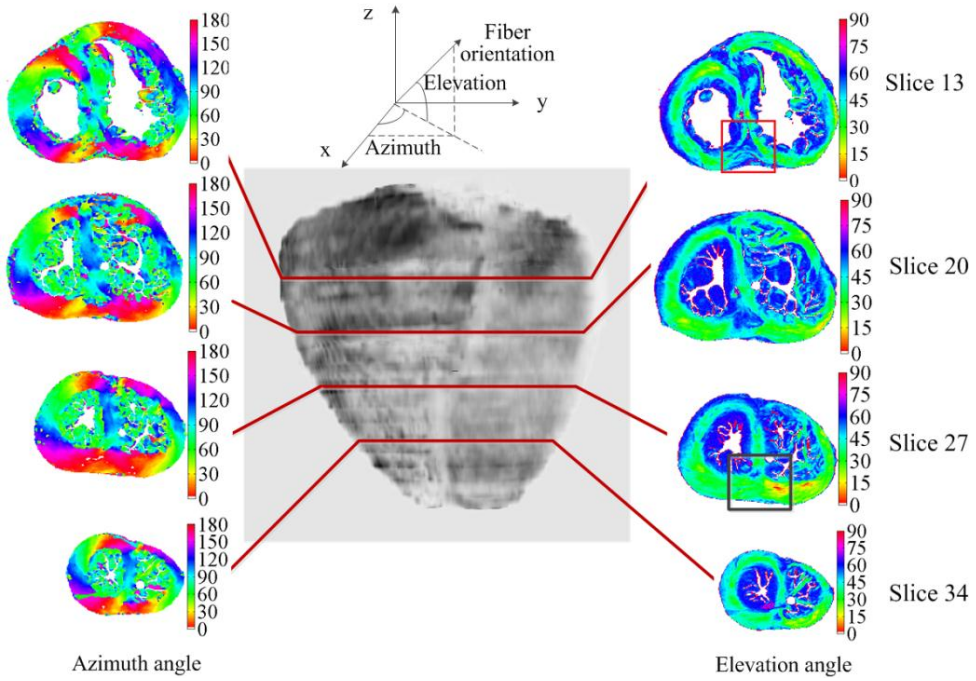

Figure 2.5. The fiber orientation expressed by the azimuth and elevation angles detected by PLI with a spatial resolution of 0.1 × 0.1 × 0.5 mm^3. The whole ventricle is sectioned into 43 slices. The azimuth and elevation angle maps for slices 13, 20, 27 and 34 are shown. The azimuth angle is coded in false color from 0º to 180º and elevation from 0º to 90º. (Jouk et al 2007)

It can be observed that the fiber at the diaphragmatic face of the heart has a 0º azimuth angle (red), and at the interventricular septum and lateral wall of the ventricles has an about 90º (blue) azimuth angle. The values of the azimuth angle vary in sympathy with the curvature of the left ventricular wall. While turning around the left ventricle the azimuth is rotating with a smooth progression from one color to the other. This means that the fibers are circumferential. A spiral anticlockwise arrangement is visible toward the apex, while the basal map shows a spiral arrangement with an inverse sense of rotation. As to the elevation angle, according to the slice location, two different fiber separate patterns between the left and right ventricles can be observed. For explaining, we make a comparison between the slices 13 and 27. The red square in the elevation angle map of slice 13 highlights the inferior part of the ventricular septum, where the medial circumferential fibers (green) of left and right ventricles converge into the circumferential medial part of the interventricular septum. However, for the

same part of slice 27 highlighted with a black square, the circumferential fibers of left and right ventricles are in either continuity or converging toward the interventricular septum.

2.2 Magnetic Resonance imaging (MRI)

We present the principle of nuclear magnetic resonance that is used to acquire magnetic resonance images (Hashemi 2004). Based on this acquisition technique, diffusion weighted magnetic resonance imaging has been developed to measure the average diffusion of water molecules in the tissue or a more complex model of diffusion with directional information.

2.2.1 MRI basis

It is well known that our body tissues contains a lot of water and hence protons ^{1}H. This little positive electrical charged proton behaves like a little planet, such as earth, it is constantly turning around an axis, which is called spin as shown in Figure 2.6(a). The spinning of the protons will generate a lots tiny magnets, in our body these tiny bar magnets are ordered in such a way that the magnetic forces equalize. However, when we put these protons in a much stronger magnetic field B_0, some interesting things happen, all the protons align with the magnetic field, parallel or anti-parallel, meanwhile, they precess or wobble due to the magnetic momentum of the atom, as illustrated in Figure 2.6(b). The precession frequency is called Larmor frequency (Levitt 2002) $\omega_0$which is determined by the strength of the magnetic field B_0 and the gyromagnetic ratio γ of proton ^{1}H.

$$\omega_0 = \gamma B_0 \tag{2.3}$$

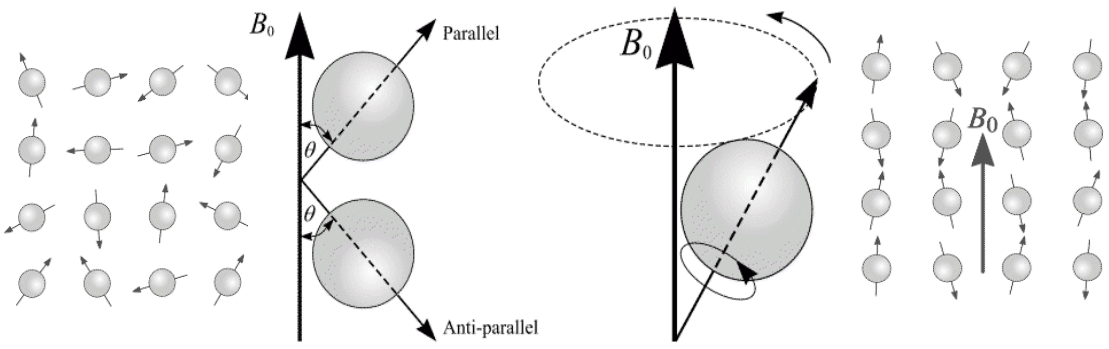

Figure 2.6. Nuclear Magnetic Resonance. (a) No external magnetic field. (b) Parallel and anti-parallel states within external magnetic field B_0. (c) Precession about the axis of the nagnetic field B_0 (d) within external magnetic field B_0
(*http://wikidoc.org/index.php/Basic_MRI_Physics*)

The ability to manipulate the direction of the net magnetization is what makes MR imaging possible. This manipulation is achieved by the application of time varying magnetic fields. These fields come in the form of radiofrequency (RF) pulses applied by a transceiver, and in

the form of magnetic field gradients. Consider first the application of RF pulses. If electromagnetic radiation at a frequency equal to γB_0 - Larmor (resonance) frequency - is applied to the sample, the protons will absorb the energy with a resulting reorientation of the spins. The tissue in fact sees this pulse of radiation as a temporary magnetic B_1 field. While the RF radiation is applied, the net magnetization vector will precess about the direction of B_1. If the RF radiation is of sufficient magnitude and duration and is applied at a right angle to the static B_0 field, the net magnetization vector can be made to precess until it reaches the transverse plane. Such a pulse of radiation is called a 90° RF pulse, and it begins the imaging protocols. The imaging process is descirbed below: once the B_1 field is turned off, the net magnetization vector lies in the transverse plane. Immediately it again begins to precess around the B_0 axis at the Larmor frequency (Figure 2.7). This rotating magnetization will induce a signal in an RF receiver tuned to the Larmor frequency as shown in the Figure 2.8. Note that the signal decays with time. This is because the individual spins that comprise the net magnetization vector initially precess together in phase.

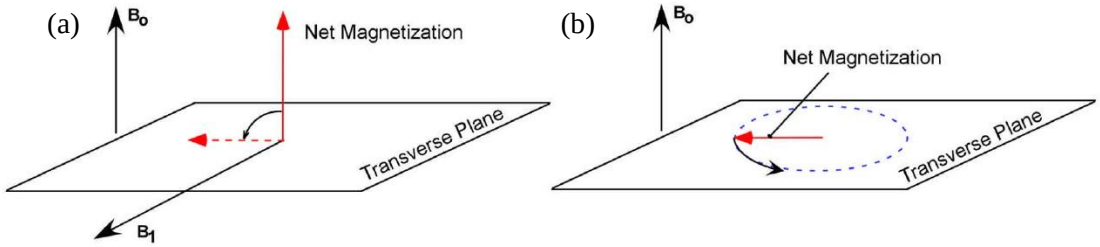

Figure 2.7. (a) Net magnetization before (solid line) and after (dashed line) application of a 90° RF pulse (B_1). (b)Pression of the net magnetization in the transverse plane anout the axis of B_0.

2.2.2 **Signal detection**

In MRI, the signal is produced by tipping the magnetization vector - $\overrightarrow{M_0}$ (the resultant sum of all angular momentum vectors) away from the static magnetic field B_0 with a radiofrequency field B_1 set at the Larmor frequency. If $\overrightarrow{M_0}$ is aligned along z and the B_1 field is applied along x, the magnetization vector then rotates around x axis of an angle α (the flip angle). The varying magnetic flux produced by the transverse magnetization $-\vec{M}$ through a nearby conductor loop induces a current in this conductor that can be measured. Figure 2.8 illustrates this process in a frame that is rotating at the Larmor frequency (referred to as the rotating frame).

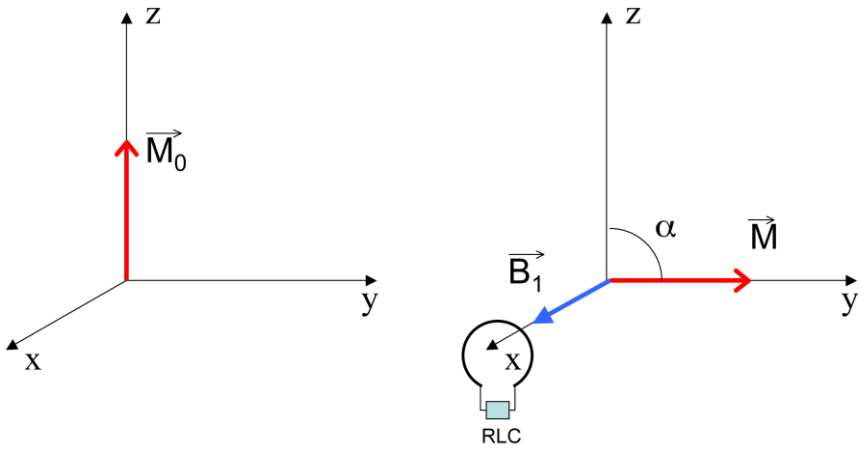

Figure 2.8. Illustration of RF excitation of the magnetization of vector $\vec{M_0}$ in the rotation frame. An RF pulse (B_1 field) is applied along x axis and tips $\vec{M_0}$ at 90° angle from z axis. A conductor loop measures the signal produced. (Delattre 2011)

The corresponding induced elecrtomotive force (emf) is given by:

$$emf = -\frac{d}{dt}\int \vec{M}(\vec{r},t) \bullet \vec{B}^{re}(\vec{r}) d\vec{r}, \tag{2.4}$$

where $\vec{B^{re}}$ is the received field produced by the detection coil at all the points where magnetization is non-zero. The dependance of the *emf* on the applied B_1 field is implicitly contained in the magnetization $\vec{M}$. Signal is proportional to the magnetization that is in turn proportional to the spin density ρ. After some simplifications, it can be expressed as:

$$s(t) = \int \rho(\vec{r}) e^{i(\omega_0 t + \phi(\vec{r},t))} d\vec{r}, \tag{2.5}$$

where ϕ(t) is the accumulated phase wxpressed as:

$$\phi(\vec{r},t) = \int_0^t \omega(\vec{r},t')dt'. \tag{2.6}$$

In the presence of only a static magnetic field B_0, $\omega = \omega_0$.

2.2.3 **Relaxation phenomenon**

When RF excitation stops, the magnetization vector tends to return to its original position along B_0 field due to interactions between the spins and their surroundings. This phenomenon is called spin-lattice relaxation and is governed by a specific relaxation time T_1. Another relaxation effect is given by the interaction between the spins themselves that causes a dephasing resulting in a reduction of transverse magnetization. This so-called spin-spin relaxation has a specifc T_2 relaxation time. These relaxation phenomenons are expressed by the Bloch equations:

$$M_x(t) = e^{-t/T_2}(M_x(0)\cos(\omega_0 t) + M_y(0)\sin(\omega_0 t)), \tag{2.7}$$

$$M_y(t) = e^{-t/T_2}(M_y(0)\cos(\omega_0 t) - M_x(0)\sin(\omega_0 t)), \tag{2.8}$$

$$M_z(t) = M_z(0)e^{-t/T_1} + M_0(1 - e^{-t/T_1}). \tag{2.9}$$

T_1 and T_2 parameters play an important role in contrast depending on the timing of the signal acquisition. In real conditions the transverse relaxation is also altered by interactions with local magnetic field inhomogeneities, this is called the T_2^* relaxation, with $T_2^* < T_2$. Figure 2.9 shows the signal measured after a 90° RF pulse, after the application of the RF pulse, the magnetization is decaying due to T_2^* relaxation. This signal is called free induction decay (FID). If we add after the 90° pulse a 180° RF excitation, the spins are refocused and produce a signal called the echo. This sequence called "spin echo", can be repeated over the time to produce an image. If we define echo time (TE) the time between the 90° excitation pulse and the maximum amplitude in the signal echo, and repetation time (TR) the time separating two consecutive repetitions, the transverse magnetization (which represents the acquired signal intensity) is given by:

$$M_{xy}(TE) = M_0(1 - e^{-TR/T_1})e^{-TE/T_2}. \tag{2.10}$$

Myocardial tissue reveals significant differences in cardiac diseases compared with a healthy volunteer. Therefore, T1 and T2 maps of the myocardium are very important in the clinical applications.

Table 2.1 T2 and T1 relaxation times at 3T and 1.5T measured at 37°C. (Stanisz et al. 2005)

Tissue	T2-3T [ms]	T1-3T [ms]	T2-1.5T [ms]	T1-1.5T [ms]
Liver	42 ±3	812 ±64	46 ±6	570 ±30
Heart	47 ±11	1471 ±31	40 ±6	1030 ±34
Kidney	56 ±4	1194±64	55 ±3	690 ±30
White matter	69 ±3	1084 ±45	72 ±4	884 ±50
Gray matter	99 ±7	1820 ±114	95 ±8	1124 ±50
Optic nerve	78 ±5	1083 ±39	77 ±9	815 ±30
Blood	275 ±50	1932 ±85	290 ±30	1441±120

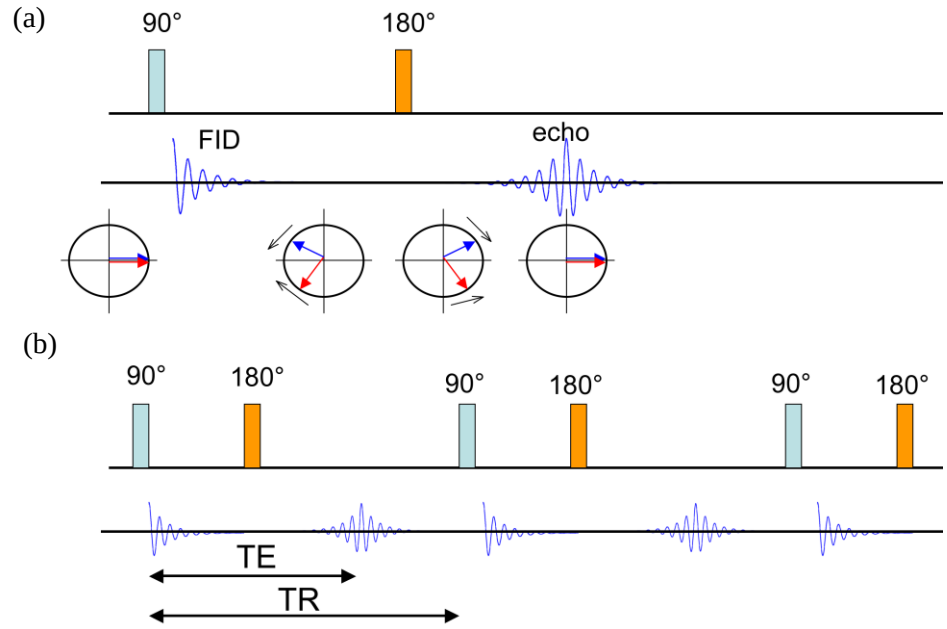

Figure 2.9. Illustration of spin echo. (a) FID signal measured after 90° pulse, spin refocalizaion after the 180° pulse and echo formation, schematic representation of 2 spins with different rotating frequencies in the transverse plane to illustrate the refocalization process. (b) Repetitions of the spin echo, definition of TE and TR.

2.2.4 **Spatial encoding of information**

As seen above, signal is related to the spin density image where the precessing frequency ω depends on the static magnetic field. To spatially discriminate the signal of protons, the position of each spin along one direction, for example z, can be encoded with a spatially varying magnetic field along that direction. The proton's precessing frequency now depends on that gradient G:

$$\omega(z,t) = \omega_0 + \omega_G(z,t), \tag{2.11}$$

$$\omega_G(z,t) = \gamma z G(t). \tag{2.12}$$

Figure 2.10 illustrates this priniciple in the case of a gradient applied along the field direction z. Similarly, gradients can be applied in x and y directions to encode spatially the spin in the transverse plane. If we define $k(t)$ as:

$$\vec{k}(t) = \gamma \int_0^t \vec{G}(t')dt', \tag{2.13}$$

The signal is thus expressed as:

$$s(\vec{k}) = \int \rho(\vec{r}) e^{-i2\pi \vec{k}\cdot\vec{r}}. \tag{2.14}$$

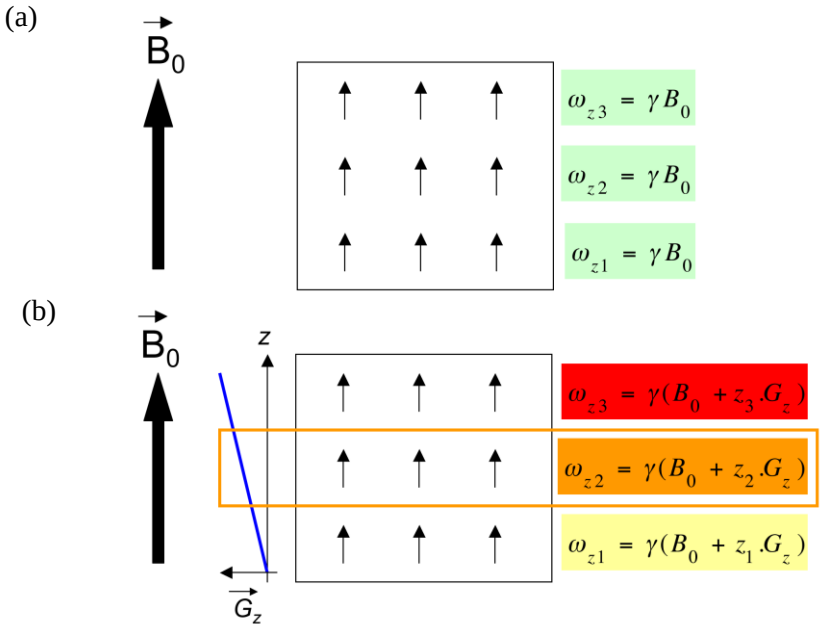

Figure 2.10. Illustration of slice selection with application of a gradient. (a) Precession frequency of spins in all the volum is the same, (b) after application of a gradient in z direction, spins rotate at different frequencies along z. (Delattre 2011)

Relation 2.14 describes the signal as the Fourier transform of the spin density ρ. The domain of spatial frequency of the signal is refered to as the k-space. Figure 2.11 illustrates the relative importance of low spatial frequencies and high spatial frequencies in the image composition. Most of the energy of the image is contained in the center of k-space whereas the details of the image are encoded into the high frequencies.

Signal acquisition in MR is most of the time performed line-by-line in k-space, a sequential process that requires a long time to sample the entire k-space (Moratal et al. 2008). In order to reduce the scan time and make the images less affected by motion, parallel imaging methods have become commonly used. By using the multiple receiver channels, the experiments can be accelerated with a good image quality. Currently, the most well known are SENSE (Van Heeswijk et al. 2012) and GRAPPA (Griswold et al. 2002). SENSE is based on the fact that receiver sensitivity generally has an encoding effect complementary to Fourier preparation by linear field gradients. Thus, by using multiple receiver coils in parallel scan time in Fourier imaging can be considerably reduced (reconstruction in the frequency domain). GRAPPA is a parallel imaging technique to speed up pulse sequences. The Fourier plane of the image is reconstructed from the frequency signals of each coil (reconstruction in the image domain). Algorithms of the GRAPPA type work better than the SENSE type in heterogeneous body parts like thoracic or abdominal imaging, or in pulse sequences like echo planar imaging. This is caused by the differences between the sensitivity map and the pulse sequence (e.g. artifacts). The major negative point of parallel imaging techniques is that they diminish SNR in proportion to the numbers of reduction factors.

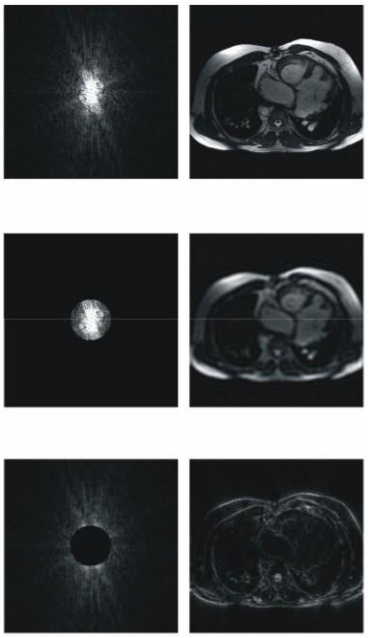

Figure 2.11. Representation of low and high spatial k-space frequencies (left) and their effects on the images (right). Upper, fully acquired k-space and the Fourier reconstructed image. Middle, Fourier transforming only the center of k-space results in high-contrast features and low-resolution image. Lower, Fourier transforming of k-space periphery results in fine resolution detail. (Moratal et al. 2008)

2.2.5 **Cardiac magnetic resonance (CMR) principles**

Since the signal acquisition in MR is most of the time performed line-by-line in k-space, it takes a certain time to sample the entire k-space. The acquisition duration is often not compatible with requirements of imaging moving objects. In cardiac imaging, one of the strategies is to segment the k-space sampling and to trigger the acquisition onto physiological information like the R-wave of the ECG. Figure 2.12 represents the complete acquisition of k-space segmented over several heartbeats. With this technique, it is possible to acquire consecutive packets of data during each R-R cycle, which give temporal information to the resulting images, as it is illustrated in the Figure 2.12. The reconstruction of all the collected k-space informations give a movie of the beating heart, referred to as “cine” (Schülen et al. 1996). To avoid the respiratory motion artifacts into the final images, we often perform this sequence under patient breath-hold. Another technique if the patient is unable to retain his respiration during 10 to 20 seconds is to perform the acquisition with a respiratory navigator (Firmin & Keegan 2001) in order to reconstruct only data that were acquired at the same phase of the respiratory cycle.

The cine sequence is the standard sequence for the evaluation of myocardial function (Lee et al. 2002) and is considered as a diagnostic technique. Contraction deficit due to a myocardial infarction, for example, is visible when the movie is played and measurements such as LV cavity volume or wall thickening between diastole and systole are performed on

the images and are considered as diagnostically relevant by a consensus of scientists and healthcare professionals.

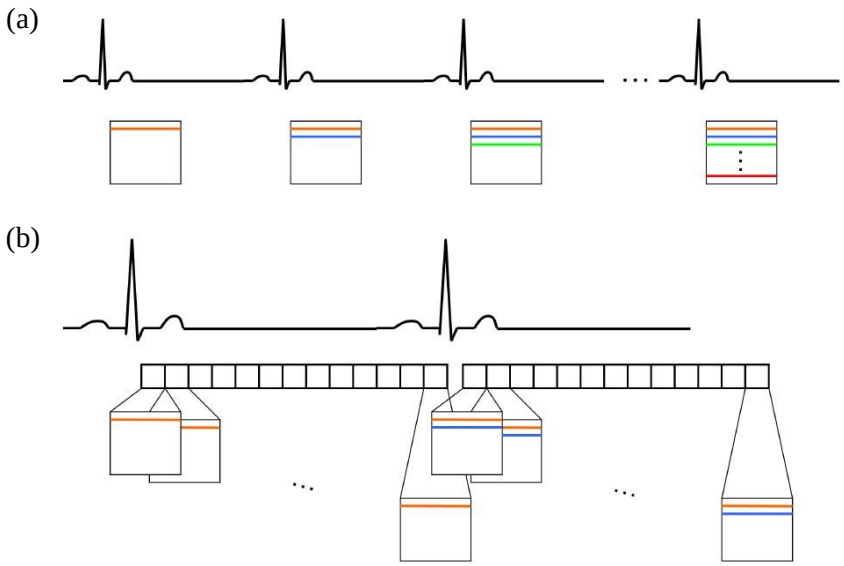

Figure 2.12. Schematic representation of k-space sampling in cine sequence. (a) Acquisition of one phase of the cardiac cycle; (b) the acquisition is performed for each cardiac phase and is repeated until the entire k-space is sampling.

2.2.6 **Advanced CMR techniques to investigate heart fucntion**

MRI pulse sequences enable us to control the way in which the system applies pulses and gradients. In this way, the image contrast type and quality is determined. There are many different MRI sequences available, and each is designed for a specific purpose (Bernstein et al. 2004). MRI tissue tagging is now widely available in clinical scanners, and is typically performed using the spatial modulation of magnetization (SPAMM) technique. This technique saturates parallel bands of tissue as a result of combining RF pulses with short gradient waveforms to create saturated magnetization vectors (Ennis et al. 2008). These dark bands follow the deformation of the underlying myocardium, thus creating high contrast image features that track with heart wall deformation throughout the cardiac cycle. Post-processing of the tagged MR images allows reconstruction of the 3D motion of the heart from the tag positions during the cardiac cycle. Recovering deformation information from the images requires high-resolution images, and specialised image processing and mathematical techniques.

On the other hand, displacement encoding with stimulated echoes (DENSE) (Aletras et al. 1999) sequences can provide high spatial resolution 3D displacement fields of the human heart in vivo.

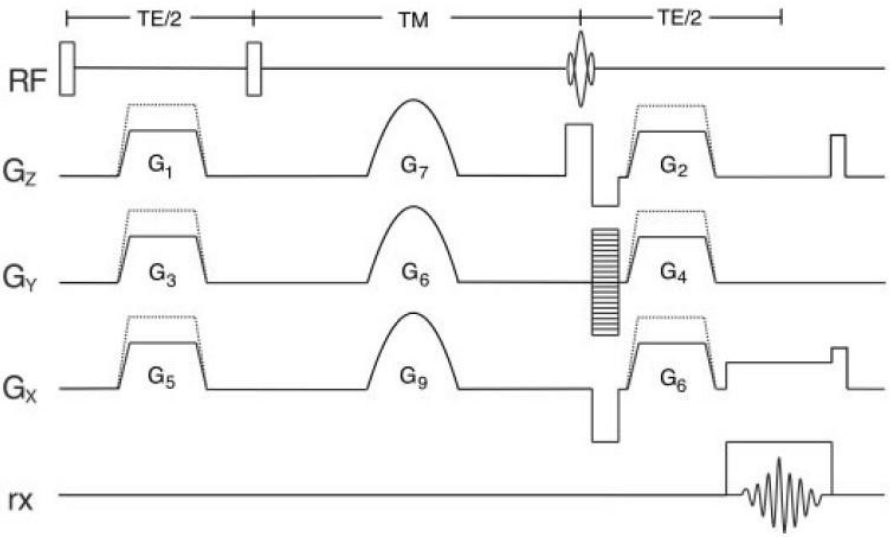

Figure 2.13. DENSE pulse sequence. Spin phase wrapping occurs through the application of gradient pulses G_1, G_3, and G_5. The corresponding gradient pulses G_2, G_4, and G_6 totally unwrap the phase for static tissue. Spins that have moved during the TM period will retain phase as described in the text.

The basic pulse sequence is schematically presented in Figure 2.13. After an initial RF excitation, phase dispersion was introduced with a single gradient lobe along the desired direction. For example, along the read direction the gradient pulse was set at G_5 G/cm and duration t_{enc}. Subsequently, a second RF pulse was applied to preserve the magnetization along the longitudinal axis. Displacement was encoded during a long mixing period TM followed by a third RF pulse that brought the magnetization onto the transverse plane. There, a second gradient pulse of amplitude G_6 (where $G_5 = G_6$) rewound the phase dispersion from the first lobe. For stationary spins this phase rewinding was complete. For spins that had moved Δx between G_5 and G_6 along the read direction, a phase of $\phi_1 = \gamma_H G_5 t_{enc} \Delta x$ was accumulated. Imaging was performed with slice selection during the third RF pulse followed by sequential k-space sampling at one view per excitation. The sequence was repeated once more with altered amplitude of the position sensitizing gradient pulses (where $G^*_5 = G^*_6$). The phase accumulated was then $\phi_2 = \gamma_H G^*_5 t_{enc} \Delta x$. The phase difference between the images was $\Delta\phi = \gamma_H(G_5 - G^*_5)t_{enc} \Delta x$. This equation was used to measure Δx. Other phase contributions common to both images were canceled. Since Δx occurred over approximately 100 ms, large phase differences $\Delta\phi$ were obtained with moderate encoding gradient pulses. To measure displacement along the read and slice directions, the corresponding encoding gradient amplitudes were modified accordingly.

DENSE magnitude images exhibit good contrast and spatial resolution (pixel based information on deformation) which allows for better understanding of myocardial regional function (Figure 2.14).

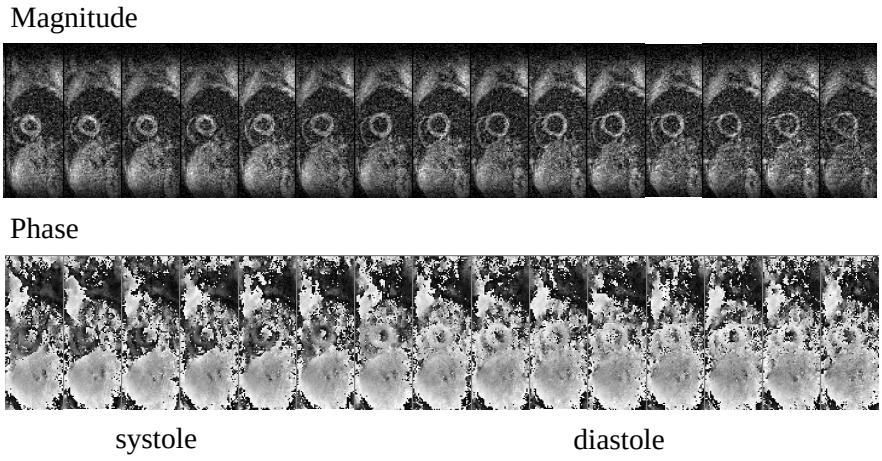

Figure 2.14. Magnitude and phase maps of DENSE at systole and diastole.

2.3 Diffusion tensor imaging (DTI)

2.3.1 Diffusion physics

Brownian motion

Diffusion is a mass transport process arising in nature, which results in molecular or particle mixing without requiring bulk motion. “Diffusion” in biological tissues usually means “molecular diffusion”, also called Brownian motion, which refers to the random motion of water molecules when they are agitated by thermal energy. The Brownian motion is usually described by the random walk model (Knight 1961), which not only gives the trajectory of molecular diffusion, but also the diffusion displacement during a given time interval, as shown in Figure 2.15.

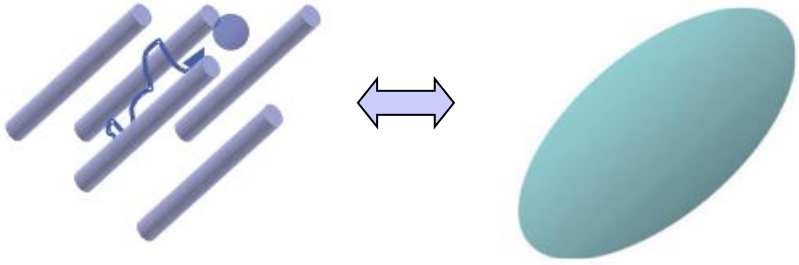

Figure 2.15. Biological cells may hinder the Brownian motion of extracellular water molecules.

2.3.2 Diffusion MR techniques

The effects of diffusion on the MRI signal was first noticed by Hahn in 1950 (Hahn 1950). Few years later, Torrey (Torrey 1956) presented a generalized version of the Bloch equations which incorporated the elements of molecular diffusion. He pointed out that in the presence of molecular diffusion, the transverse magnetization variation is

$$\frac{d\overrightarrow{M}}{dt} = \gamma \overrightarrow{M} \times \overrightarrow{B}_0 + \begin{pmatrix} \frac{M_x}{T_2} \\ \frac{M_y}{T_2} \\ \frac{M_0 - M_z}{T_1} \end{pmatrix} + D\nabla^2 \overrightarrow{M}, \qquad (2.15)$$

where ∇^2 signifies the Laplace operator, the first two terms in this equation come from the original Bloch equation, the third term accounting for molecular diffusion. The complete equation is called Bloch-Torrey equation. In order to detect the molecular diffusion information, the original MRI pulse sequence was altered and produced another imaging modality, which is called diffusion weighted magnetic resonance imaging (DWI) (Mori & Barker 1999).

All MRI pulse sequences are to some extent sensitive to molecular motion and diffusion, however, a specific diffusion measurement diffusion sequence was developed by Stejskal and Tanner in order to extract the diffusion information (Stejskal & Tanner 1965). This sequence (Figure 2.16) is designed based on a spin echo (SE) sequence, one symmetric pair of diffusion-weighted gradients is added to either side of the refocusing 180° RF pulse in each encoding directions (slice selection, phase and frequency encoding).

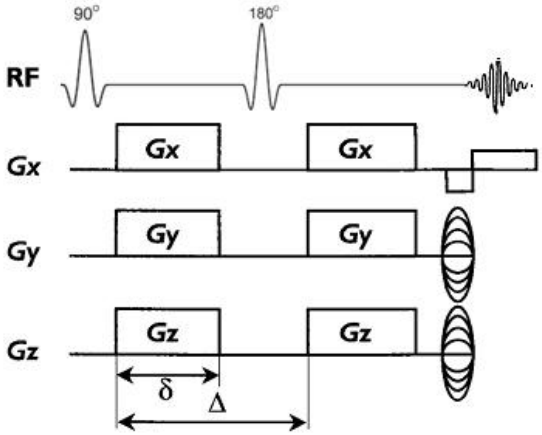

Figure 2.16. Stejskal-Tanner diffusion magnetic resonance imaging sequence

The different magnitudes of the diffusion-weighted gradients in the three encoding directions will provide a specific diffusion-weighted direction corresponding to the encoding coordinate system. The first of these gradients offsets the phase of the spins by an amount that depends on their location, the second will provide equal and opposite (due to 180° pulse) rephasing if the spins have not moved during the diffusion time Δ, which is the time between the application of the two gradients. As the spins move randomly due to diffusion, the rephasing effects of 180° will disappear. The further the spins have diffused during the diffusion time, the less perfectly rephasing and the smaller the amplitude of the final signal will be. More diffusion information can be indicated by a more attenuated signal.

Diffusion imaging is therefore a unique MR imaging technique that can non-invasively quantify the water displacement in the encoding direction (the direction where the diffusion gradient is applied and so called Diffusion weigthed imaging: DWI); it can also exploit the directionality of diffusion to provide non-invasive characterization of tissue architecture (diffusion tensor imaging: DTI).

2.3.3 **Single shot spin echo EPI**

The echo planar (EPI) is the fastest acquisition method in MRI (100 ms / slice), but with limited spatial resolution. It continuous signal acquisition in the form of a gradient echo train, to acquire total or partial k-space (single shot or segmented acquisition). To constitute the gradient echo train, a readout gradient is continuously applied, with positive and negative alternations. In the case of an alternating gradient (blipped and nonblipped EPI), k-space will be scanned from left to right and back, with each echo. At the same time, the phase encoding gradient may be permanent and constant (nonblipped) giving a zigzag global trajectory, or intermittent (blipped) at each echo onset, giving a rectilinear trajectory. The artifacts in echoplanar sequences are linked to: 1) sensitivity to magnetic susceptibility, which can be reduced by using segmented rather than single-shot sequences, at the cost of increasing scan time. 2) Gradient imperfections (particularly induced currents) perturb spatial encoding, leading to ghost images. EPI sequences are the basis for advanced MRI applications such as diffusion, perfusion and functional imagery.

Bipolar acquisition (Figure 2.18) with positive and negative encoding gradient lobes is used to acquire echoes (this is normal EPI behaviour: positive, negative, positive, negative, etc, with phase encoding blips between each). It is faster because we use all the echoes. Mononpolar acquisition (Figure 2.17) means echoes are recorded for only positive (or only negative) gradient lobes, and so the acquisition is slower. The benefit of monopolar is that if there are different phase errors between the positive- and negative-gradient echoes, or changes in amplitude, these alternating errors will not be present in the final data set (so no Nyquist ghosting). The eddy current compensated by bipolar diffusion encoding scheme implemented allows for reliable diffusion imaging with low spatial distortions.

The b value for the monopolar sequence is

$$b = \left(\gamma \bar{G} \delta\right)^2 (\Delta - \delta / 3) \tag{2.16}$$

while for the bipolar sequence, the b value is calculated

$$b = \gamma^2 \int_0^{\tau} \left(\int_0^{t} G(t') dt' \right)^2 dt \tag{2.17}$$

where γ is the gyromagnetic ratio and G represents the effective gradient strength as a function of time. B value calculation for bipolar diffusion encoding is more complex.

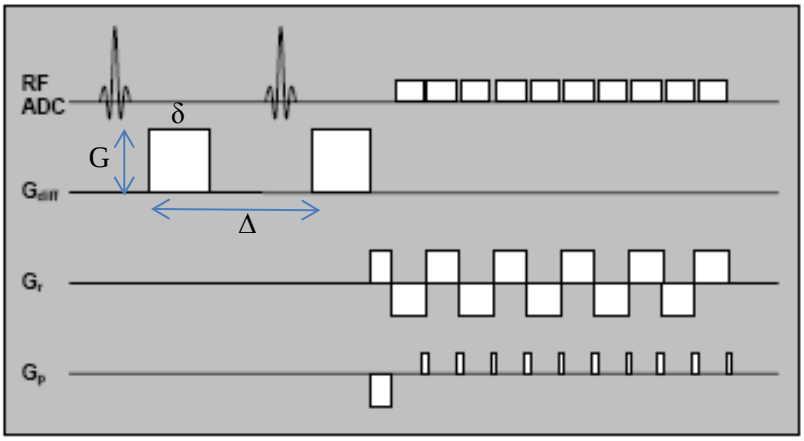

Figure 2.17. Schematic timing diagram of the monopolar diffusion encoding scheme.

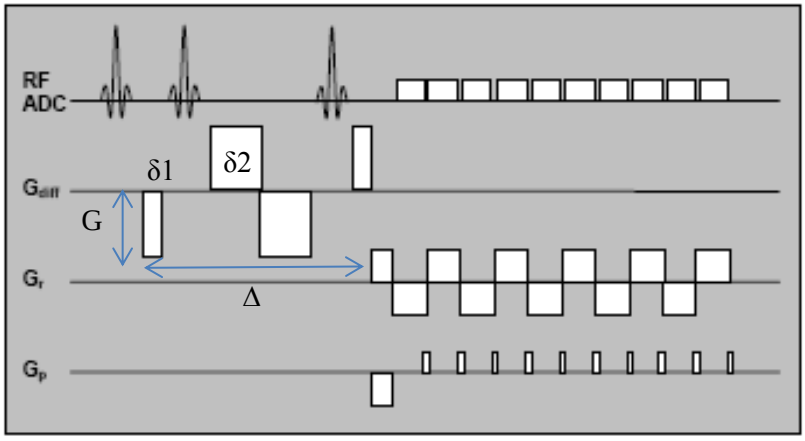

Figure 2.18. Schematic timing diagram of the bipolar diffusion encoding scheme.

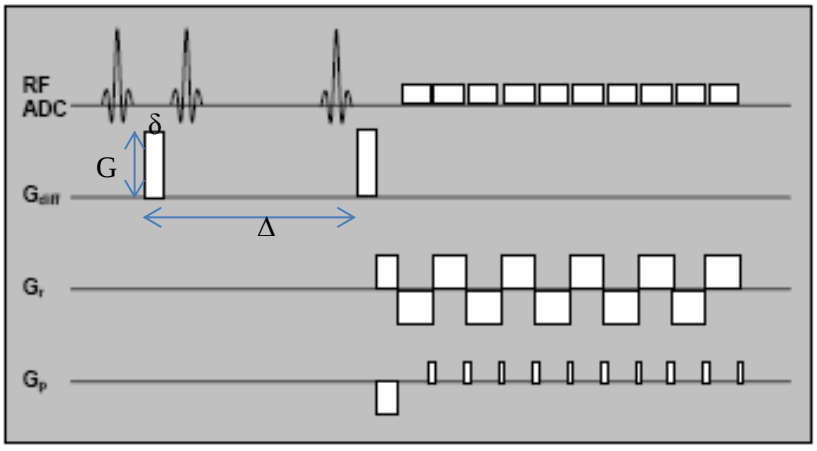

Figure 2.19. Schematic timing diagram of the STEAM diffusion encoding scheme. With three 90° pulses, the signal of the stimulated echo is used for imaging.

STEAM sequence (Figure 2.19) runs over two heartbeats, and makes the assumption that the heart is in the same position at both diffusion-encoding times on consecutive cardiac cycles. That means the STEAM sequence for the cardiac acquisition is an increased scan time.

2.3.4 **Diffusion models**

A mean isotropic diffusion image (so called «Trace Image») only requires three orthogonal directions of diffusion investigated using a 2D multislice acquisition. It is a very short sequence; the main clinical application is oncology (brain but also whole body MRI). A basic fit provides the directionally averaged apparent diffusion coefficient (ADC). In the case of isotropic diffusion, the diffusion process is simply described by a single scalar parameter, the ADC. However, in presence of diffusion anisotropy, diffusion effect can no longer be characterized by a single ADC, but requires other parameters able to fully describe the molecular diffusion along each spatial direction. Thus the concept of diffusion tensor $\overline{D}$ was introduced into DWI (Basser et al. 1994) and leading to DTI. More than three orthogonal gradient directions need to be acquired, and DTI acquisition can vary from low angular (6-30 directions, $2\times2\times2mm^3$) to high angular isotropic $1mm^2$ resolution). The tensor model (Le Bihan 1995) yields several quantitative parameters reflective of tissue microstructure. The most common are the scalar metrics, mean diffusivity (MD) and fractional anisotropy (FA), which are rotationally invariant parameters reflecting the degree of (directionally averaged) diffusivity and anisotropy, respectively. MD is the tensor equivalent of the ADC in DWI. The largest (major) eigenvalue is often called parallel diffusivity, as it is presumed to reflect the magnitude of diffusion parallel to axons. The average of the 2 lesser (medium and minor) eigenvalues is often called radial, transverse, or perpendicular diffusivity, as it is presumed to reflect the magnitude of diffusion perpendicular to axons (assuming of a single population of unidirectional axons within the imaging voxel).

Other model such as Orientation distribution functions (ODF) aim at circumventing the limitation of the tensor model in voxel showing crossing of the major pathways. Inded, DW and DT imaging measure the mobility of water molecules, assuming a process of random, unrestricted but potentially hindered, diffusion. The diffusion probability distribution function (PDF) i.e. the chance of a particular proton diffusing from one location to another in a given time interval, is thus considered a Gaussian PDF, with the standard deviation relating to the apparent diffusion coefficient. However, the complexity of the biologic cytoarchitecture—determined by, for example, cell membranes, intracellular organelles, and the rapid exchange of protons between different compartments will inhibit random Brownian motion and thus causes water diffusion to deviate from strict Gaussian behavior.

Clinical applications of DW and DTI imaging are multiple in the brain and arising in the heart, Given that this theis focuses on DTI in the heart, we specially focus on the diffusion tensor model and DTI.

The diffusion tensor model and DT Imaging

In DTI, the diffusion magnetic resonance signal is expressed by (Le Bihan 1995)

$$E(b) = S_0 \exp(-b\overline{D}) \tag{2.18}$$

where b characterizes the gradient pulses used in the MRI sequence, including the gradient amplitude G, the gradient impulse duration δ and the diffusion time Δ. In the spin echo sequence (Stejskal & Tanner 1965), the b value is calculated by:

$$b = \left(\gamma \overline{G} \delta\right)^2 (\Delta - \delta / 3) \tag{2.19}$$

with γ designating the gyromagnetic ratio of ^{1}H proton S_0, the magnetic resonance signal intensity when $b = 0$ and the diffusion tensor given by

$$\overline{D} = \begin{pmatrix} D_{xx} & D_{xy} & D_{xz} \\ D_{yx} & D_{yy} & D_{yz} \\ D_{zx} & D_{zy} & D_{zz} \end{pmatrix} \tag{2.20}$$

According to the thermodynamic laws (Groot & Mazur 1962), the diffusion tensor of water molecules is thought to be symmetrical ($D_{ij} = D_{ij}$, with $i, j = x, y, z$).

Because the diffusion tensor $\overline{D}$ is symmetrical, the diffusion signal becomes:

$$E = S_0 \exp(-b_{xx}D_{xx} - b_{yy}D_{yy} - b_{zz}D_{zz} - 2b_{xy}D_{xy} - 2b_{xz}D_{xz} - 2b_{yz}D_{yz}) \tag{2.21}$$

The logarithm of the diffusion signal E is

$$\ln(E) = \ln(S_0) - b_{xx}D_{xx} - b_{yy}D_{yy} - b_{zz}D_{zz} - 2b_{xy}D_{xy} - 2b_{xz}D_{xz} - 2b_{yz}D_{yz} \tag{2.22}$$

For convenience, the right-hand side of Eq.2.20 can be written as

$$\ln(E) = BX \tag{2.23}$$

where

$$B = (-b_{xx}, -b_{yy}, -b_{zz}, -2b_{xy}, -2b_{xz}, -2b_{yz}, 1) \tag{2.24}$$

$$X = [D_{xx}, D_{yy}, D_{zz}, D_{xy}, D_{xz}, D_{yz}, \ln(S_0)]^{\mathrm{T}} \tag{2.25}$$

In order to obtain the six components of the diffusion tensor, the diffusion signal should be measured in at least six different diffusion angles (projections) corresponding to six different gradient directions.

$$\ln(E_i) = B_i X \tag{2.26}$$

where $i = 1, ..., M$, with $M \geq 6$. When $M = 6$, The diffusion tensor can be calculated directly through the following equation.

$$X = B_i^{-1} \ln(E_i) \tag{2.27}$$

When the number of acquisition directions is more than six, there is no true inverse B_i^{-1}, but Eq. 2.25 can still be solved by calculating a pseudo inverse matrix B^{Ψ} (Langlet 2006)

$$B^{\Psi} = (B^{\mathrm{T}} B)^{-1} B^{\mathrm{T}} \tag{2.28}$$

Consequently, the components of the diffusion tensor are computed from:

$$X = (B_i^{\mathrm{T}} B_i)^{-1} B_i^{\mathrm{T}} \ln(E_i) \tag{2.29}$$

Once the diffusion tensor is calculated, some diffusion parameters should be extracted for explaining the structures of the diffusion environment. Generally, concerning diffusion in biological tissues, especially in the cardiac fibers, we mostly care about the main direction of diffusion, the local mean diffusivity, fractional anisotropy, and fiber tractography.

Main direction of the diffusion

DTI is often used to detect the privileged orientations within tissues. Mathematically, a tensor is often represented by an ellipsoid (Basser 1995) with its three main axes called eigenvectors. Each eigenvector corresponds to one eigenvalue, expressed by λ. It is assumed that the direction of the eigenvector associated with the largest eigenvalue of the tensor corresponds to the local orientation of the tissue (Figure 2.20). The diffusion orientation extracted from DTI is commonly used for doing fiber tracking in the brain (Mori et al. 2002; Le Bihan 2003; Hüppi & Dubois 2006; Assaf et al. 2008), sometimes in the heart muscle (Zhukov & Barr 2003; Sosnovik et al. 2009) and some other tissues.

Mean Diffusivity (MD)

Mean diffusivity is often used in DTI. It represents the overall mean-squared displacement of the water molecules and gives information about the overall presence or not of obstacles to the diffusion in one voxel or one region. It is defined by the average of the three ADCs, respectively, measured along the three axes of the tensor. Assuming that the tensor axes along x, y and z, then the MD is written as:

$$MD = (ADC_x + ADC_y + ADC_z) / 3 \tag{2.30}$$

From the mathematical point of view, the MD can also be calculated from the eigenvalues of the tensor

$$MD = (\lambda_1 + \lambda_2 + \lambda_3) / 3 \tag{2.31}$$

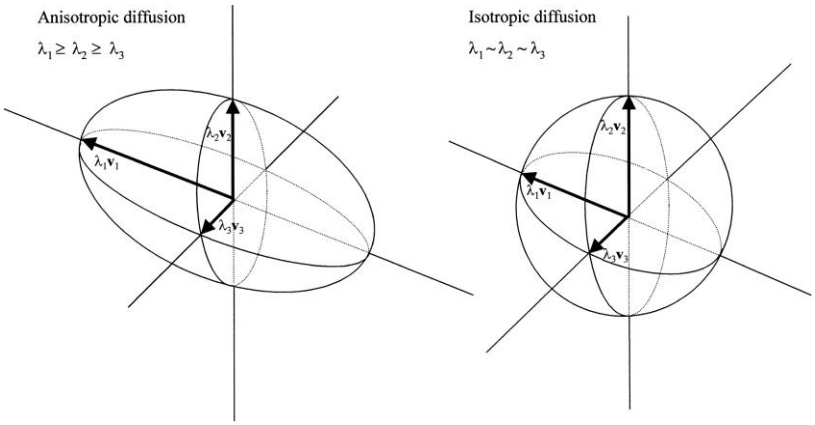

Figure 2.20. The probability function for water displacement can be depicted as an ellipsoid. The ellipsoid represents an isocontour of the 3D Gaussian solution to the diffusion equation. The axes are directed along the eigenvectors (v_1, v_2, v_3, principal diffusion orientations), and the lengths are scaled by the corresponding eigenvalues (λ_1, λ_2, λ_3, diffusion magnitudes). The eigensystem is conventionally ordered so $\lambda_1 > \lambda_2 > \lambda_3$, with anisotropic diffusion characterized by $\lambda_1 \geq \lambda_2 \geq \lambda_3$ and isotropic diffusion by $\lambda_1 \sim \lambda_2 \sim \lambda_3$.

Fractional Anisotropy (FA)

The fractional anisotropy describes the spatial heterogeneity of the water molecules displacements that is related to the presence of orientated structures (Pierpaoli & Basser 1996), it is defined as

$$FA = \sqrt{\frac{3}{2}} \sqrt{\frac{(\lambda_1 - MD)^2 + (\lambda_2 - MD)^2 + (\lambda_3 - MD)^2}{(\lambda_1^2 + \lambda_2^2 + \lambda_3^2)}} \tag{2.32}$$

Maps can be generated by calculating diffusion tensor derived indices on a voxel-by-voxel basis. Example of FA and MD maps are shown in Figure 2.21

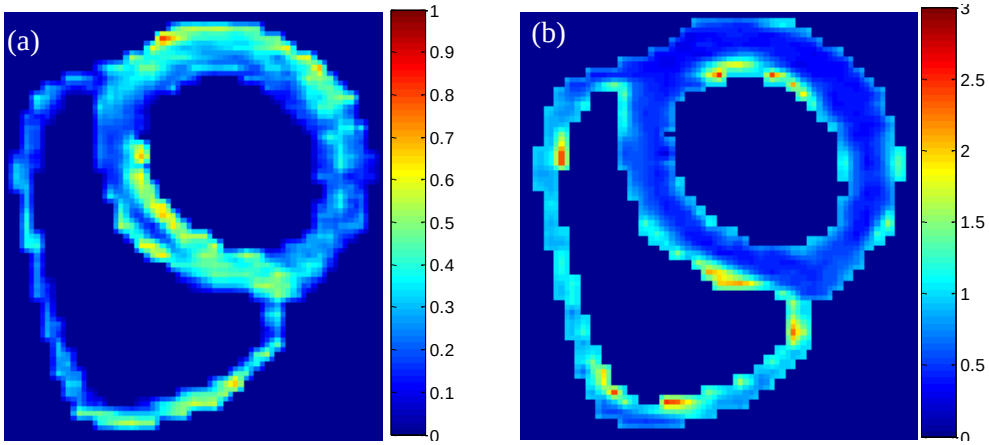

Figure 2.21. Maps of diffusion tensor derived indices of a healthy volunteer. (a) FA map describes degree of diffusion anisotropy in the heart. (b) MD map describes the average diffusivity in each voxel.

Intravoxel Incoherent Motion (IVIM) model

Signal intensity in DWI is affected by the Brownian motion of water molecules present in intra- and extra- cellular compartment (diffusion) but also to flow motion in vessels and capillaries (perfusion). The IVIM model allows the separation of the respective contribution of diffusing and flowing water molecules in the image and gives access thus to diffusion and perfusion characterization. The IVIM model has been used in dogs (Callot et al. 2003) but also the myocardium in in healthy volunteers (Delattre et al. 2012) (Figure 2.22).

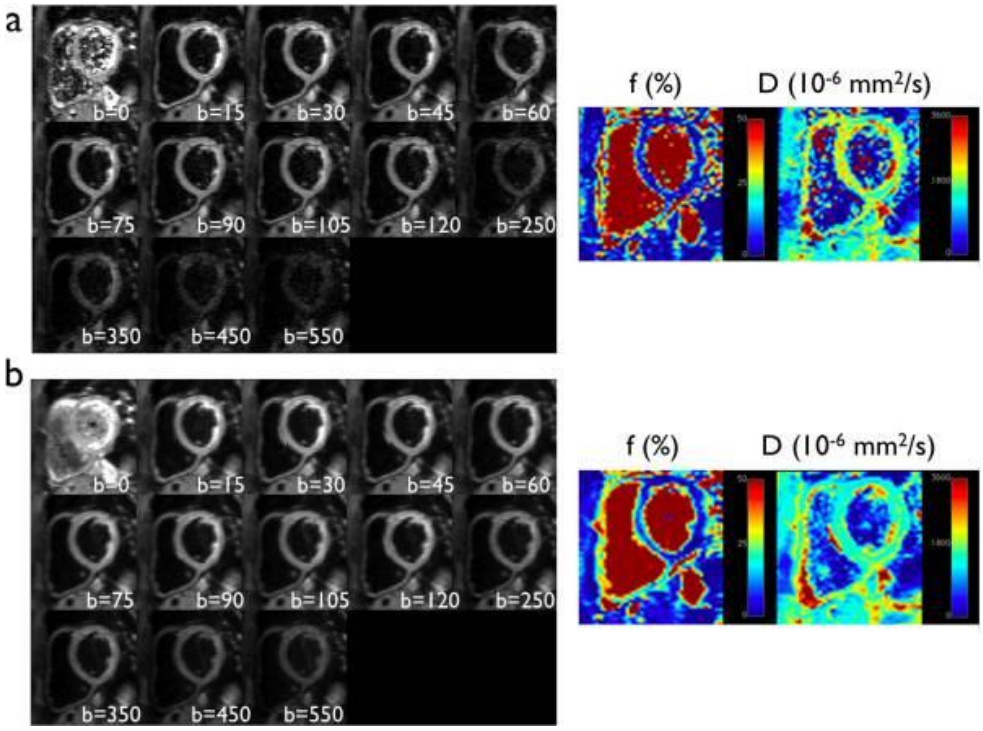

Figure 2.22. Trace DWI (multiple b value) for one volunteer (left and maps of perfusion fraction f and diffusion coefficient D (Delattre et al. 2012).

Fiber tracking

By following and connecting the principal eigenvector, which corresponds to the largest eigenvalue in each voxel, the orientation of cardiac fiber structure can be visualized. This technique is called fiber tractography, which provides the unique map of the tissues (Figure 2.23).

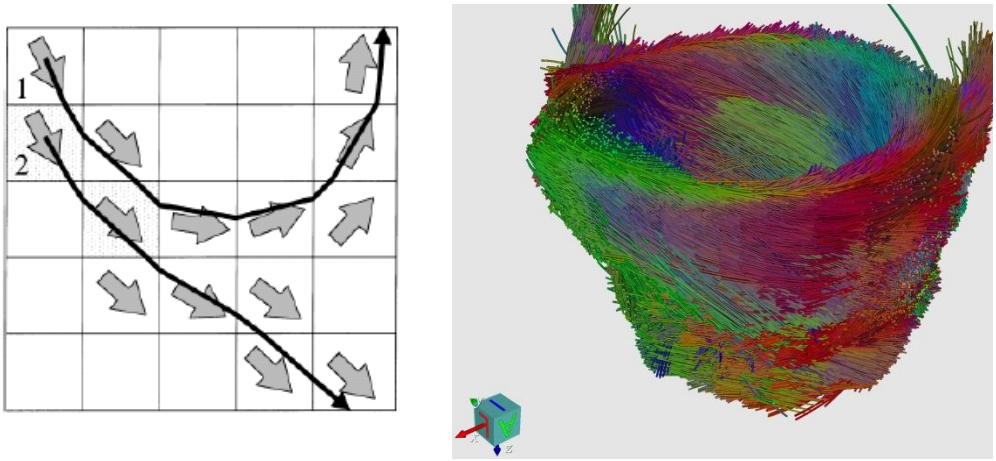

Figure 2.23. Schematic shows the basic idea of fiber tractography and an example of fiber tractography result of the heart of a healty volunteer.

2.3.5 **DW and DT Imaging techniques in the heart and today's challenges**

The overall motion of the heart is a complex mixture of cardiac motion associated with its cyclic pumping and respiratory motion which results in an additional twisting and volumetric distortion. The respiratory motion is relatively unpredictable and can vary considerably from person to person and from time to time. Cardiac motion has been well controlled over the years by detecting the ECG and triggering the acquisition at a certain delay. Obviously, ECG triggering works best when there is low variation between heartbeats; however, arrhythmias and ectopic hearts will cause artefacts. A moving object will change both the phase and magnitude of its k-space components. Motion during image acquisition will therefore introduce artifacts.

Today's challenge in cardiac DTI is the bulk motion of the patients. Image quality in MRI is strongly affected by motion. Therefore, motion is one of the most common sources of artefacts in contemporary cardiovascular MRI. Such artefacts in turn may easily lead to misinterpretations in the images and a subsequent loss in diagnostic quality. Hence, there is considerable research interest in strategies that help to overcome these limitations at minimal cost in time, spatial resolution, temporal resolution, and signal-to-noise ratio (SNR).

Breathing motion

The respiratory motion has been largely controlled by acquiring the data over the period of a breath-hold, although this can translate into a long acquisition window within the cardiac cycle, thus potentially including periods of more rapid cardiac motion. Most cardiac sequences are segmented, i.e. the acquisition of one image is divided into multiple heartbeats and the acquisition window in each heartbeat is restricted in order to reduce cardiac motion artefacts and blurring. On the other hand, respiratory motion introduces k-space inconsistencies between different segments. Breathing artifacts will depend on the phase-encoding order used, and the timing of the motion. If, for example, motion only occurred when sampling the edges of k-space, then motion artefacts would result in blurring of the

edges of the moving object in the phase encoding direction. If, on the other hand, the central regions of k-space were affected then this would result in a more significant ghosting and image degradation (Figure 2.24). In generally, if breathing motion is periodic during the acquisition of k-space in the phase encoding direction, it results in a number of defined "ghost" artefacts distributed in that direction on the image. As can be seen from Figure 2.24, for acquisition sequences that employ an interleaved segmented coverage of k-space then a single movement or drift in the respiratory position will have a similar impact to periodic breathing motion. On the other hand for sequences that acquire k-space in a block sequential manner a single movement, as long as it does not coincide with the centre of k-space, or similarly a drift in position, will cause some blurring but will generally cause less impact through ghosting. Different segmented sequences have different optimal phase-encoding orders, and therefore will be affected by respiratory motion differently. Generally, to avoid sudden signal amplitude and or phase discontinuities through k-space, which would lead to other artifacts, the Turbo-spin-echo, conventional gradient echo sequences acquire the data with an interleaved manner and the balanced SSFP sequences acquire in a block sequential manner. However, it should be noted that the exactly methods may vary between manufacturers and even for the same manufacturer over time.

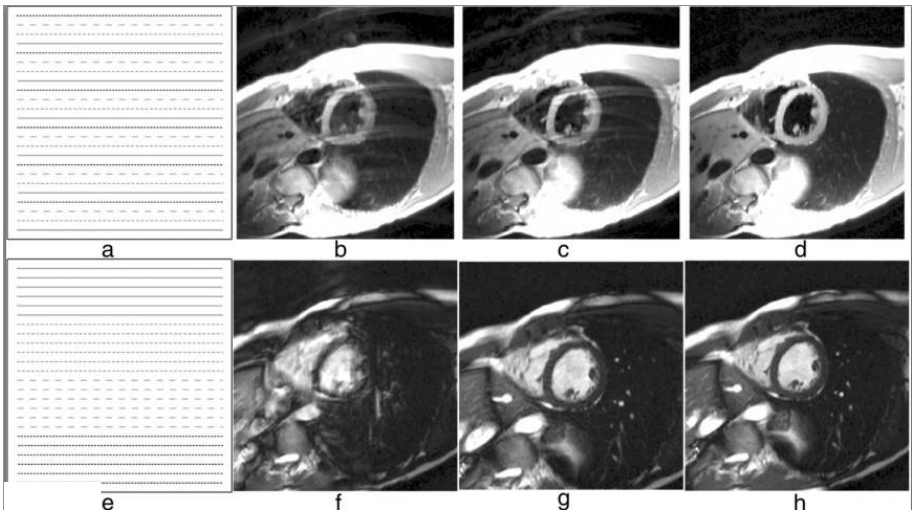

Figure 2.24. Breathing motion artifacts with two different phase-orders. This figure shows the artifacts caused by changes in respiratory position at different times during a breath-hold acquisition. (a) Shows an interleaved segmented phase-order, with 4 segments, each with 6 phase-encode lines, each line-type represents a different segment. (b) The effects of a respiratory movement in the middle of the acquisition. (c) The effects of a respiratory movement at the end of the acquisition. (d) A good breath-hold. e) Shows a block sequential phase-order case, with 4 segments, each with 6 phase-encode lines, each line-type represents a different segment. (f) The effects of a respiratory movement in the middle of the acquisition. (g) The effects of a respiratory movement at the end of the acquisition. (h) A good breath-hold. With a block sequential phase order the central region of k-space is acquired during a certain well defined period, and not spread throughout the whole acquisition window, therefore if no respiratory motion happens during this period, the artifacts are less conspicuous.(Ferreira et al. 2013)

To avoid breathing motion artifact problems, the total imaging time is kept short, and suitable for a breath-hold. If the patient is unable to hold their breath, the total imaging time needs to be reduced. Possible solutions include the use of parallel imaging, although the reduction of SNR in some applications such as the reduction of overall k-space lines acquired, thus reducing phase-encode spatial-resolution. Another solution is to reduce the temporal-resolution, increasing the data lines per cardiac cycle and the imaging window of each cardiac-phase. This may have the cost of increasing cardiac motion problems, especially if imaging during rapid cardiac motion stages.

Cardiac motion

Cardiac motion is another source of motion artefacts. Cardiac motion is mainly a problem in sequences where the data acquisition window includes periods of rapid cardiac motion, causing blurring or signal losses (Figure 2.25, Figure 2.26).

In order to minimize cardiac motion artefacts it is important to keep the DT image acquisition time as short as possible in each heartbeat. Possible approaches, therefore, include using a fast EPI readout, and/or parallel imaging. Additionnally imaging period need to be set in the portion of the cardiac cycle where the heart is relatively still.

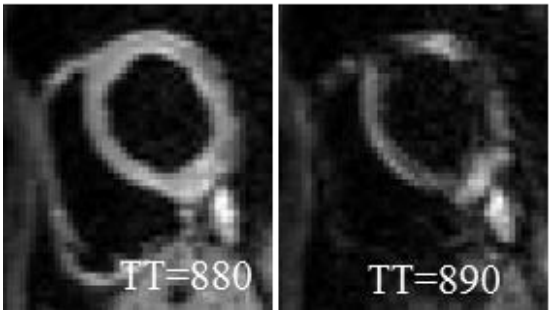

Figure 2.25. Cardiac motion introduces the signal losses of the DW images. The images are acquired in diastole, right image has a servere signal losses due to too much motion during scan.

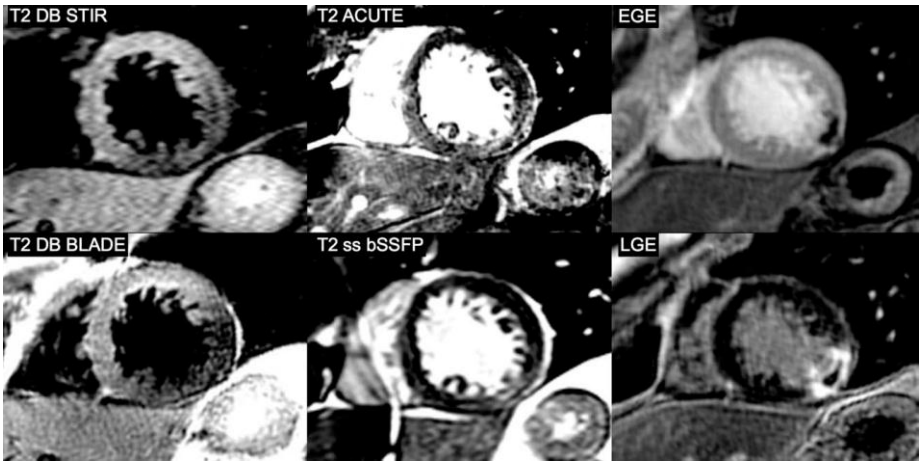

Figure 2.26. Intrascan motion artifacts in infero-lateral segment in the left images. (Viallon et al. 2011).

The signal loss is time dependent and spatial variable as seen in Figure 2.25. Therefore, it is difficult to acquire the accurate diffusion information at a signal phase. Figure 2.27 shows b=200 images sequentially obtained while shifting the acquisition window in the entire cardiac cycle. One can see that signal losses are very severe in the contraction and expansion phases of the heart, because the presence of bulk motion causes an additionnal attenuation to occur, in agreement with what has been described by Rappachi et al (Figure 2.28).

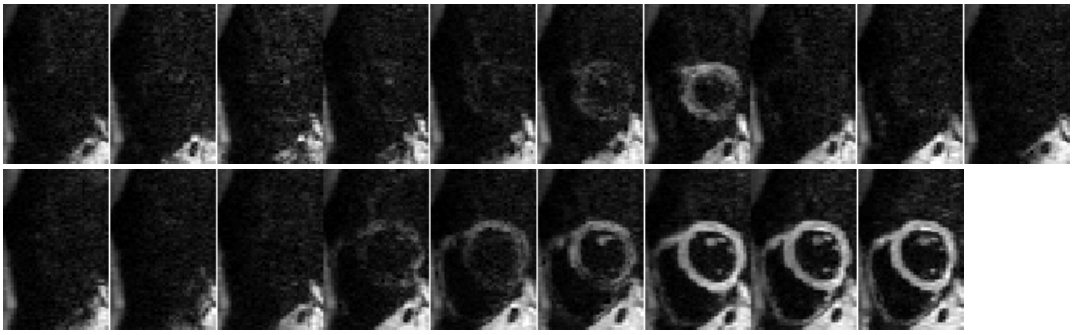

Figure 2.27. DW images acquired through the entire cardiac cycle with inceased TD 50ms. The signal loss is clear in the systole and diastole.

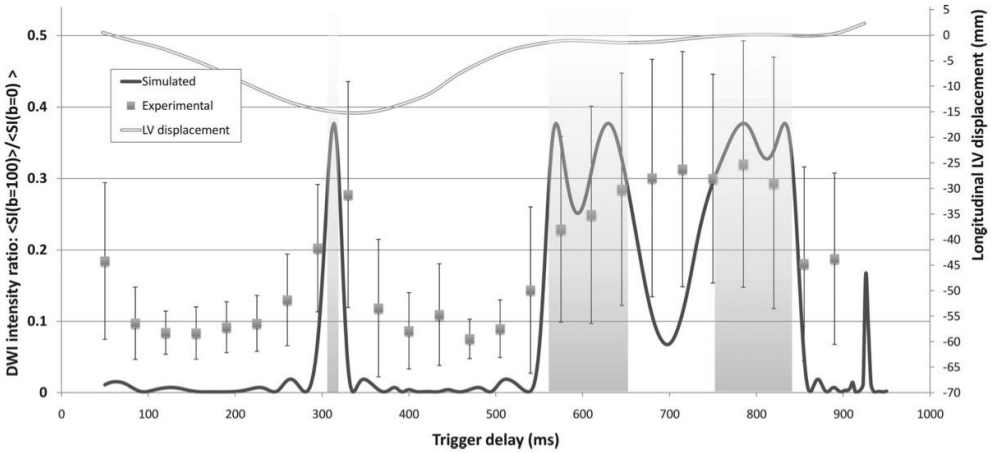

Figure 2.28. Quantification of longitudinal cardiac motion and associated DW image signal loss.

Figure 2.29 shows the DW images acquired with multiple b values. The DW image with b=0 generally good quality, b=60 with signal loss, and the higher b value (>120) the worst image quality. The higher the motion encoding gradient (MEG) in the diffusion preparation, duration, delay and amplitude, the higher the attenuation, which prevent the use of strong b value in heart diffusion imaging. (~550 being the optimum value for skeletal muscle).

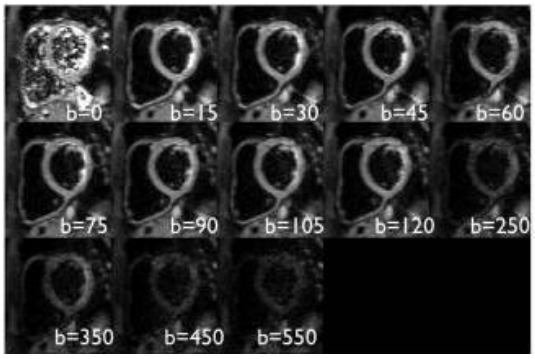

Figure 2.29. DW images acquired at end diastole with different b values.

Indeed, as we have seen, the signal decay as a function of the b-value is defined by:

$$SI = S_0 \cdot e^{-bD}, \tag{2.33}$$

where *SI* represents the signal intensity, b denotes the b-value which determines the amount of diffusion-weighting, S_0 represents the signal intensity for $b = 0$, and *D* represents the diffusion coefficient related to molecular mobility. However, this model does not take into account the attenuation caused by cardiac motion. In the presence of motion, the diffusion gradients not only encode molecular motion (diffusion) but also generate an additional signal attenuation term. This term reflects the fact that the diffusion gradients encode the displacement of the moving object and generate a phase term according to the principle used in DENSE with so-called motion encoding gradients (MEG):

$$\begin{aligned} SI &= S_0 \cdot e^{-bD} \cdot e^{-i\varphi} \\ \varphi &= \gamma \int G \cdot r dt \end{aligned}, \tag{2.34}$$

where φ represents the phase shift resulting from the displacement of proton spins, γ is the proton gyromagnetic ratio, G is the gradient pulse in a given diffusion gradient direction and r is the displacement component of the spins in the diffusion gradient direction. Unlike the diffusion attenuation term $S_0 \cdot e^{-bD}$, the attenuation, $e^{-i\varphi}$, owing to tissue motion is spatially variable, unpredictable and several orders of magnitude larger than diffusion.

Hence several strategies have been proposed on the sequence side it-self to reduce the impact of motion on the MR DW signal (Nielles-Vallespin et al. 2012; Toussaint et al. 2013). Several technical challenges need to be addressed to perform in vivo CMR. Several studies in the labo using image registration and post-processing (PCATMIP) have been performed on volunteers for DWI under free-breathing (Rapacchi et al. 2011). To date, there are less studies on in vivo DTI with free-breathing. Eventhough there are some studies using PACE (prospective acquisition correction using navigators) techniques. The navigater acqusition means long scan time and it is not comfortable for patients. Therefore, it is very important to acquire in vivo DTI data under free-breathing.

The group that has built experience in the field of in vivo cardiac DTI comes from Zurich (ETH). The images are acquired at mid-systole with b= 340 s/mm^2 by an Echo Planar imaging

(EPI) sequence. Retrospective gating was used. Their results (Figure 2.30) on volunteers showed good correlation with the literature. Their work has lead to propose 3D interpolation of cardiac fibers using multiple slice DTI acquisition (Toussaint et al. 2010; Toussaint et al. 2013). By using the shape-based DT processing methods have shown the in vivo results (Figure 2.31). They acquired the DW images in 18 diffusion encoding directions. For each volunteer, the acquision slice for DTI is limited (3 or 5 slices) and totally performed on 5 volunteers. The scan time is about 10-15 min for each slice. That means for the 3D fiber tracts reconstruction, the total acquisition time should be about 5 hours.

However, due to its low bandwidth in phase-encoding direction, EPI is vulnerable to artifacts caused by static magnetic field inhomogeneity and eddy currents. The spatially variant field inhomogeneity will cause artefacts manifested by spatial distortion and signal loss in EPI image. The diffusion gradient induced eddy current will cause directionally dependent image distortion in DWI that leads to the misalignment among the DW images.

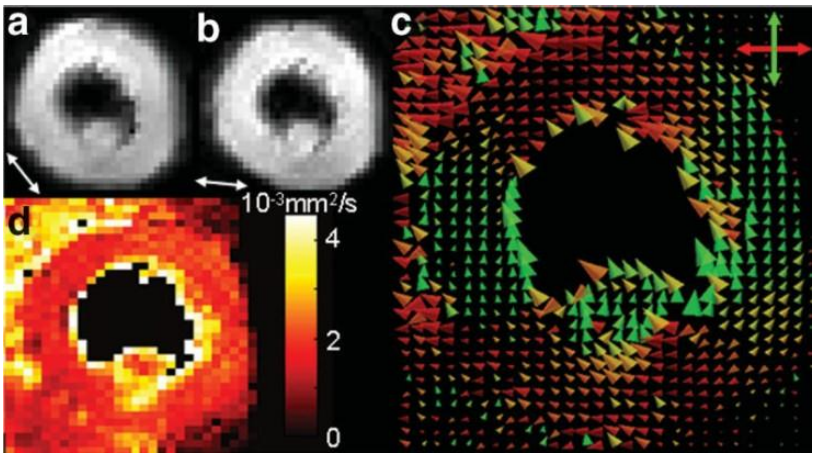

Figure 2.30. Volunteer resluts from the spin echo appoache (Gamper et al. 2007). (a) and (b): modulus images of a short-axis slice on the LV on a equatorial level. The direction of the applied gradient is indictaed by the white arrows. The (c) direction and (d) magnitude of the largest eigenvalue are shown color-coded.

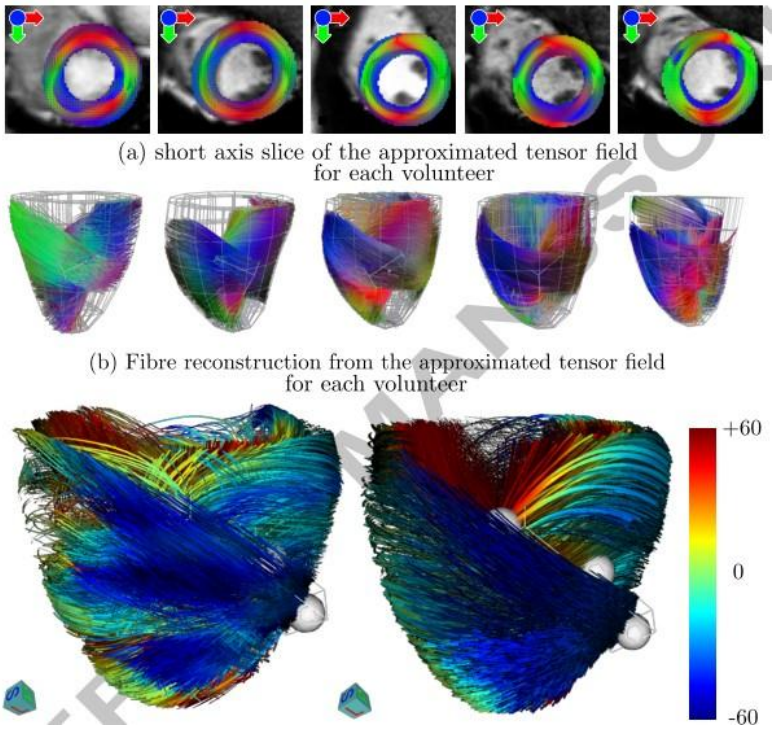

Figure 2.31. In vivo cardiac DTI results from (Toussaint et al. 2013) using 3D interpolation

Probably the most well-known in vivo cardiac work comes from the Massachusetts General Hospital (MGH). They have explored simulated-echo sequence with unipolar and bipolar diffusion encoding gradient (Dou et al. 2009). Their results have come to use of a stimulated echo (STEAM) (Figure 2.32) diffusion sequence with unipolar encoding gradients and EPI k-space readout (Tseng et al. 2000). Images are acquired at mid-systole under breath-hold.

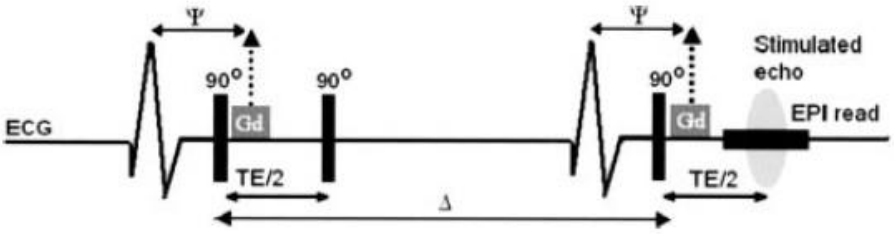

Figure 2.32. STEAM DWI sequence diagram from MGH and by their colleagues (Wu et al. 2006).

Recently, the in vivo cardiac DTI results from Royal Brompton (London, United Kingdom) have shown that the 3D fiber tracking on the volunteers with breath-hold and navigator-based free-breathing acquisitions shown in Figure 2.33. Their results show good reproducibility but have the weakness with less DTI slices and long acquisition time. The most interesting results them are that the time-resolved in vivo cardiac cardiac tensor. They successfully acquired DTI data both at systole and diastole and obtained tensor fields on the healthy volunteers (Nielles-Vallespin et al. 2012).

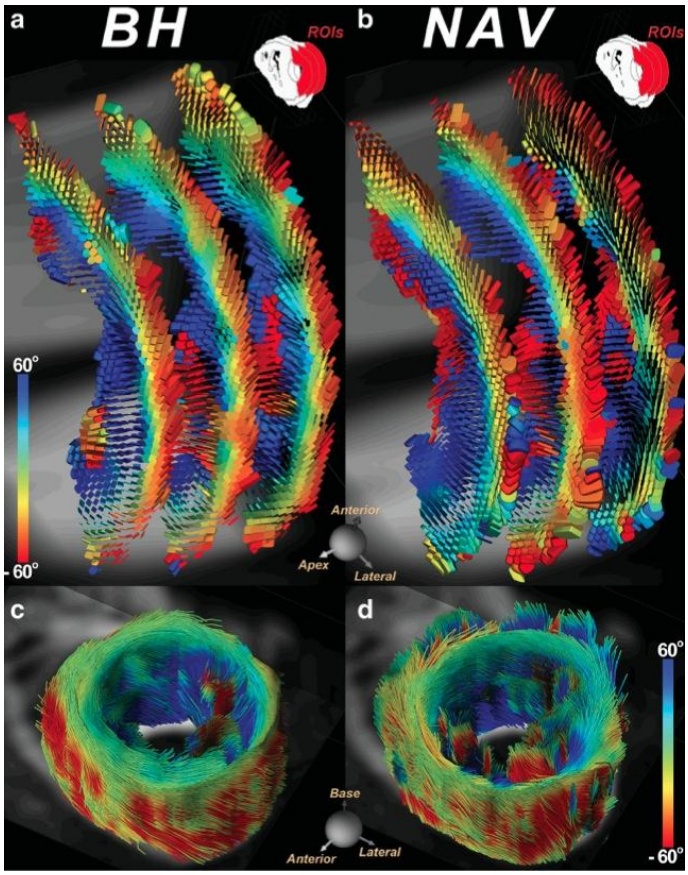

Figure 2.33. In vivo DTI results from (Nielles-Vallespin et al. 2012).

Diffusion imaging can be performed at several levels of complexity, ranging from the simple acquisition of a single DW image to the complex but robust acquisition scheme used in diffusion spectrum imaging DSI (Sosnovik et al. 2009). DTI and q-ball imaging (Descoteaux et al. 2011) can be thought of as formalisms that sample diffusion or q-space with an intermediate level of complexity. Fourier transformation of q-space produces a PDF in which the local maxima indicate the axes of fiber orientation in that voxel. The angular resolution and accuracy of DSI result in large part from the number and distribution of the samples acquired in q-space. The DSI study has been performed on the normal rat ex vivo heart (Sosnovik et al. 2009). The technique images (Figure 2.34) show the myocardium at the microstructural scale and provides information that is highly complementary to that provided by other modalities and imaging techniques. Diffusion tractography of the myocardium expands the breadth and scope of cardiovascular magnetic resonance and has the potential to become an extremely powerful tool in both the research and clinical settings.

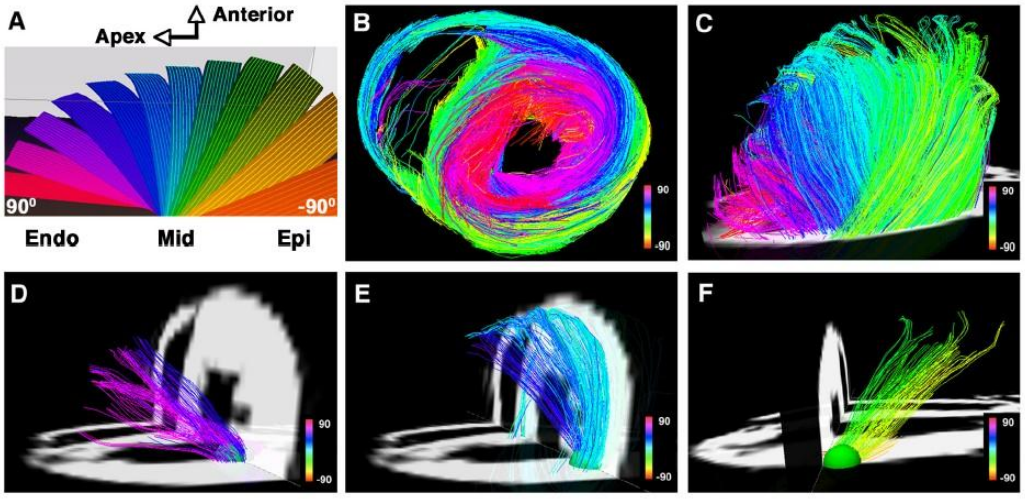

Figure 2.34. DSI tractography of a normal rat heart ex vivo showing the transmural variation in myofiber HA: Only those fibers intersecting a spherical region-of-interest are displayed in (D-F). Subendocardial fibers have a positive or right-handed helix angle and in the lateral wall course towards the antero-apex, while those in the subepicardium have a negative or left-handed helix angle and in the lateral wall course from the antero-base towards the postero-apex. Myofiber helix angle transitions smoothly from the subendocardium to subepicardium. Fibers in the mid-myocardium have a zero helix angle and are thus circumferential. (Sosnovik et al. 2009)

2.4 Conclusion

In this chapter, we mainly introduced two kinds of cardiac fiber imaging modalities: PLI and DTI, the former is for ex vivo and the latter is for in vivo imaging. For a better understanding of the main work of this thesis, the basic concepts and principles of PLI and DTI were explained.

For PLI, we showed the setup of devices for obtaining the cardiac fiber images and introduced the technique using the polarization properties of the light to detect the cardiac fiber orientation. We also pointed out the pearls and the pitfalls of this imaging technique.

As to DTI, the basic concepts involved in the magnetization process of ^{1}H, including precession, excitation, relaxation, and signal detection were illustrated. Then following the introduction of spatial encoding technique, some commonly used MRI sequences were explained. All of these make it clear how MRI works. Next, the physical process of molecular diffusion was presented, including free diffusion and the diffusion process in the cardiac fiber. Finally, combining the principles of MRI and process of diffusion, the principle of DTI was elaborated.

PART II

Contributions

Hongjiang WEI et al. IEEE trans Med Imaging 2013; 32(10): 1928-1938

Chapter 3

Assessment of cardiac motion effects on the fiber architecture of the human heart in vivo

Contents

Hongjiang WEI et al. IEEE trans Med Imaging 2013; 32(10): 1928-1938

Abstract

Using DTI for studying the human heart in vivo is a great challenge due to cardiac motion. This chapter assesses the effects of cardiac motion on the human myocardial fiber architecture. First, we need to build a real model on the signal loss caused by motion. To this end, we acquire multiple phase diffusion images and DENSE images. Totally, we acquired 20 phases through the entire cardiac cycle. Using the two kinds of information, we can estimate signal loss as a function of the cardiac longitudinal displacement. In this simulation study, the ground-truth is the ex vivo heart acquired by PLI. Knowing the fiber orientation, we can derive simulated diffusion-weighted (DW) images in multiple directions using Monte-Carlo simulation. In these simulated DW images, we can inject motion information according to the proposed motion model. By estimating the signal loss, we can add the motion into these images. Then we add the Rician noise into these images. We can obtain the simulated cardiac DW images, which allow for the construction of motion-induced datasets. Then, we calculate the diffusion parameters, such as FA, MD, and fiber angles. By comparing to the ground truth, we can quantify the effects of cardiac motion. Meanwhile the images with motion and noise are processed by PCATMIP. Diffusion parameters are calculated again and the results are compared to the ground truth, which allows us to investigate the efficiency of the motion correction method. Finally, in vivo cardiac DTI data processed by PCATMIP are compared with those obtained from one trigger delay acquisition to assess cardiac motion effects on in vivo fiber architecture. The results showed that cardiac motion induces an overestimation of FA and MD and a narrower range of fiber angles. We find that the combination of multiple shifted TD acquisitions and dedicated image post-processing can compensate for physiological motion effects and quantify motion effects on diffusion parameters.

Résumé en français

L'imagerie du tenseur de diffusion (diffusion tensor imaging-DTI) pour l'étude du cœur humain in vivo est un grand défi en raison du mouvement cardiaque. Dans ce chapitre nous étudions des effets de mouvement sur les paramètres de diffusion et sur l'évaluation de la performance de notre méthode de correction du mouvement. Tout d'abord, nous avons besoin de construire un modèle sur la perte de signal causée par le mouvement. À cette fin, nous acquérons des images de diffusion sur plusieurs phases cardiaques et des images DENSE. Au total, nous avons acquis 20 phases par cycle cardiaque entier. Nous pouvons estimer la perte de signal en fonction du déplacement longitudinal en utilisant les deux types d'informations. Dans la simulation, la vérité-terrain est le cœur ex vivo cœur acquis par PLI. Connaissant l'orientation des fibres, nous pouvons simuler des images pndérées en diffusion (diffusion weighted image—DW en angalis) multidirectionnelles par Monte-Carlo. Dans ces images DW simulées, nous pouvons injecter des informations de mouvement selon le modèle de mouvement (la courbe moyenne de mouvement). En calculant la perte de signal, nous pouvons ajouter le mouvement correspondant dans ces images. Ensuite, nous ajoutons du bruit dans ces images. Nous pouvons obtenir les images DW cardiaques simulées qui permettent de construire des bases d'images contenant des artéfacts de mouvement. Ensuite, on calcule les paramètres de diffusion, tels que FA, MD et les angles de fibres. En comparant ces paramètres avec la vérité-terrain, nous pouvons quantifier les effets de mouvement cardiaque. En même temps, les images corrompues par le mouvement et le bruit sont traitées par PCATMIP. Des paramètres de diffusion sont calculés de nouveau et les résultats sont comparés avec la vérité-terrain, ce qui nous permet d'étudier l'efficacité de la méthode de correction de mouvement. Enfin, les données in vivo cardiaques traitées par PCATMIP sont comparées avec celles obtenues à partir d'une seule acquisition afin d'évaluer les effets de mouvement cardiaque sur l'architecture de fibres in vivo. Les résultats ont montré que le mouvement cardiaque induit une surestimation de la FA, MD, et une plage étroite d'angles de fibre. Nous trouvons que la combinaison des acquisitions avec multiples TD décalés et des post-traitements d'images peut compenser les effets de mouvement physiologique et quantifier les effets de mouvement sur les paramètres de diffusion.

3.1 Introduction

DTI allows for noninvasive assessment and quantification of water molecule diffusion behavior in tissues in vivo (Sosnovik et al. 2001). In simple water molecule diffusion models, the directional dependence of diffusion is defined by diffusion tensors. Diffusion tensors can be visualized as ellipsoids with major, medium, and minor axes defined by the diffusion tensors' three eigenvectors. Diffusion tensor shape is also characterized by the diffusion tensor's three eigenvalues. The major axis, which corresponds to the largest of the three eigenvalues, reflects the direction of maximum diffusivity and thus the orientation of fiber tracts (Kingsley 2006). Cardiac DTI has been used to depict the fiber architecture of the human heart in healthy individuals (Edelman et al. 1994; Tseng et al. 2006; Nielles-Vallespin et al. 2012) and patients (Wu et al. 2006; Wu et al. 2009). FA and MD have been shown to provide quantitative information regarding the spatial coherence of cellular structures and the average intra-voxel water molecule mobility, respectively (Basser & Pierpaoli 1996). These parameters have been used in *ex vivo* cardiac DTI measurement (Helm et al. 2005) and also in vivo DTI to characterize the fiber integrity of the myocardium in patients (Wu et al. 2006). However, patient status or heart motion in *in vivo* DTI greatly influences the image quality because DTI is motion sensitive (Reese et al. 1996). Moreover, the low SNR of *in vivo* images can also cause estimation errors in these measures (Landman et al. 2008).

To date, very few studies have investigated the impact of cardiac motion on diffusion measurement and fiber architecture properties in beating human hearts. One of the main difficulties lies in the fact that cardiac motion induces large signal loss and has complex effects on diffusion tensors. Compared to computational imaging methods such as DTI, PLI appears to be the only technique that allows for physical measurement of the fiber orientation of the entire human heart in 3D with high spatial resolution ($100 \times 100 \times 500\ \mu m^3$) (Jouk et al. 2007). PLI provides the ground truth of the human cardiac fiber architecture; however, PLI can only be used in *ex vivo* hearts. On the other hand, DENSE (Aletras et al. 1999) sequences can provide high spatial resolution 3D displacement fields of the human heart *in vivo*. This has motivated us to investigate cardiac motion effects on the measurement of *in vivo* fiber architecture in a multimodal approach. More precisely, our method consists of the following: (i) using physical measurements from PLI to generate realistic DW images at different gradient diffusion directions (Wang et al. 2012) (ii) integrating motion information of the beating human heart obtained from DENSE acquisition, (iii) establishing an empirical model describing the relationship between cardiac motion and diffusion signal intensity (SI), (iv) applying this model to the simulated DW images to imitate the *in vivo* acquisition of DW images, (v) applying the PCATMIP (Pai et al. 2010) to the simulated and *in vivo* DW images to obtain motion corrected images, and (vi) computing the corresponding diffusion tensor parameters and fiber architecture properties.

3.2 Data acquisition

3.2.1 PLI data acquisition

PLI data were acquired using an *ex vivo* human heart via the procedure detailed in (Jouk et al. 2007). The heart was fixed in formaldehyde (4% neutral buffer) and was embedded in a MMA resin. It was then mounted on a microtome (Leica Microsystems, Wetzlar, Germany) stage and the plane of serial sectioning was determined such that it was parallel to the diaphragmatic face of the heart. A series of 500 µm sections was cut using a rotary microtome. Sections were then imaged using the polarized light optical bench developed in TIMC-IMAG (University of Joseph Fourier Grenoble I, France). Briefly, the section was placed on a stage and illuminated with parallel rays of polarized light. After traversing the section, this light was collected through an orientable full-wave plate and a crossed polarizer. The intensity of the resulting interfering light was measured with a charge-coupled device (CCD) camera. For a single section, a set of twelve images was collected using various orientations of the crossed polarizers and full wave plate with a specific spatial resolution (100×100 µm^2). From these images, the elevation and azimuth angles of cardiac fibers at each voxel were derived. All tissues were obtained in compliance with French legal and ethical guidelines.

3.2.2 **CMR data acquisition**

The CMR *in vivo* experiments were performed with a 1.5T clinical scanner (MAGNETOM Avanto, Siemens AG, Healthcare Sector, Erlangen, Germany) with a maximum gradient strength of 45 mT/m and maximum slew rate of 200 mT/m/ms. Six healthy volunteers were recruited for this study, including 4 males and 2 females with a mean age of 30 ± 9 years (from 25 to 50 years) and a mean heart rate (HR) of 56.5 ± 9.6 beats per minute (bpm). All subjects gave informed consent to the institutional review board-approved study protocol prior to participation.

To model the influence of cardiac motion on *in vivo* DTI, 3D displacement fields were obtained from a DENSE acquisition according to (Aletras et al. 1999). A total of 20 frames were acquired with a time resolution of 50 milliseconds covering the entire RR cycle during breath-holding conditions.

For each subject, both DENSE data and DW images were acquired in the short-axis view at the mid-ventricular level. Prior to each acquisition, standard 2-chamber, 4-chamber and short-axis cines were acquired.

For the DW image acquisitions, two different types of datasets were collected. These datasets are illustrated in Fig. 3.1(a) and Fig. 3.1(b), respectively:

1) DW images were acquired at the same time points of the cardiac cycle as in the DENSE acquisitions to study the relationship between regional signal loss and cardiac motion. The trigger delay (TD) was increased 20 times (20 TDs), in order to produce a series of multi-TD or multi-phase DW images with the same temporal resolution as the DENSE acquisitions (Fig. 3.1 (a)). The first TD (TD1) corresponds to 50 ms after the R-wave trigger. For each TD, three DW acquisitions with three orthogonal gradient directions (x, y, z) were obtained to produce b=200 s/mm² images. In total, 80 DW images, including 20 b0 images (corresponding to null diffusion gradient), were acquired under breath-holding conditions to explore the entire cardiac cycle.
2) Whole heart DTI images were then acquired with minimal signal loss, i.e., at the end of diastole (Fig. 3.1 (b)). These datasets are devoted to investigating *in vivo* cardiac DTI.

The acquisitions occurred inside an optimal time-window that corresponded to the smallest amount of cardiac motion toward the end of diastole. To achieve this in the acquired short-axis and long-axis cine sequences, we sought the time-window of smallest motion at the end of diastole. For the first time point or TD (e.g., 850 ms), we acquired one b0 image and 12 DW images corresponding to the 12 diffusion gradient directions in the optimal time-window. By shifting the TD (by 10 ms), we acquired another b0 image and 12 DW images at the next time point, which corresponded to the same 12 gradient directions. By repeating the TD shifting 10 times, we acquired a total of 10 × 13 = 130 multi-phase images for each slice. The total scan time was approximately 2 minutes for each slice under free-breathing conditions. Compared to acquisition scheme 1 (Fig. 1(a)), acquisition scheme 2 had higher temporal resolution (10 ms instead of 50 ms), and its TDs occurred in the optimal time-window situated toward the end of diastole rather than covering the entire cardiac cycle.

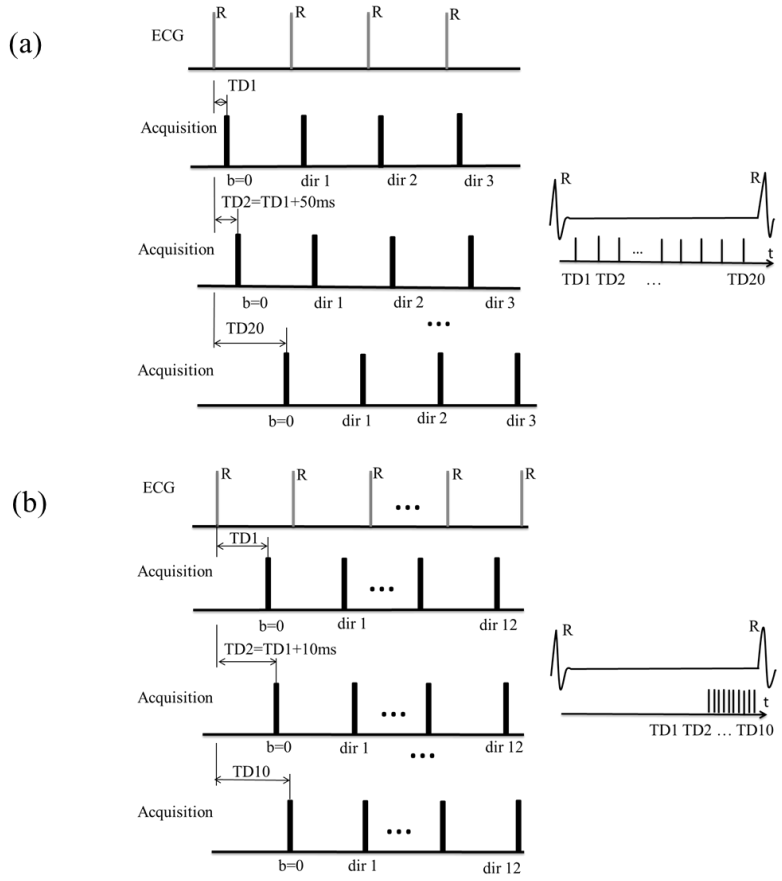

Fig. 3.1 Two DW image acquisition schemes. (a) DW images acquisition at the same time points as in the DENSE acquisitions: the 20 TDs of the DW images were determined by DENSE acquisitions. (b) DW acquisition devoted to *in vivo* DTI: the 10 DW images were acquired with TD increased by 10 ms inside a diastolic time window. "TD" in the schemes refers to Trigger Delay.

All diffusion images were acquired using a single-shot twice-refocused spin-echo EPI sequence with optimized bipolar diffusion encoding gradients, improved fat suppression using a gradient reversal technique (Park et al. 1987), and standard global phase correction. The localized first- and second-order shimming was performed with an adjustment box fitting the entire heart. The sequence parameters used for the study are listed in Table 3.1.

TABLE 3.1
SEQUENCE PARAMETERS USED IN THE PRESENT STUDY.

Cine trueFISP	FOV: 287 ×400 mm^2 Matrix: 184 ×256 Resolution: 1.56 ×1.56 ×8 mm^3 TE/TR = 1.49/35.76 ms Flip angle = 70° 29 cardiac phases	Breath-holding Acquisition time ~30s
DENSE	FOV: 168 ×448 mm^2 Matrix: 48 ×128 Resolution: 3.5 ×3.5 ×8 mm^3 TE/TR = 2/50 ms 20 cardiac phases	Breath-holding Acquisition time ~20s
DW imaging with scheme 1	FOV: 236 ×420 mm^2 Matrix: 90 ×160 Resolution: 2.63 ×2.63 ×6 mm^3 TE/TR = 51/100 ms Partial Fourier acquisition: 6/8	Breath-holding Acquisition time ~4s b-value = 200 s/mm^2
DW imaging with scheme 2	FOV: 236 ×420 mm^2 Matrix: 90 ×160 Resolution: 2.63 ×2.63 ×6 mm^3 TE/TR = 51/110 ms Partial Fourier acquisition: 6/8	Free-breathing Acquisition time ~13s b-value = 200 s/mm^2

3.3 Methods

3.3.1 Simulation of cardiac motion in DTI using DENSE sequence: Toward a motion model

From the Eq. 2.33 and 2.34, an additional attenuation is caused by motion. CMR techniques sensitive to phase variations (Fischer et al. 1995) are usually affected by longitudinal cardiac motion (through-plane motion), which leads to additional signal loss. To establish the motion model, the amplitude of the relative longitudinal displacement between two consecutive time points and the DW SI were derived from all pixels averaging in each region of interest (ROI). The LV was divided into 6 myocardial ROIs corresponding to American Heart Association (AHA) segments (Cerqueira et al. 2002), and the normalized myocardium SI was plotted as a function of the mean motion of each ROI. *In vivo* DW SI attenuation in the presence of heart

motion results from a complex process. It is not straightforward to integrate such motion in the Bloch-Torrey equations describing the precession of spins in an external magnetic field *B*, as well as the relaxation and diffusion effects in field *B*. As a first approach, we simplified the process by considering that the relationship between DW SI and cardiac motion can be modeled as an attenuation of magnetization. We then modeled the relationship between the relative longitudinal displacement amplitude (as a surrogate for cardiac motion) and SI as an exponential function regression defined by

$$y = A\exp(Bx) + \varepsilon, \tag{3.1}$$

where *y* represents the normalized SI of 20 time-course signal points inside a given sector and during one cardiac cycle, *x* represents the mean motion of each sector, *A* and *B* represent the regression coefficients, and ε represents the remaining difference between the data and the model. A moving average (MA) filter was applied to the DW SI data to identify the underlying trends hidden in the measured data. The MA filter smoothes data by replacing each data point with the data averaged in a neighborhood, according to the equation $y_s(i) = \frac{1}{2N+1}\left(y(i+N) + y(i+N-1) + ... + y(i-N)\right)$ where $y_s(i)$ is the smoothed value for the *i*th data point, *N* is the number of neighboring data points on both sides of the current data point, and 2*N*+1 defines the size of neighborhood. In the present study, we chose *N* = 2. The estimation of the regression error was evaluated by the absolute measure of fit, the root-mean-square error (*RMSE*), and a relative measure of fit, the coefficient of determination (*R-square*). They are defined by:

$$RMSE = \sqrt{\frac{1}{n}\sum_{i=1}^{n}\omega_i(y_i - \hat{y}_i)^2}, \tag{3.2}$$

where y_i is the acquired data value, $\hat{y}_i$ is the predicted value from the fit and ω_i is the weighting applied to each data point, and

$$R - square = \frac{\sum_{i=1}^{n}\omega_i(\hat{y}_i - \bar{y}_i)^2}{\sum_{i=1}^{n}\omega_i(y_i - \bar{y}_i)^2}, \tag{3.3}$$

where $\bar{y}_i$ is the mean of acquired data.

In the above definitions, usually ω_i =1. An *RMSE* value close to 0 indicates that the model has a smaller random error and that the fit will be more useful for prediction. An *R-square* value close to 1 indicates that a greater proportion of variance is accounted for by the model.

3.3.2 **Simulation of realistic cardiac DTI using PLI**

Based on fiber orientation of PLI images, an ex vivo simulated cardiac fiber structure was modeled. The diffusion behavior of water molecules in this simulated arichitecture was simulated by means of Monte-Carlo method (Wang et al. 2012). In a free medium, during a

given time interval, molecular displacement can be expressed by Einstein diffusion law (Einstein 1956), which is well described by the diffusion coefficient of water molecules in this medium. Thus, in our simulation, the distance s during one random walking time interval τ is given by:

$$s = \sqrt{2mD\tau} \tag{3.4}$$

where D is the free diffusion coefficient of water molecules in the cardiac muscle at 37ºC, and m is the diffusion dimension.

In the biological tissues, the walking displacement distribution of water molecules is determined by the structure of tissues. In our simulation, this distribution is split into two items. One is the distribution of diffusion distances $P(s)$ during one walk step, which is simulated by a Monte-Carlo method. The other is about the diffusion directions that conform to uniform distribution in our case.

Since the molecule position randomly varies with time, at the end of each walking step, the displacement $\overrightarrow{r_i^j}$ of each molecule i for the j^{th} walking step is different, which is expressed by

$$\overrightarrow{r_i^j} = sP(s) \tag{3.5}$$

In order to measure this displacement, a pair of magnetic field gradient pulses in the different directions are simulated, whose duration is δ, diffusion time is Δ and gradient strength vector is $\vec{G}$. These parameters determine the simulated $\vec{q}$ value and $\vec{b}$ factor for calculating diffusion signal:

$$\vec{q} = \frac{\gamma}{2\pi}\vec{G}\delta \tag{3.6}$$

$$\vec{b} = 4\pi^2\vec{q}^2(\Delta - \delta/3) \tag{3.7}$$

where γ is the gyromagnetic ratio of ^{1}H with a constant value of 42.5657 MHz/T. According to the basic theory of dMRI, the phase shift induced by the displacement of molecule i during the j^{th} walking step is:

$$\phi_i^j = 2\pi\vec{q}\cdot\overrightarrow{r_i^j} \tag{3.8}$$

The total number of random walks k is:

$$k = \Delta/\tau \tag{3.9}$$

Thus at the end of the diffusion gradient pulse, the phase shift caused by one molecule is:

$$\phi_i = \sum_{j=1}^{k}\phi_i^j = 2\pi\sum_{j=1}^{k}\vec{q}\cdot\overrightarrow{r_i^j} \tag{3.10}$$

Accordingly, the diffusion signal caused by the diffusion of n molecules is numerically approximated by:

$$E = \frac{1}{n}\sqrt{(\sum_{i=1}^{n}\cos(\phi_i))^2 + (\sum_{i=1}^{n}\sin(\phi_i))^2} \tag{3.11}$$

The key point of this simulation is to find accurately the collision point between the molecules and the complex tissue structures at different diffusion moments. It determines whether the simulated diffusion images are capable of interpreting the microstructures for a given model. The flow diagram in Fig. 3.2 illustrates the simulation process.

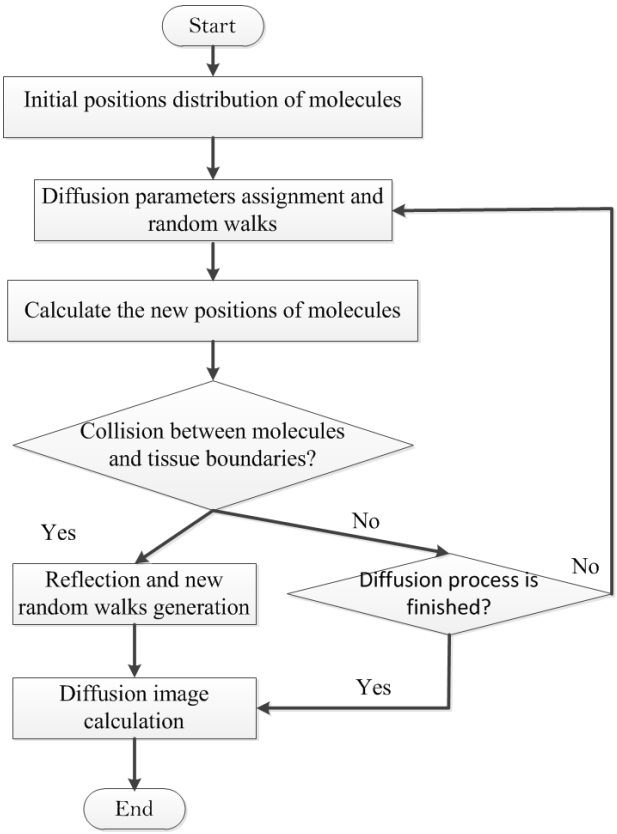

Fig. 3.2 Flow diagram of the proposed simulation.

In order to choose an appropriate distribution $P(s)$ of random walking step lengths, we use situations with Gaussian distributions (Farnell & Gibson 2004), which are often used in diffusion simulations. We assume that water molecules diffuse in two infinite parallel plates separated by a distance of $2a$. If the diffusion gradient is applied along the direction normal to the plates, the thus resulting diffusion corresponds to the restricted one. However, if the gradient is added in the direction parallel to the plates, it then concerns free diffusion of the water molecules in this direction. For the restricted diffusion and the free diffusion, the corresponding analytical diffusion signals are given respectively in the works of (Price 1997; Price & Price 1998):

$$E_{\text{retrict}} = \sin^2(\pi qa)/(\pi qa)^2 \tag{3.12}$$

$$E_{\text{free}} = \exp(-bD_0) \tag{3.13}$$

Using Monte-Carlo method, we simulate the diffusion of water molecules between two plates and calculate the diffusion signal for the restricted diffusion. In all the simulations, the number of molecules is set to 2×10^8 in order to obtain the results with high accuracy. At the beginning, the molecules are uniformly distributed in the space. Then, they walk randomly with Gaussian distribution of walk step lengths, but with the same distribution of directions. After a given time, according to Eq. (3.11) the diffusion signals in the directions both normal and parallel to the plate are calculated. All simulations were performed on a PC machine cluster and the computation time was about 16 hours.

Once the simulated static DW images were gernerted, we can get the following simulated images with added motion and noise. Fig. 3.3 presents a flowchart describing simulated DW data generation, post-processing and analysis. First, the diffusion behavior of water molecules in the cardiac fiber structure was simulated based on a series of cardiac PLI data using the Monte Carlo method. In the simulation, 6 diffusion gradient directions ([1 0 0; 0 1 0; 0 0 1; 0.707 0.707 0; 0 0.707 0.707; 0.707 0 0.707]) were applied and the diffusion coefficient for the water molecules in the cardiac tissue was set to 1×10^{-3} mm^2/s in all the directions. Six DW images were then generated, from which the reference tensor field as well as FA, MD, and fiber angles were calculated. Second, Rician noise was added to the simulated DW images to imitate real noise situations before motion was incorporated (Skare et al. 2000). The added Rician noise had a standard deviation of σ_R =17 with respect to the SI of 102, which corresponded to a SNR of 6 (which is the same as that used in previously published work) (Pai et al. 2010). In parallel, the average motion was calculated from the 20 displacement fields obtained using a DENSE sequence for all six healthy volunteers. The raw data obtained by the DENSE acquisition were processed using IDL (Research systems, Inc., Boulder, CO, USA); phase map differences were constructed using the reference scan and the encoded images (Aletras et al. 1999). Following manual myocardial border segmentation, the maps were phase-unwrapped and scaled to the position-encoding gradient strength, yielding separate displacement maps for the x, y, and z directions. The corresponding signal loss was calculated using the motion model described above (Eq. 2.34) and was added to the noise-simulated DW images to yield multi-directional DW images mimicking noisy *in vivo* cardiac DW images contaminated with realistic intrascan cardiac motion. Because the DENSE encoded data had a temporal resolution of 50 ms, we used linear interpolation to interpolate the cardiac diastolic motion to achieve a temporal resolution of 10 ms. Ten DW images at 10 TDs in diastole with intensity fluctuations induced by cardiac motion were generated for each diffusion gradient direction, which resulted in a total of 60 multi-directional and multi-TD DW images and 6 reference images with a null diffusion gradient.

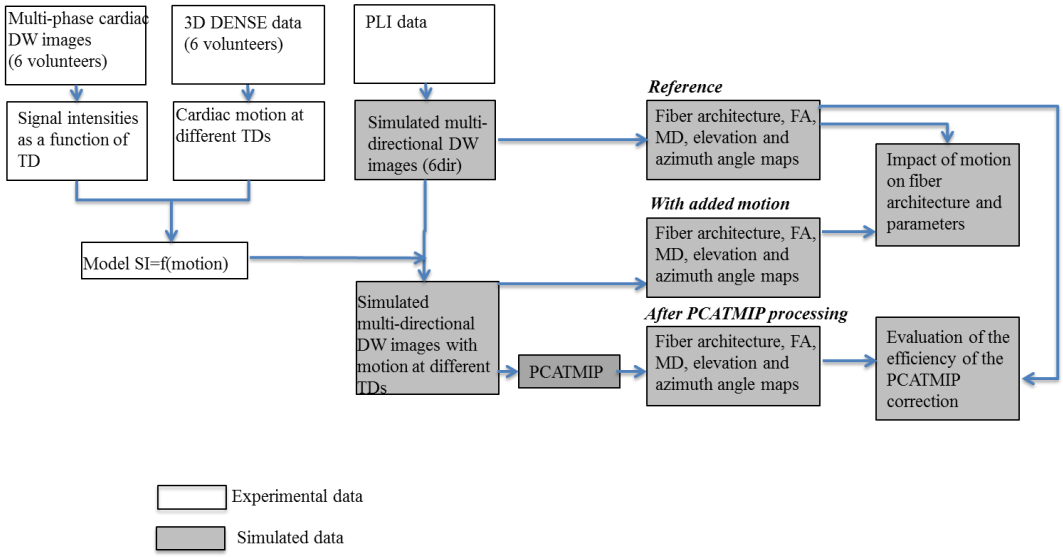

Fig. 3.3 Flowchart of simulated DW data generation and post-processing. Blocks with gray background represent simulated data and blocks with white background represent experimental data. "TD" represents Trigger Delay.

3.3.3 **Post-processing and analysis**

After the acquisitions using scheme 2 were obtained (Fig. 3.1(b)), a set of DTI images was formed using b0 images and DW images corresponding to the combination of the 12 gradient directions and 10 equi-spaced time points (10 ms shift acquisition over the end of diastole). Because these DTI images were acquired under free-breathing conditions, we registered them in order to compensate for motion and correctly calculate the subsequent diffusion tensor parameters. To this end, a non-rigid registration algorithm (Guetter et al. 2011) was applied, not only to the different TD DW images corresponding to a given diffusion direction but also to the DW images at all of the diffusion directions. For a given gradient direction, we then obtained a temporal sequence of registered images corresponding to different shifted TDs or time points. Our goal was to then find, for each given pixel, an optimal time point at which motion is minimal. To this end, we applied the PCATMIP technique (Pai et al. 2010) to the temporal sequence of DW images, which was used as follow. Given a set of 2D raw images from the same slice location, $I(x, y, k)$, where $k=1, 2,...N$ is the number of repetitions of the acquisitions, they were divided into some subregions, $I_{sub}(b, c, k)$ (with $0<b\leq 15$ and $0<c\leq 15$ in the present study). The following symmetrical matrix is calculated over each of the subregions

$$M(k,l) = \iint I^*_{sub}(b,c,k) I_{sub}(b,c,l) dbdc \tag{3.14}$$

Diagonalizing the symmetrical matrix yields the eigenvalues ε_j and eigenvectors $V_j(k)$ such that

$$\sum_k V_i^*(k) V_j(k) = \delta_{ij} \tag{3.15}$$

where δ_{ij} is the Kronecker delta. The principal components $P_j(a, b)$ were calculated over the subregion using the eigenvectors

$$P_j(a,b) = \sum_k I(b,c,k)V_j^*(k) \tag{3.16}$$

such that

$$\iint P_i(b,c)P_j(b,c)dbdc = \delta_{ij}\varepsilon_i \tag{3.17}$$

Using a number of principal components (determined by threshold E_t above noise), the new image was calculated over the subregion as

$$I'(b,c,k) = \sum_m P_m(b,c)V_m(k) \tag{3.18}$$

For each pixel, one of the 10 repetitions that provides the highest intensity value can be identified, leading to

$$I_{PCATMIP}(x,y) = \underset{k=1}{\overset{N}{MAX}}(I'(x,y,k)) \tag{3.19}$$

By assigning the highest intensity to that pixel in a reconstituted DW image and repeating this procedure for every pixel, we obtained the final image which is a DW image of minimal signal loss due to motion.

The two key parameters in the PCA process are the size of the sliding boxcar and the eigenvalue threshold E_t. The size of the boxcar needs to be large enough to distinguish coordinated physiological effects from random noise and small enough to capture the local pattern of motion-induced fluctuation. Thus, the box size should be small enough that no more than 2 components are included; thus, 2 PCs are needed to describe the intensity fluctuations in the box and can capture local pattern of motion-induced fluctuation, but large enough to distinguish coordinated physiological effects from random noise. The eigenvalue threshold E_t should be set high enough to reject the PCs corresponding to pixel-wise random noise and low enough to include the PCs from global intensity fluctuations caused by motion. Both parameters were determined by numerical simulations based on the SNR level of experimentally acquired DW images, more details can be found in (Pai et al. 2010).

Calculating the final image for each gradient direction generated 12 DW images, which allowed us to obtain a whole heart DTI dataset with the derived diffusion tensor parameters (FA, MD, elevation angle, azimuth angle, and 3D tracts).

To illustrate how an optimal time point inside the optimal window can be found in a (registered) DW image sequence obtained using multiple shifted TD acquisitions, Fig. 3.4 presents two curves showing the variation of motion amplitude (measured from DENSE sequence) at a pixel in the lateral wall and the variation of this voxel SI as a function of time points for one volunteer, respectively. These curves clearly show that the optimal time point for this case occurred at 900 ms; at this time point, motion is at a minimum and SI is at a

maximum, which implies that motion-reduced DW SI can be accessed using multiple shifted TD acquisitions.

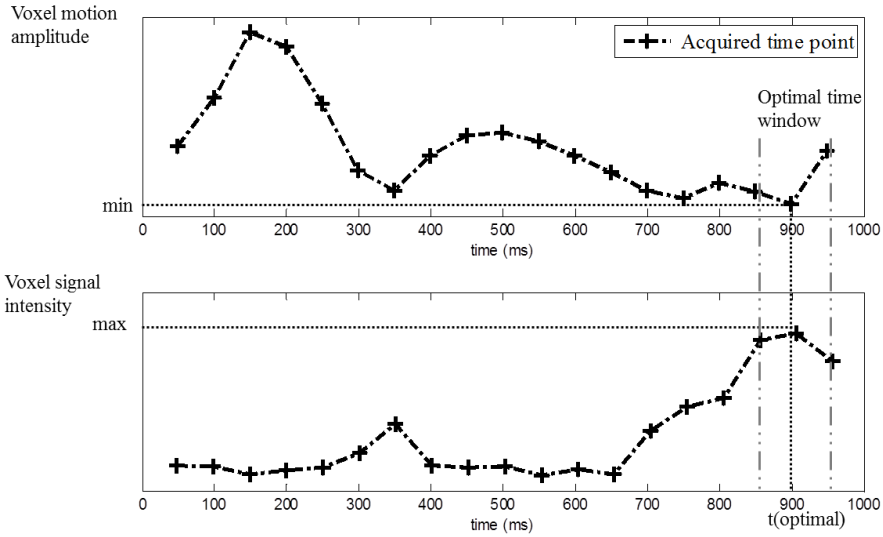

Fig. 3.4 Variations of voxel motion amplitude and signal intensity as a function of time points for one pixel in the lateral wall. Signal loss is relatively low at a few phases of the cardiac cycle and reaches a minimum inside the optimal time-window, which occurred at the time point 900 ms for this case.

***Simulated DTI data**:* Image post-processing was performed using MATLAB (R2010b, the Mathworks, Inc., Natick, MA, USA). The PCATMIP technique was applied to the temporal sequence of DW images corresponding to the same diffusion gradient direction but different TDs. The SI was measured in the LV after manual segmentation of the myocardium in b = 0. The SI values of the entire myocardium resulting from PCATMIP processing were used to estimate the motion information according to the proposed cardiac motion model. We compared the motion information obtained from the PCATMIP-processed DW images with those originally included in the PLI simulated DW data.

For quantitative analysis, the trace diffusion-weighted image (T-DWI) was defined as the geometrical mean of the DW image intensity over all the directions (N = 6):

$$T-DWI=\sqrt[N]{DWI_1\cdot DWI_2\cdot ...DWI_N} \tag{3.20}$$

The SNR of the T-DWI images was then defined to assess the quality of the acquired DW images

$$SNR=\frac{\langle I\rangle_{LV}}{Noise} \tag{3.21}$$

where $\langle I\rangle_{LV}$ denotes the pixel intensity mean over the LV wall and "Noise" was measured as the standard deviation (SD) of pixel intensities over the LV wall.

However, SNR alone is not sufficient to completely assess the quality of the acquired DTI data. Indeed, DTI data are fundamentally different from commonly used scalar data (gray-

level images) or vector-valued data; it is essentially diffusion tensor data, which implies that DTI data should be evaluated not only at the level of the DW image (although their quality is primarily the most important) but also at the level of diffusion tensor-derived parameters such as FA, MD, and fiber angles. These parameters constitute the main practical indices to evaluate myocardial integrity. FA and MD are defined in terms of the eigenvalues λ_1, λ_2, and λ_3 of the diffusion tensor. FA represents the degree of deviation of a diffusion ellipsoid from a sphere and was quantified as the SD of the eigenvalues of the diffusion tensor normalized by the "magnitude" of the 3 eigenvalues of the diffusion tensor. FA varies between 0 (perfectly isotropic diffusion) and 1 (the hypothetical case of an infinite cylinder).

To compare the data with the ground truth of the fiber architecture provided by PLI (Jouk et al. 2007), we calculated two indices: elevation angle and azimuth angle. The elevation angle corresponds to the angle between the fiber and the short-axis plane, while the azimuth angle represents the angle between the projection of the fiber in the short-axis plane and the +y axis.

***In vivo DTI data**:* The DW images acquired under free-breathing conditions were first registered and then processed using the PCATMIP method as described previously in detail. These DW images were then used to calculate the tensor fields. To improve spatial resolution, the diffusion tensors were interpolated in the plane by a factor of 2 using the Log-Euclidean method, which avoids swelling effects (Arsigny et al. 2006).

Subsequently, FA, MD, elevation angle, and azimuth angle maps were calculated from the tensor fields, and they were compared to the results obtained from one single trigger delay (1TD). Elevation angle was calculated in the regions of the LV wall at 5 transmural locations (endocardium, mid-endocardium, mid-wall, mid-epicardium, and epicardium layers). The partition of the myocardium into these transmural layers was achieved by first manually segmenting the LV, calculating a distance from the endocardium to the epicardium, and finally dividing the distance into five segments equally. The pixels belonging to the same layer were automatically grouped into the same class on which the elevation angle was calculated. Finally, the 3D fiber architecture of the human heart from multi-slice data was obtained using the conventional streamline algorithm.

3.4 Results

3.4.1 Influence of motion on diffusion parameters in simulation

Fig. 3.5 plots the relationship between cardiac motion and signal loss (normalized myocardial DW SI) for each of the 6 datasets corresponding to the 6 volunteers (Fig. 3.5 (a) to (f)), and the cardiac motion model (Fig. 3.5 (g), red curve), which was obtained by fitting SI values (blue points) as a function of cardiac motion. The experimental data were acquired and analyzed based on AHA ROI segmentation. Globally, more motions increases SI attenuation. Fig. 3.5 (a)-(f) shows that the 6 datasets exhibit rather similar behavior. However, the experimental data do not exhibit a simple monotonous relationship between the SI values and the cardiac motion, as illustrated by the discrepancy between the blue points and red curve in Fig. 3.5 (g). The fitting parameters of this model are *RMSE* = 0.026 and *R-square* = 0.9855, which were obtained from the regression estimation. This model provided a mean

value to add signal loss in simulated DW images to imitate the *in vivo* DW image acquisition of the beating human heart.

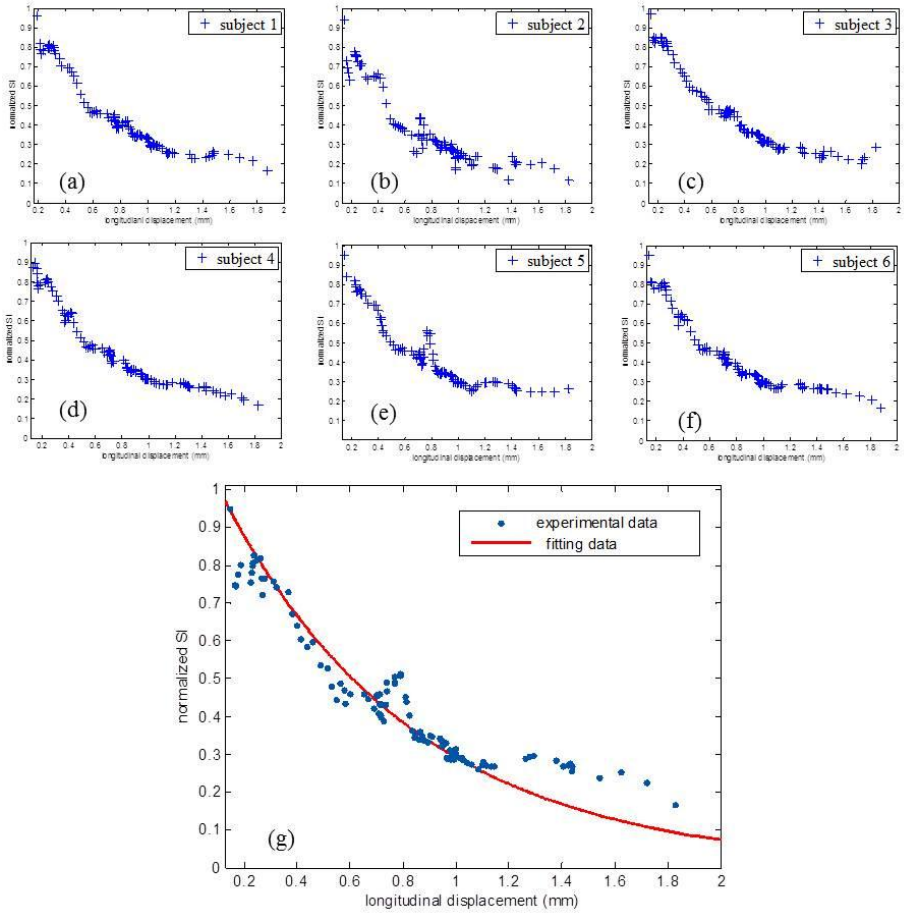

Fig. 3.5 Normalized myocardial DW SI as a function of cardiac motion for the 6 volunteers corresponding to (a) through (f) and the cardiac motion model over the 6 volunteers (g). The blue points in (g) represent experimental data: for each blue point, the x value indicates the relative longitudinal displacement amplitude and the y value indicates the measured SI derived from all pixels averaged inside each of the 6 AHA ROIs. The red curve in (g) represents the fitted data.

The impact of cardiac motion on T-DWI simulated by volunteer's physiological motion and on fiber architecture properties is shown in Fig. 3.6. Signal dropout due to motion is visible in the LV. Table 3.2 provides quantitative analysis of the impact of cardiac motion on normalized SI, SNR, and fiber architecture properties corresponding to Fig. 3.6. The DW images corrected by the PCATMIP method offered an overall increased SI (this is consistent with the hypothesis that PCATMIP removes inherent signal loss due to motion) and therefore resulted in a subsequent higher SNR (5.3) compared to the Ref + noise (4.9) and the Ref + noise + motion (3.7). This illustrates that the PCATMIP can effectively recover signal loss due to cardiac motion. The signal loss due to noise resulted in increases in FA (0.82 ± 0.07) and MD (0.95 ± 0.87 $\times 10^{-3}$ mm^2/s) compared to those obtained from the original DW images (0.56 and 0.78 $\times 10^{-3}$ mm^2/s for FA and MD, respectively). With the added motion, signal loss

is more pronounced. After processing by the PCATMIP, we observed lower FA values with respect to the Ref + noise (-28%), but higher FA values with respect to the Ref (+5%). We also observed smaller MD values with respect to the Ref + noise + motion (-54%); however, the MD values are higher than those in the Ref+ noise and the Ref (+19% and +44%, respectively). The results showed that both FA and MD were overestimated with increased motion and that motion-induced signal loss could be minimized after using PCATMIP.

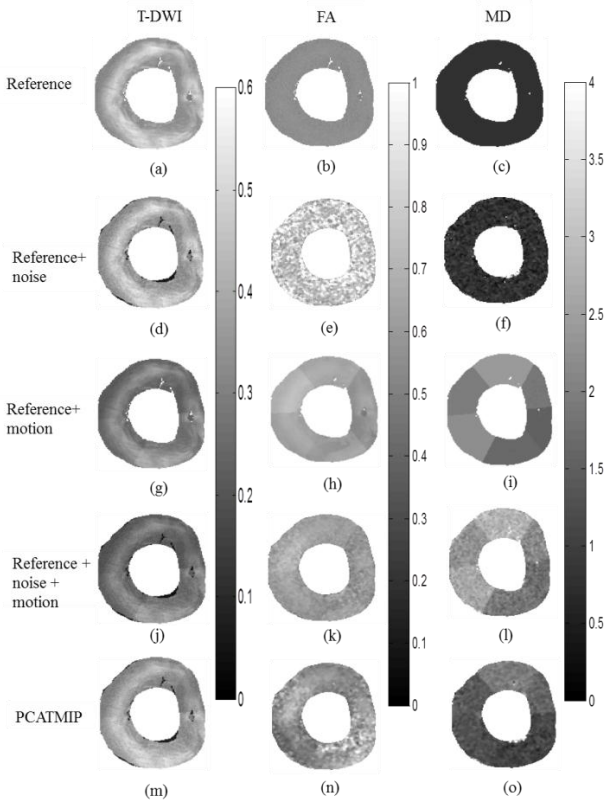

Fig. 3.6 Impact of cardiac motion on T-DWI (left column) and fiber architecture properties (middle and right columns) using simulated data. (a)-(c) With reference noise-free data. (d)-(f) With reference + noise data. (g)-(i) With reference + motion data. (j)-(l) With reference + noise + motion data. (m)-(o) PCATMIP results.

TABLE 3.2

QUANTITATIVE ANALYSIS OF THE IMPACTS OF CARDIAC MOTION ON MORMALIZED SI, SNR, AND FIBER ARCHITECTURE PROPERTIES USING SIMULATED DATA. MD VALUES ARE IN UNITS OF 10^{-3} mm^2/s.

	SI	SNR	FA ± SD	MD ± SD
Ref	0.399	6.8	0.56	0.78
Ref + noise	0.389	4.9	0.82 ± 0.07	0.95 ± 0.87
Ref + motion	0.295	3.9	0.61 ± 0.05	1.99 ± 0.30
Ref + noise + motion	0.263	3.7	0.62 ± 0.10	2.45 ± 1.21
PCATMIP	0.369	5.3	0.59 ± 0.02	1.13 ± 0.49

Fig. 3.7 shows the elevation and azimuth angle maps calculated from the primary eigenvectors of the diffusion tensor fields. Fig. 3.7 (a) and (b) represent the original maps without adding noise and motion. In Fig. 3.7 (a), the elevation angle varies from $57^{\circ} \pm 9^{\circ}$ on the endocardium to $25^{\circ} \pm 10^{\circ}$ on the mid-wall, and back to $51^{\circ} \pm 13^{\circ}$ on the epicardium of the LV, which reflects fiber rotation. In Fig. 3.7 (b), we can observe continuous circular variation of the azimuth angles inside the LV wall. The azimuth angle varies with the curvature of the LV and rotates with a smooth progression from one color to the other while turning around the LV. For example, there are red fibers at the junction between the LV and right ventricle of the heart with a 0° azimuth angle, and blue fibers in the inter-ventricular septum and lateral wall of the ventricles with a 90° azimuth angle. Variation in the azimuth angle reflects the spiral-shaped muscle structure of the heart. The regular variation pattern of elevation and azimuth angles is removed after adding the Rician noise and cardiac motion in Fig. 3.7 (g) and (h). Signal loss due to motion and noise therefore greatly influence the angle maps. After using the PCATMIP method, regular azimuth angle (Fig. 3.7 (j)) variation patterns were nearly completely recovered despite a relatively higher noise level. However, the elevation angle (Fig. 3.7 (i)) range was narrower ($41^{\circ} \pm 13^{\circ}$ on the endocardium, $15^{\circ} \pm 11^{\circ}$ on the mid-wall, and $35^{\circ} \pm 12^{\circ}$ on the epicardium) than in the reference (Fig. 3.7 (a)).

Fig. 3.7 presents the iber taractographis in this simulation study. Fig.3.7(a) shows the fiber tracts obtained from simulated DW images. We can clearly see the fiber orientation from the top of the heart. Fig.3.7(c) shows the cardiac fiber with added motion and noise. While Fig. 3.8(b) presents the fiber tracts processed by PCATMIP. 3D cardiac fiber architecture is recoverd and the advantage of PCATMIP for coping with signal loss is obvious.

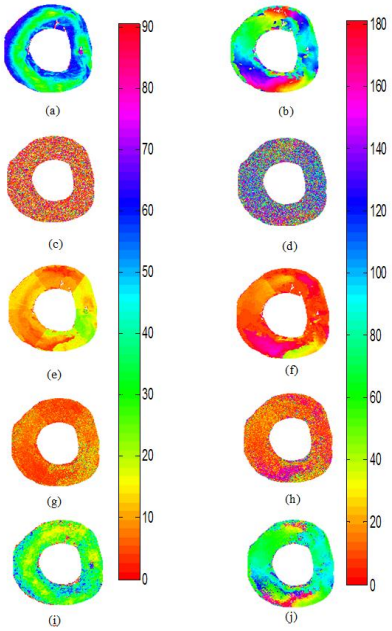

Fig. 3.7 Elevation angle maps (left column) and azimuth angle maps (right column). (a) and (b) Original angle maps from simulated DW data. (c) and (d) Angle maps after adding noise. (e) and (f) Angle maps after adding cardiac motion. (g) and (h) Angle maps after adding noise and cardiac motion. (i) and (j) corrected angle maps after using PCATMIP processing.

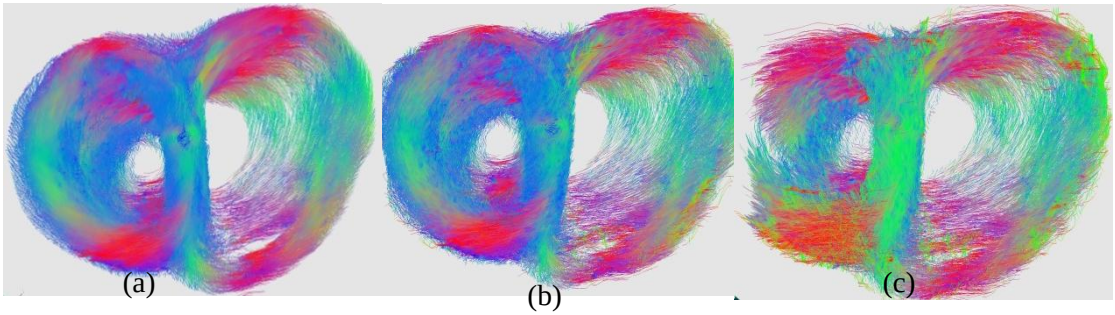

Fig. 3.8. Fiber architectures of the simulation study. (a) Fiber tracts calculated from the simulated DW images. (b) Fiber tracts after processed by PCATMIP. (c) Fiber tracts with added motion and noise.

3.4.2 *In vivo* DTI results

Fig. 3.9 shows an example of in vivo cardiac DW images of a volunteer. Fig. 3.9(a) presents DW images of 10 TD acquisitions of one diffusion gradient direction. The signal loss throughout the myocardium is visible because the cardiac motion was spatially and temporally heterogeneously distributed due to free-breathing during acquisition. Fig. 3.9(b) shows the processed DW image after applying the PCATMIP method to the 10 TD DW images. Fig. 3.9(c) shows the DW images recovered from the raw images using the PCATMIP method in 12 directions, which presents highly reduced motion artefacts and reduced intrascan signal loss.

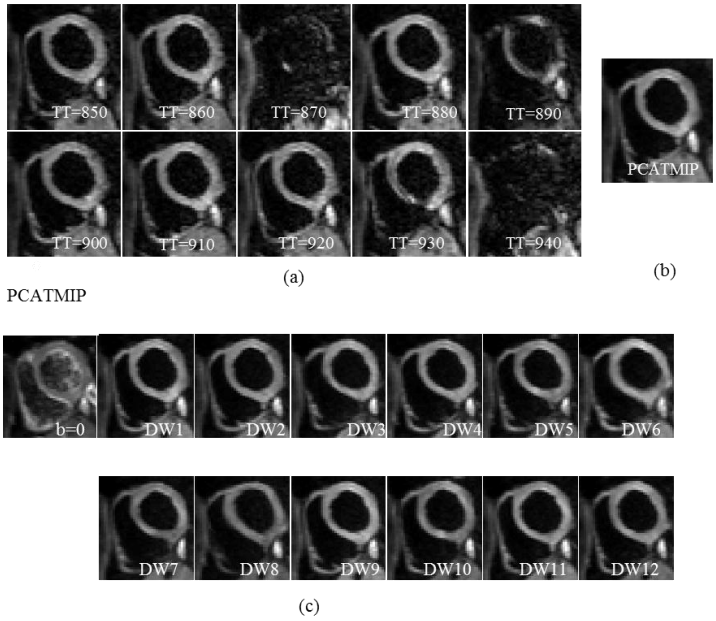

Fig. 3.9 (a) Free-breathing short-axis DW images from 10 repetitions acquired at different time points for one direction during diastole on a volunteer. Visible spatial SI fluctuation resulting from spatially variable intrascan motion is visible. (b) Processed DW images for one direction using the PCATMIP method. (c) DW images corresponding to 12 diffusion gradient directions as well as b0 images were reconstituted using the PCATMIP method.

The FA, MD, elevation angle, and azimuth angle maps are illustrated in Fig. 3.10. The maps revealed that the mean FA value for 1TD (without PCATMIP) (0.60) is higher than that obtained using PCATMIP (0.42). The MD maps revealed significant differences between before and after processing with PCATMIP. PCATMIP yielded significantly lower MD than with 1TD (-73%). It also yielded smaller SD (0.28 $\times 10^{-3}$ mm^2/s) than without PCATMIP (0.37 $\times 10^{-3}$ mm^2/s). There were also significant differences between 1TD and PCATMIP in the angle maps. With 1TD, heterogeneous elevation and azimuth maps were yielded due to signal loss throughout the myocardium, while PCATMIP generated smooth angle maps. For PCATMIP, the elevation angle varied globally from $-43^{\circ} \pm 16^{\circ}$ on the epicardium to $10^{\circ} \pm 9^{\circ}$ on the mid-wall and to $32^{\circ} \pm 19^{\circ}$ on the endocardium, which reflects the fiber rotation of the LV.

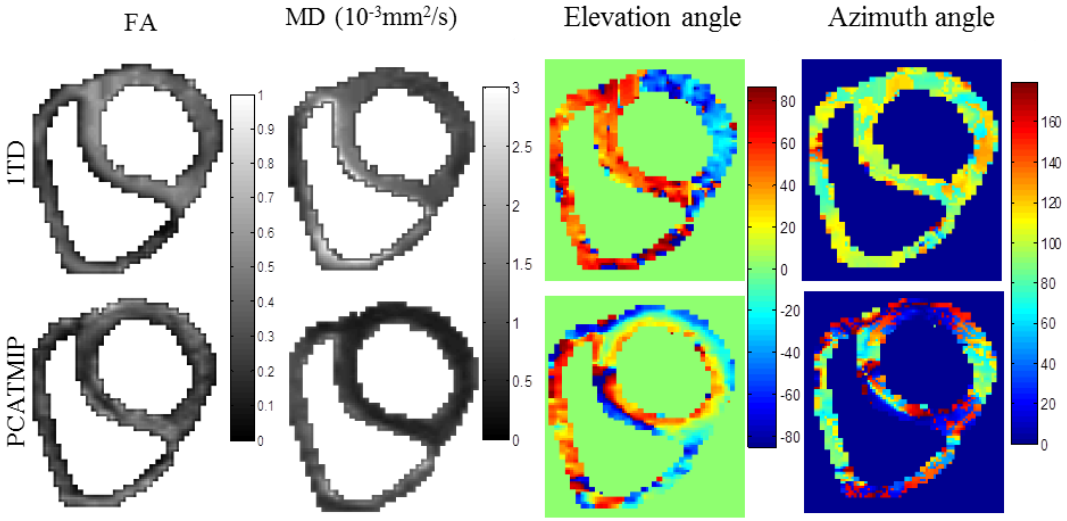

Fig. 3.10 FA, MD, elevation and azimuth maps calculated from tensor fields for a short-axis slice in a healthy volunteer.

Table 3.3 summarizes the results obtained after applying PCATMIP to the *in vivo* cardiac DTI datasets of all of the volunteers. For each volunteer, with or without PCATMIP, the FA and MD variation share the same trend: PCATMIP yielded lower FA and MD values than 1TD. The mean FA value over all of the volunteers that was obtained using PCATMIP (0.43 ± 0.05) was smaller than that obtained using 1TD (0.56 ± 0.05). At the same time, the mean MD value over all of the volunteers with PCATMIP (0.75 ± 0.12 $\times 10^{-3}$ mm^2/s) was smaller than that obtained using 1TD (1.37 ± 0.16 $\times 10^{-3}$ mm^2/s).

TABLE 3.3
MEAN ± SD FA AND MD VALUES IN THE LV OF ALL VOLUNTEERS. THE RESULTS DEMONSTRATED THAT THE PCATMIP CORRECTION YIELDED SYSEMATICALLY LOWER VALUES AND MUCH LOWER VARIATION THAN 1TD ACQUISITIONS.

Subject	FA ± SD		MD ± SD ($\times 10^{-3}$ mm^2/s)	
	1TD	PCATMIP	1TD	PCATMIP
1	0.59± 0.08	0.51± 0.02	1.23± 0.19	0.77± 0.09
2	0.56± 0.02	0.48± 0.02	1.52± 0.08	0.88± 0.04
3	0.60± 0.11	0.42± 0.02	1.57± 0.14	0.58± 0.08
4	0.60± 0.13	0.39± 0.03	1.41± 0.16	0.74± 0.07
5	0.57± 0.09	0.42± 0.02	1.25± 0.08	0.88± 0.10
6	0.46± 0.04	0.39± 0.01	1.23± 0.08	0.64± 0.03
Mean ± SD	0.56± 0.05	0.43± 0.05	1.37± 0.16	0.75± 0.12

Fig. 3.11 shows the mean ± SD of the elevation angle values over all volunteers in the five cardiac layers with and without (1TD) PCATMIP. The elevation angle values for all of the volunteers vary from $32^\circ \pm 9^\circ$ in the endocardium layer, through $24^\circ \pm 5^\circ$ in the mid-endocardium layer and $13^\circ \pm 5^\circ$ in the mid-wall, and $-7^\circ \pm 7^\circ$ in the mid-epicardium layer to $-27^\circ \pm 7^\circ$ in the epicardium layer.

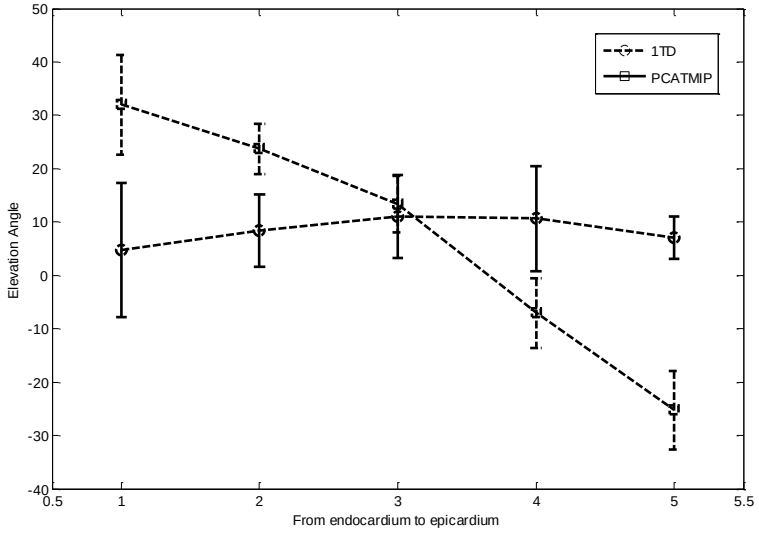

Fig. 3.11. Elevation angle values obtained without (1TD, dotted line) and with the PCATMIP (solid line) method from the endocardium to epicardium of the LV. The x value (from 1 to 5) in the plot represents five different transmural locations (endocardium, mid-endocardium, mid-wall, mid-epicardium and epicardium layers, respectively). The error bars represent the standard deviations in each dataset.

Fig 3.11 shows 3D fiber tracts obtained from PCATMIP post-processing on 5 volunteers. The top row shows the fibers viewed from the lateral wall of the heart. For better depict the

fiber orientation, we apply a shutter located at the lateral wall. The fiber orienataion from the endocardiuam to pericardium is clearly seen from the shutters

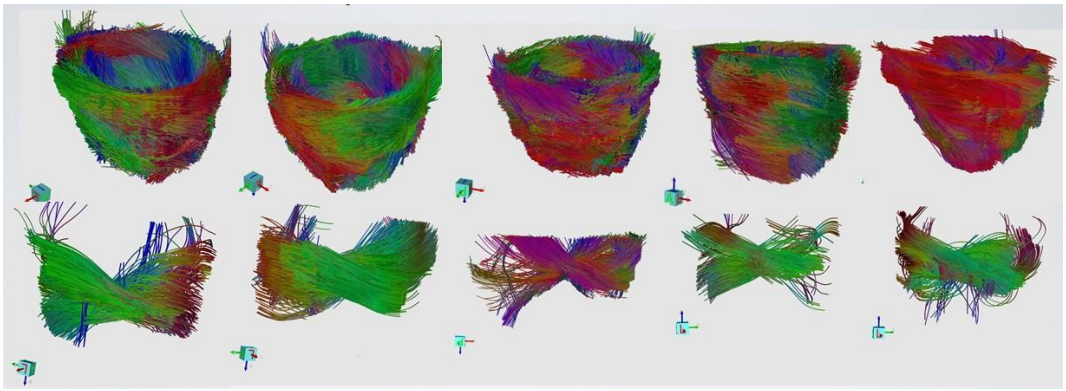

Fig. 3.12. 3D fiber tracts obtained from PCATMIP of 5 volunteers.

3.5 Discussion

As mentioned before, cardiac motion is three-dimensional, both in the longitudinal direction (through-plane motion) and within the imaging plane (in-plane motion). Our experiments confirmed much greater amplitudes of the longitudinal motion. The relative in-plane displacement amplitude ranged from 0.01 to 3.5 millimeters and the relative longitudinal displacement ranged from 0.01 to 10 millimeters at the pixel level of the DENSE data. As a consequence, we only considered cardiac longitudinal motion in the analysis of the impact of cardiac motion on diffusion signal loss in the present cardiac *in vivo* DTI study. This is in line with the work by (Fischer et al. 1995), which also stressed the importance of longitudinal motion; this has been considered the most challenging issue in phase sensitive MR imaging.

From the results shown in Fig. 3.5, the relationship between cardiac motion and DW SI is not strictly mono-exponential, which implies other possible approximations to motion modeling problems. Our model was obtained for a single-shot twice-refocused spin-echo EPI sequence with optimized bipolar diffusion encoding gradients; other diffusion encoding schemes will most likely lead to other signal loss dependency.

Using a PLI simulated DW dataset as reference for the ground truth and combining it with our diffusion model, we can provide simulations that illustrate the efficacy of the PCATMIP method to recover signal loss due to cardiac motion. We analyzed the displacement in only six sectors following AHA standardized segmentation rather than the myocardial motion at the pixel level. The difference in resolution between the PLI ($100 \times 100 \times 500\ \mu m^3$) and the DENSE ($3.5 \times 3.5 \times 8\ mm^3$) data did not allow us to obtain motion information for each pixel in the PLI data. Moreover, we did not compare the motion at different transmural zones from the endocardium to epicardium. With transmural segmentation, we may try to search for other models given experimental cardiac motion data and also find better fitting techniques for a given motion model. Additionally, we did not consider the effects of diffusion gradient direction sampling schemes. Because the same gradient directions were used in the simulation, this issue does not affect the comparison of motion effects.

Noise simulation revealed that the FA value is 0.82 ± 0.07 in the presence of noise, compared to the original value (0.56). The effects of noise on the FA estimation have been reported in the literature, which shows that, in anisotropic systems, the largest eigenvalue is overestimated and the lowest eigenvalue is underestimated in general (Pierpaoli & Basser 1996). The mean FA of the Ref + noise + motion was 0.62 without PCATMIP, compared to the original value of 0.56. The mean MD of the Ref + noise + motion was 2.12 $\times 10^{-3}$ mm^2/s compared to the original value of 0.78 $\times 10^{-3}$ mm^2/s. Our results therefore showed that while cardiac motion was associated with an overestimation of both FA and MD, the effect was greater for MD. For the *in vivo* experiments, the mean FA value for 1TD (without PCATMIP) over the six volunteers (0.56) was higher than when using PCATMIP (0.43); this was due to the higher noise level and motion-induced signal loss. The MD values showed differences between before and after measures using PCATMIP. With 1TD, signal loss resulted in an overestimation of MD (1.37 ± 0.16 $\times 10^{-3}$ mm^2/s). PCATMIP yielded a significantly lower MD (0.75 ± 0.12 $\times 10^{-3}$ mm^2/s) than that obtained using 1TD. The *in vivo* results showed that motion-induced signal loss could be minimized by using the PCATMIP method, which is consistent with the simulation results. This is in line with previous reports of human brain studies that also demonstrated that noise and motion cause a bias for FA and MD and that motion correction strategies help to improve the accuracy of DTI indices (Ling et al. 2012; Tijssen et al. 2009).

The shifted acquisition scheme combined with the PCATMIP post-processing allowed us to select, after motion correction and for each pixel, the optimal time point during the cardiac cycle with minimal signal loss due to cardiac motion. The PCATMIP post-processing over multi-TD SIs clearly maximized the diffusion information in the images while reducing the influence of motion. Note that in some patients with spatial heterogeneity of motion (dyskinesia, akinesia), it might be difficult to find a unique TD that could cancel the effects of motion in the entire myocardium. It is therefore retrospectively not always possible to determine a best TD at which the DTI data would be acquired with minimal motion impact. Nevertheless, the chosen reference TD for 1TD was the one that exhibited the highest homogeneity and SI in the myocardium.

The first important result was that PCATMIP operation over multi-TD DW images clearly and always improved image quality (increased SNR resulting from compensated signal loss compared to that obtained with 1TD).

The range of elevation angles used in the simulation was restricted to 90° in order to compare to the data reported in the prior PLI study (Jouk et al. 2007). After processing by PCATMIP, the range of elevation angles (Fig. 3.7 (i)) in the simulation study was narrower ($41^\circ \pm 13^\circ$ on the endocardium and $35^\circ \pm 12^\circ$ on the epicardium) than the reference (Fig. Fig. 3.7 (a), $57^\circ \pm 9^\circ$ on the endocardium and $51^\circ \pm 13^\circ$ on the epicardium). This implies that PCATMIP could not completely eliminate the impact of motion and noise on the fiber architecture, but it could still reduce the effect of physiological motion. Motion resulted in a reduced range of fiber angles. The elevation angle range obtained in the *in vivo* DTI study was narrower (approximately from 41° on the endocardium to -34° on the epicardium) than in previously reported *ex vivo* human cardiac studies (Lombaert et al. 2012). We must account for many factors that may influence the elevation angle range, i.e., *in vivo* or *ex vivo* data, data

acquired at different cardiac phases, spatial resolution, motion artifacts and segmentation method. The study reported by Lombaert et al. (Lombaert et al. 2012) on healthy *ex vivo* human hearts showed that the helix angle varied from $66^{\circ} \pm 15^{\circ}$ on the endocardium to $-41^{\circ} \pm 26^{\circ}$ on the epicardium. The histological study of postmortem human hearts by Greenbaum et al. showed a distribution of helix angles from approximately 40° on the endocardium to approximately -40° on the epicardium (Greenbaum et al. 1981). The narrower elevation angle range may be caused by signal loss in the DW images due to residual noise or residual motion. Another possible cause of narrower angle ranges may be related to the fact that the angles were obtained by averaging the coarser in-plane resolution voxels inside the transmural layers. Because coarser resolution neighboring voxels have greater angle difference, the obtained angle has, after averaging, a smaller value in total.

3.6 Conclusion

We have proposed a multimodal approach to assess the effects of cardiac motion on *in vivo* diffusion tensor parameters of the human heart. With the aid of the ground truth provided by the combined use of PLI data, simulated DW images and motion information derived from DENSE imaging, the proposed cardiac motion model has been shown to elegantly allow us to investigate the relationship between cardiac motion and *in vivo* diffusion tensor parameters of the human heart. Additionally, this method allowed us to quantify the impact of motion on diffusion tensor parameters. Cardiac motion resulted in large signal loss in DW images, an overestimation of both FA and MD, and a reduced range of fiber angles between the endocardium and epicardium. We also showed that 3D fiber architecture can be retrieved from *in vivo* DTI data acquired under free-breathing conditions using the shifted TD acquisition scheme combined with adequate post-processing based on image registration and PCATMIP. The FA was 0.43 ± 0.05 and MD was $0.75 \pm 0.12 \times 10^{-3}$ mm^2/s among all volunteers. From the angle maps, the myocardial fiber orientation of the LV wall showed a circularly symmetric pattern, ranging from 41° on the endocardium to -34° on the epicardium. The results showed that the combined use of shifted TD acquisitions and adequate post-processing based on registration and PCATMIP effectively improves the quality of *in vivo* DW images as well as the subsequent measurement accuracy of fiber architecture properties. This suggests new directions toward obtaining *in vivo* human myocardial fiber architecture in clinical conditions.

Chapter 4

In vivo DTI of the human heart with free-breathing using sliding window multiple delay DT imaging

Contents

Abstract

This chapter mainly focuses on in vivo DTI to obtain the myocardial fiber structure of the human heart under free-breathing conditions and without resorting to respiratory gating. We propose novel approaches that combine multiple shifted TD acquisitions and post-processing methods. First, we perform multiple shifted TD acquisitions at end diastole. We use image co-registration and PCATMIP to addresses physiological motion effects. Ten slices across the entire heart were acquired under free-breathing conditions. For each slice, 12 DW images corresponding to 12 diffusion gradient directions were obtained. Tensor fields were calculated, from which the in vivo fiber architecture properties were derived. The myocardial fiber orientation of the LV showed a circularly symmetric pattern, from about -34° on the epicardium and to 41° on the endocardium, which reflects well the rotation characteristic of cardiac fibers. This is the first result on the entire in vivo heart DTI of healthy volunteers under free-breathing conditions. This study demonstrates that the combination of multiple shifted TD acquisitions and dedicated image post-processing can compensate for physiological motion effects, which allows us to obtain 3D fiber architectures of the human heart in vivo. Such acquisition and processing scheme suggests new solutions to signal loss problems associated with bulk motion, which are promising for obtaining in vivo human myocardial fiber architecture properties in clinical conditions.

Résumé en français

Ce chapitre porte principalement sur l'imagerie in vivo du tenseur de diffusion (diffusion tensor imaging—DTI) en vue d'obtenir la structure des fibres myocardiques du cœur humain dans des conditions de respiration libre sans recourir au gating respiratoire. Nous proposons de nouvelles approches consistant à combiner des acquisitions à retards de déclenchement multiples (trigger delay—TD) et des méthodes de post-traitement. D'abord, nous réalisons des acquisitions avec multiples TD décalés en fin de diastole. La méthode s'attaque au problème d'effets de mouvement physiologique sur DTI cardiaque in vivo en utilisant les techniques de recalage et de PCATMIP. 10 coupes sur l'ensemble du cœur ont été acquises dans des conditions de respiration libre. 12 DW images correspondant aux 12 directions de gradient de diffusion ont été obtenues pour chaque coupe. Les champs de tenseurs sont calculés, à partir desquels les propriétés de l'architecture des fibres in vivo sont dérivées. L'orientation des fibres du LV présente un motif de symétrie circulaire, d'environ -34° sur l'épicarde et à 41° sur l'endocarde, ce qui traduit bien la caractéristique de rotation de fibres cardiaques. C'est le premier résultat sur in vivo DTI d'un cœur entier chez les volontaires sants dans des conditions de respiration libre. Cette étude démontre que la combinaison des acquisitions avec des TD décalés et des post-traitements d'images peut compenser les effets de mouvement physiologique, ce qui permet d'obtenir l'architecture 3D du cœur humain in vivo. Ce système d'acquisition et de traitement suggère de nouvelles solutions au problème de perte du signal due au mouvement, qui sont prometteuses pour obtenir les propriétés de l'architecture des fibres myocardiques du cœur humain in vivo, dans des conditions cliniques.

4.1 Introduction

Respiratory gated approaches (Gamper et al. 2007; Nielles-Vallespin et al. 2012) were often preferred to minimize the effect of respiratory motion for DTI acquisitions although they can still be obtained in multiple breath-hold acquisitions (Delattre et al. 2012). However, respiratory gated strategies imply increased acquisition time (Ehman et al. 1984), since only 30-40% of the whole respiratory cycle (Summers et al. 2006) is actually used for the acquisitions.

The motivation is high for a 100% duty cycle free-breathing DTI acquisitions, compatible with a high patient compliance rate. The biggest problem in in vivo cardiac DTI is the large signal loss caused by intrascan motion induced by the combined respiratory and cardiac motion. First attempt to collect in vivo human diffusion data on the heart was achieved using a stimulated echo acquisition mode (STEAM) (Edelman et al. 1994). Cardiac diffusion imaging using a STEAM preparation presents the advantage of having much shorter scan time per RR interval, thus reducing the intrascan motion, but inherently doubles the total scan time with respect to spin-echo sequences (Gamper et al. 2007) since encoding and decoding must take place in two consecutive cardiac cycles. The study (Reese et al. 1996) showed the feasibility of mapping fiber orientations quantitatively in human subjects; they found that cardiac DW imaging has a significant sensitivity to myocardial deformation due to the motion. A method to overcome the myocardial strain effect on cardiac diffusion imaging has been proposed. This method requires an additional strain measurement to de-convolve the strain effect by computation. In (Tseng et al. 2000) was presented a method of obtaining accurate diffusion data by requiring an additional sequence measurement and defining a "sweet spot" in the cardiac cycle where the net effect of strain on the observed diffusion approximates zero. The author in (Dou et al. 2009) developed a stimulated-echo acquisition mode technique for cardiac DW imaging in vivo, which has the major drawback of an inherently low signal-to-noise ratio (SNR) efficiency. In (Gamper et al. 2007) a spin echo approach with bipolar diffusion encoding gradient was proposed to make the sequence insensitive to systolic bulk motion of the heart. Several implementations (Edelman et al. 1994; Gamper et al. 2007) were used to compensate for motion including retrospective navigators and breath-hold, which required acquisition times of about 7 minutes per slice. In the majority of these studies, however, either a single (Dou et al. 2009) or three (Nielles-Vallespin et al. 2012) slices could be acquired. A 3D reconstruction of cardiac fiber architecture to derive in vivo human atlas using conformal mapping schemes (Toussaint et al. 2010) was proposed. Nevertheless, either three (Nielles-Vallespin et al. 2012) or five (Toussaint et al. 2013) slices are not adequate due to the low spatial resolution (8 mm slice thickness) in the slice direction for the whole 3D fiber architecture reconstruction. The 3D cardiac fiber architecture construction using streamline would benefit from a higher number of slices.

The aim of this study is to investigate the feasibility of in vivo cardiac DTI and 3D fiber tracking of the entire heart under free-breathing conditions and without resorting to respiratory gating. To this end, motion-reduced in vivo cardiac DTI datasets were first acquired at end-diastole using a multiple shifted TD acquisition strategy. Then a non-rigid registration method (Guetter et al. 2011) was used to correct interscan motion caused by

respiratory motion. The robust PCATMIP method (Pai et al. 2010) based on principal component analysis (PCA) and temporal maximum intensity projection (TMIP) was applied to the registered DW images to compensate for the signal loss induced by cardiac motion. The so corrected DW images were finally used to calculate the tensor field, from which the in vivo fiber architecture (3D fiber tracts) and diffusion parameters such as FA, MD, and HA were derived.

4.2 Methods

4.2.1 **Data acquisition**

The whole heart in vivo diffusion data was acquired the same as used in chapter 3 (DW imaging with scheme 2).

4.2.2 **Interscan motion correction (MOCO)**

Respiratory and cardiac motion affect free-breathing diffusion acquisitions in two ways, depending on the time scale of motion with respect to image acquisition time. First, there is the interscan motion corresponding to the movement of the organ during the period between two consecutive diffusion acquisitions. Second, the intrascan motion occurs during the measurement of the diffusion data along the successive trajectories of k-space. The intrascan motion leads to phase-related artifacts, which manifest itself as severe signal loss of the DW images.

To correct interscan motion, a fast non-rigid image registration algorithm was applied to the multi-directional and multi-TD DW images. In brief, non-rigid registration was first performed on all the TD DW images for each gradient direction (co-registration of 10 ms shifted images per direction). Then, in a second step, the co-registration was performed in all the 12 diffusion directions. The flow chart describing the whole co-registration is illustrated in Fig. 4.1.

Let's consider the two images, I_{ref} and I_{flo}. Deformable image registration is the search for a function Φ_{12} that transforms each location x using a displacement field u such that both images are accurately aligned: $\Phi_{12}(x) = x + u(x)$. This function is searched in a set of admissible functions such that it minimizes an energy functional ξ, and the minimizing function Φ represents the solution of the deformable registration problem: $\Phi_{12} = \arg\min \xi(I_{ref}, I_{flo,}\Phi_{12})$, where ξ depends on the two images I_{ref}, I_{flo} and Φ_{12} describing the transformation from I_{flo} to I_{ref}. The deforming function Φ_{12} can be retrieved by desending the gradient of ξ using an iterative shceme of composing incremental updates of the deformation: $\Phi_{12,k+1} = \Phi_{12,k} \circ (id + \tau \nabla_u \xi G_\sigma)$, with τ controlling the step size along the gradient, and G_σ denoting a Gaussain filter. The energy functional ξ can be measured by

$$\xi_{12} = \int (I_{ref} - I_{flo} \circ \Phi_{12})^2 + \lambda \xi_{smooth}(u) dx \tag{4.1}$$

$$\xi_{21} = \int (I_{ref} \circ \Phi_{21} - I_{flo})^2 + \lambda \xi_{smooth}(v) dx \tag{4.2}$$

where ξ_{12} denotes $\xi(I_{ref}, I_{flo}, \Phi_{12})$, and ξ_{smooth} preventing fast variations of the displacements u and v respectively. A registration method is symmetric if the equality is satisfied:

$$\xi(I_{ref}, I_{flo}, \Phi_{12}) = \xi(I_{flo}, I_{ref}, \Phi_{12}^{-1}) \tag{4.3}$$

The invers transformation Φ_{12}^{-1} describes the transformation from I_{flo} to I_{ref} and satisfies

$$\Phi_{12} \circ \Phi_{12}^{-1} = \Phi_{21} \circ \Phi_{21}^{-1} = id, \tag{4.4}$$

where $\Phi_{21}(x) = x + v(x)$. In case only the latter constraint is satisfied by a registration method, it is called inverse-consistent. The following energy functional of the form

$$\Rightarrow \xi(I_{ref}, I_{flo}, \Phi) = \xi(I_{ref}, I_{flo}, \Phi_{12}) + \xi(I_{flo}, I_{ref}, \Phi_{21}). \tag{4.5}$$

In this deformable registration algorithm that solves a symmetric energy functional and provides forward as well as inverse deformations at little performance loss to the one-directional and asymmetric estimation. This is achieved by making use of the theory of multiobjective optimization stating that two or more conflicting objectives can be optimized simultaneously subject to certain constraints.in this method, the two competing objectives are forward and backward deformation estimation under the constrain that both are to be inverse of each other. In order to solve the symmetric registration problem above, here uses an interleaved optimization scheme alternating the optimizing directions at each iteration. The outline of the first little iteration in such an interleaved optimization scheme is

$$\begin{aligned}
&\Phi_{12,0} = \Phi_{12,0}^{-1} = \Phi_{21,0} = \Phi_{21,0}^{-1} = id, \\
&\Phi_{12,1} = \Phi_{12,0} \circ (id + \tau \nabla_u \xi_{12} G_\sigma), \\
&\Phi_{21,1_initial} = \Phi_{12,1}^{-1}, \\
&\Phi_{21,2} = \Phi_{21,1} \circ (id + \tau \nabla_v \xi_{21} G_\sigma), \\
&\Phi_{21,2_initial} = \Phi_{12,2}^{-1}, \\
&\Phi_{12,3} = \Phi_{12,2} \circ (id + \tau \nabla_u \xi_{12} G_\sigma), \\
&\vdots
\end{aligned} \tag{4.6}$$

with an iterative inverse transformation estimation step. Forward $\Phi_{12,k}$ and backward $\Phi_{21,k}$ transformations at iteration k are forced to be inverse by the fixed-point iteration scheme:

$$\varphi_{i+1}^{-1}(x) = \frac{1}{2}(-\varphi_i(id \circ \varphi_i^{-1}(x)) + \varphi_i^{-1}(x)), i = 0, \ldots, N \tag{4.7}$$

where N describe how many iterations should be taken for the estimation. Setting $\varphi = \Phi_{12,k}$ and $\varphi^{-1} = \Phi_{21,k}$ enforces the inverse condition. The correction step can be repeated after the optimization has converged in order to further decrease the inverse-consistency error. The interleaved optimization scheme can be applied to any ξ that is differentiable and wholegradient exist and can be computed. This method focuses on the local cross-correlation

(LCC) here because it is a robust and accurate similarity measure in clinical MRI. The LCC is defined as

$$\xi_{12}(x)=\sum_{i,j}^{N_{nb}}\frac{\sum_{nb}(I_{ref}(i,j)-\overline{I_{ref}})(I_{flo}\circ\Phi_{12}(i,j)-\overline{I_{flo}})}{\sqrt{\sum_{nb}(I_{ref}(i,j)-\overline{I_{ref}})^2(I_{flo}\circ\Phi_{12}(i,j)-\overline{I_{flo}})^2}}, \tag{4.8}$$

where $\overline{I_{ref}}$ and $\overline{I_{flo}}$ are the mean values of the neighborhood *nb* around location (i, j) in both images, and N_{nb} determines the number of elements in that neighborhood.

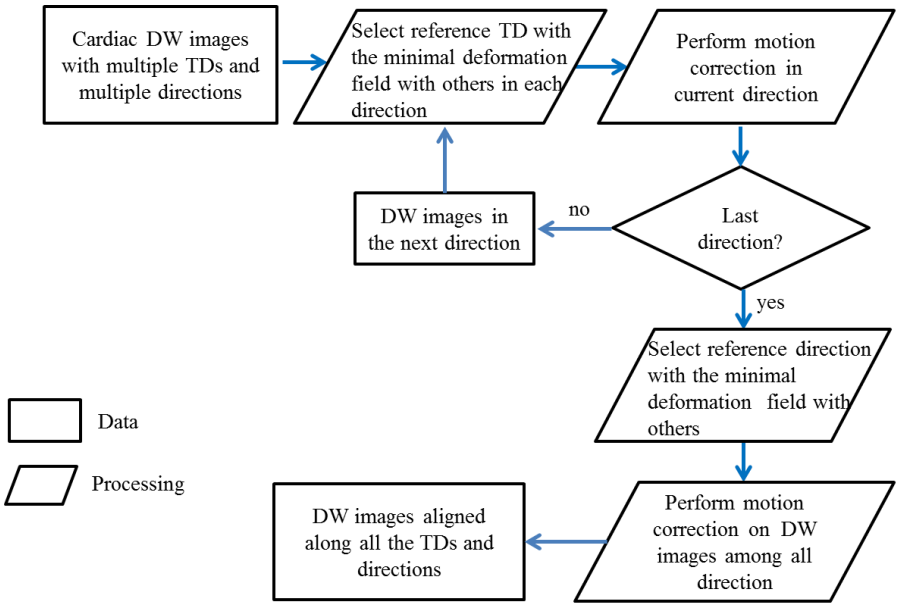

Fig. 4.1 Block diagram of motion correction for DW images.

For the first registration step, the best reference TD for each direction is determined by the following approach: given a series of *N* images (here, 10 TD images per direction), the registration is first performed by selecting every image as the reference (Fig. 4.1). This results in *N* series of deformation fields corresponding to *N* reference TD choices. For each of the *N* series, the mean deformation is computed. The TD that corresponds to the minimum mean deformation is selected as the reference, which allows us to minimize the total deformation field caused by non-rigid image registration. Once the reference TD was found, non-rigid registration was performed on all the TDs for each direction. Then the same procedure is repeated for all the diffusion gradient directions. The image registration (interscan motion correction) was performed using a Siemens Prototype code within MATLAB (R2010b, the Mathworks, Inc, Natick, MA, USA).

4.2.3 **Intrascan motion compensation**

After interscan motion correction, we used the PCATMIP method to obtain the final intrascan and interscan motion-corrected DW images. PCATMIP involves repeated DWI

acquisitions over time, and the signal at each pixel fluctuates due to several factors. One factor is the physical movement of the anatomical features due to physiological motion. This can be effectively corrected with non-rigid-body image registration. However, intensity fluctuation remains due to two other factors: bulk motion-induced intensity drops and random noise. This random noise needs to be reduced or removed to isolate the maximum signal and regard it as the one with minimum motion-induced loss. For this, we exploit the fact that physiological motion is mostly cardiac and respiratory, which are mechanically transmitted to other areas. While some organs have active peristaltic motion, these are slow and temporally coordinated in nature. Therefore, motion-induced signal fluctuations in neighboring pixels are temporally correlated, while random noises are not. With this in mind, we look at a neighborhood defined by a boxcar and determine through PCA how many independent temporal behaviors (modes) are present. We then determine how many of these have amplitudes that exceed the random noise threshold and therefore represent real physiological fluctuations. If we include only these modes in reconstructing the signals in the boxcar, random noise will be reduced. A further consideration is that the size of the boxcar needs to be large enough to distinguish coordinated physiological effects from random noise, while small enough to capture local pattern of motion-induced fluctuation.

From the final corrected DW images the tensor fields were calculated. The PCATMIP post-processing was carried out within IDL (Research systems, Inc., Boulder, CO, USA).

4.3 In vivo cardiac diffusion parameters calculation

The image post-processing was performed using a home-written MATLAB (R2010b, the Mathworks, Inc, Natick, MA, USA) program. The diffusion parameters were measured in the LV after the manual segmentation of the myocardium in b0 image (null diffusion gradient) and papillary muscles were excluded. The diffusion tensor was calculated for each voxel using the signal intensity data from the 12 DW images and b0 image. The eigenvalues and eigenvectors were then obtained for each tensor. Two quantitative diffusion parameter maps were derived from eigenvalues and eigenvectors: FA and MD (Wu et al. 2006). FA is an index of the degree of deviation of the observed diffusion from isotropic, and MD is the first moment of the diffusion tensor, which is the average diffusivity. The principal eigenvector of the diffusion tensor was taken to represent mean intravoxel fiber orientation. HA was computed as the angle between the short-axis plane and the projection of the angle on the tangent plane of epicardium (Fig. 4.2).

To evaluate the benefit of the PCATMIP for free-breathing in vivo cardiac DTI, comparison was performed with the one TD (referred to as “1TD” in the following) method and averaging operation (AVG, by averaging the 10 TD DW images instead of using PCATMIP). Finally, the 3D fiber tracts were constructed using the conventional streamline algorithm (Fillard et al. 2003; Xu et al. 2003). The parameters for judging local continuity include minimal FA value. It can display the path of the principle direction of diffusion in anisotropic tissue until termination in areas of low anisotropy. The parameters used for tracking are, 0.05 for the FA threshold and 20 voxels for the minimum length.

Diffusion tensor parameters differences among the image processing methods were assessed using 2-way repeated analysis of variance (ANOVA). Measurements were presented

as means ± SD (standard deviation) and P<0.05 was considered as statistically significant. All statistical computations were performed using SPSS 20 (SPSS Inc., Chicago, IL, USA).

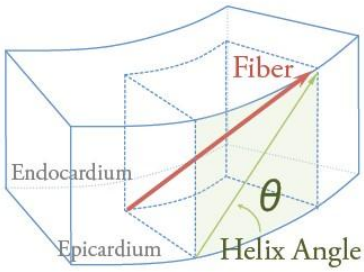

Fig. 4.2 Helix angle definition

4.4 In vivo cardiac diffusion parameters analysis

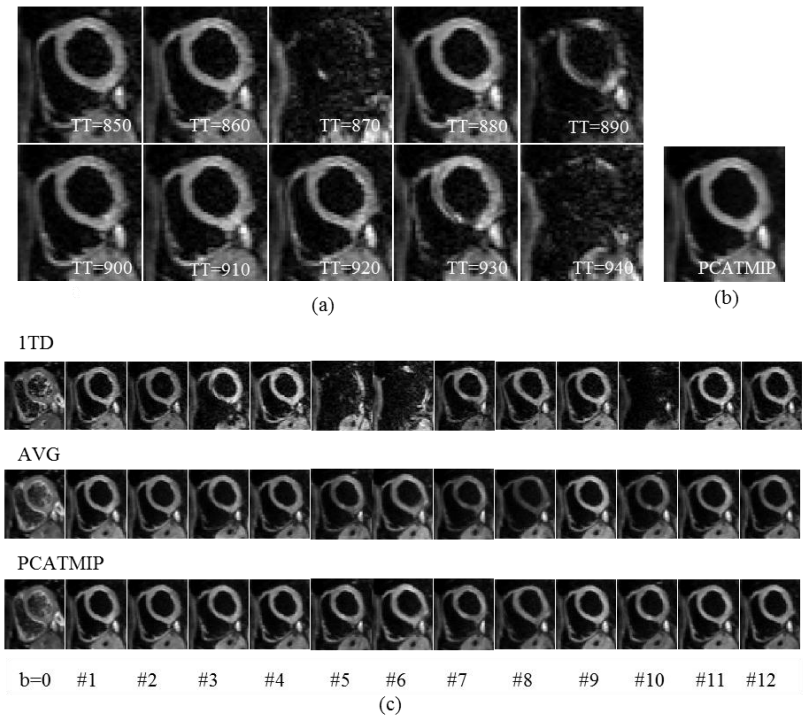

Fig. 4.3. (a) Free-breathing short-axis DW images resulting from one diffusion prepared acquisition performed at 10 shifted different time points in diastolic on a volunteer. Visible spatial signal intensity fluctuation resulting from spatially variable intrascan motion, varies from slight hypo-intensities impacting some of the myocardial segments to entire missing parts of one or more segments. (b) Corresponding corrected DW images using PCATMIP; (c) DW images corresponding to 12 diffusion gradient directions as well as b0 images. Top: A single delay acquisition performed at an optimized diastolic time point (1TD); for some directions, part of the myocardium disappeared due to the cardiac or respiratory motion. The chosen TD was the one that exhibited higher signal intensity (corresponding to minimal motion) for most of the directions. Middle: DW images processed using the AVG method. Bottom: DW images retrieved using PCATMIP post-processing.

Fig. 4.3 shows an example of in vivo cardiac DW images of a volunteer acquired near the base of the heart. Although the multiple shifted TD acquisitions were collected at end-diastole where in-plane and through-plane heart motion of the LV were minimal, intensity fluctuations due to not only the residual cardiac motion but also the respiratory intrascan motion can be seen from the free-breathing acquisitions.

Fig. 4.3(a) gives registered DW images of the 10 TD acquisitions for one diffusion gradient direction. We observe that signal loss throughout the myocardium is visible. Fig. 4.3(b) shows the corrected DW image by applying PCATMIP post-processing to the 10 TD DW images. Fig. 4.3(c) shows motion corrected DW images recovered from raw images in 12 diffusion gradient directions as well as b0 images using different methods. The DW images acquired with 1TD (top row) exhibits higher artifact rate and severe signal loss: for some diffusion gradient directions (e.g. direction 5 and 6), part or entire of the myocardium have disappeared during free-breathing acquisition. If this is the case, this will yield inaccurate diffusion tensor parameters calculated from the available signal intensities of these directions. The middle row of Fig. 4.3(c) gives the DW images obtained using the AVG method. The motion artifact contamination rate was reduced, but the averaging operation resulted in global signal intensity fluctuation that corrupts the directional information of the diffusion weighted scans. PCATMIP algorithm (bottom row in Fig. 4.3(c)) further reduced the motion artifacts and intrascan signal loss.

Fig. 4.4 shows the FA and MD maps of the same volunteer as in Fig. 4.3, which were calculated from the Log-Euclidean interpolated tensor fields. The mean FA and MD values in the LVs of all the volunteers are summarized in table 1. We can see that FA_{1TD} (0.56 ± 0.16) is higher than FA_{AVG} (0.33 ± 0.10) and $FA_{PCATMIP}$ (0.43 ± 0.05). The MD maps show significant differences among the three methods. $MD_{PCATMIP}$ (0.75 ± 0.12 $\times 10^{-3}$ mm^2/s) was lower than MD_{1TD} (1.20 ± 0.37 $\times 10^{-3}$ mm^2/s) and MD_{AVG} (1.10 ± 0.25 $\times 10^{-3}$ mm^2/s). Using the PCAMTIP as a reference, significant difference were observed between processing methods ($P<0.05$).

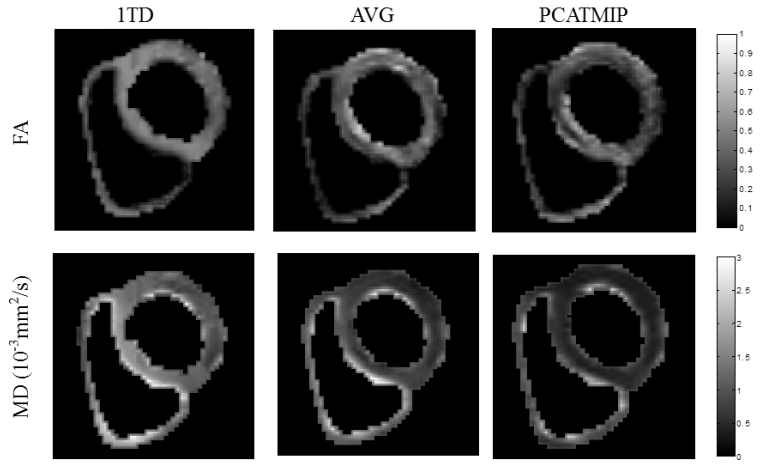

Fig. 4.4. FA and MD maps calculated from tensor fields. Images show FA and MD maps obtained from 1TD, AVG and PCATMIP approaches described in Fig. 4.3. Left: 1TD; middle: AVG; right: PCATMIP.

The mean values over the six volunteers at different longitudinal locations were reported in table 4.2. After processing by PCATMIP, the FA values were 0.43 ± 0.05, 0.41 ± 0.10 and 0.39 ± 0.08 for base, mid-cavity and apex, respectively. The MD values were 0.75 ± 0.12 $\times 10^{-3}$ mm^2/s, 0.79 ± 0.20 $\times 10^{-3}$ mm^2/s and 0.87 ± 0.21 $\times 10^{-3}$ mm^2/s for base, mid-cavity and apex, respectively. Using the values of the mid-cavity as a reference, there was no statistically significant difference between different heart locations (P>0.05). The mean global FA and MD were defined the values averaged from all three slices (base, mid-cavity and apex). When analyzed by different methods, the global FA was 0.59 ± 0.15, 0.33 ± 0.10, and 0.41 ± 0.09 for 1TD, AVG and PCATMIP, respectively. The global MD was 1.38 ± 0.30 $\times 10^{-3}$ mm^2/s, 1.12 ± 0.27 $\times 10^{-3}$ mm^2/s, and 0.80 ± 0.20 $\times 10^{-3}$ mm^2/s for 1TD, AVG and PCATMIP, respectively. Significant differences were observed depending on the methods. 1TD yielded 43% ± 67% and 72% ± 50% increases in FA and MD with P=0.005 and P=0.003 when compared to those measured from PCATMIP. AVG yielded -20% ± 11% and 40% ± 35% increases in FA and MD with P=0.027 and P=0.008 when compared to those measured from PCATMIP.

Table 4.1. FA and MD values in the LVs of all the volunteers (the 9th slice, near the heart base). The results show that both AVG and PCATMIP yielded systematically lower values and lower SD than 1TD. MD values are in units of 10^{-3} mm^2/s.

	FA ± SD					
	Vol#1	Vol#2	Vol#3	Vol#4	Vol#5	Vol#6
1TD	0.59 ±0.08	0.56±0.02	0.60±0.11	0.60±0.13	0.57±0.09	0.46±0.04
AVG	0.35± 0.09	0.28±0.04	0.33±0.06	0.27±0.07	0.25±0.04	0.32±0.07
PCATMIP	0.51±0.02	0.48±0.02	0.42±0.02	0.39±0.03	0.34±0.01	0.39±0.01
	MD ± SD					
	Vol#1	Vol#2	Vol#3	Vol#4	Vol#5	Vol#6
1TD	1.23±0.19	1.52±0.08	1.57±0.14	1.41±0.16	1.25±0.08	1.23±0.08
AVG	1.17±0.14	1.34±0.08	0.91±0.01	1.02±0.14	1.09±0.18	1.06±0.13
PCATMIP	0.77±0.09	0.88±0.04	0.58±0.08	0.74±0.07	0.88±0.10	0.64±0.03

Table 4.2. Global mean FA and MD values in the LVs of different longitudinal locations of the heart. MD values are in units of 10^{-3} mm^2/s.

FA	Base	Mid-cavity	Apex	Mean ± SD
1TD	0.56±0.16	0.63±0.17	0.59±0.15	0.59±0.15
AVG	0.33±0.1	0.33±0.13	0.32±0.11	0.33±0.10
PCATMIP	0.43±0.05	0.40±0.1	0.39±0.08	0.41±0.09
MD	Base	Mid-cavity	Apex	
1TD	1.40±0.37	1.43±0.28	1.34±0.24	1.38±0.30
AVG	1.07±0.25	1.14±0.21	1.15±0.32	1.12±0.27
PCATMIP	0.75±0.12	0.79±0.20	0.87±0.21	0.80±0.20

The HA maps obtained from 1TD, AVG as well as PCATMIP are shown in Fig. 4.5. It can be observed that the HA map of PCATMIP exhibit decreasing values from endocardium to epicardium. Left-handed epicardial helix orientations were assigned a negative angle and right-handed endocardial helix orientations a positive helix angle as described by (Streeter et al. 1969). Fig. 4.5 (b) shows the mean ± SD of the HA values over all volunteers in the five layers obtained using the three methods. With PCATMIP, the mean HAs for all the volunteers varied from $32^\circ \pm 9^\circ$ on the endocardium layer, through $24^\circ \pm 5^\circ$ on the mid-endocardium layer and $13^\circ \pm 5^\circ$ on the mid-wall, $-7^\circ \pm 7^\circ$ on the mid-epicardium layer to $-27^\circ \pm 7^\circ$ on the epicardium layer. The helix angle variation from endocardium to epicardium, which is a very important characteristic of the human cardiac fiber architecture, can be clearly seen.

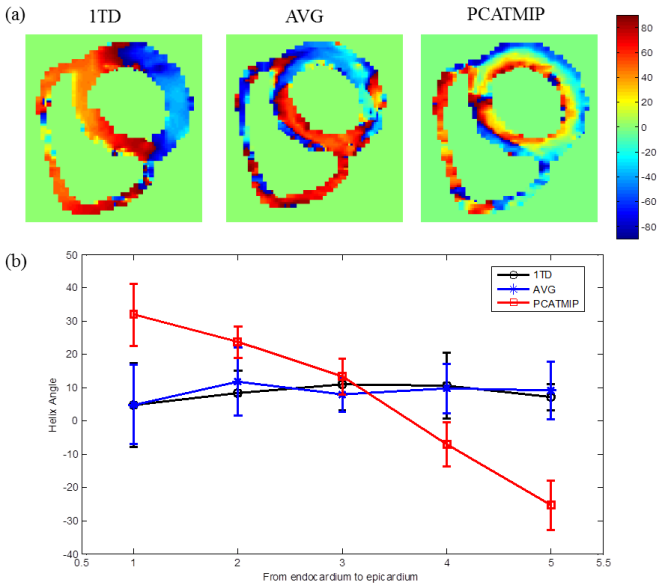

Fig. 4.5 HA values of in vivo myocardium in the LV. (a) HA maps derived respectively from 1TD, AVG and PCATMIP. (b) The global HA values over all volunteers in the endocardium, mid-endocardium, mid-wall, mid-epicardium and epicardium layers. The three curves in the plot correspond to 1TD (black line), AVG (blue line) and PCATMIP (red line) methods, respectively.

The tensor fields derived from the three methods are shown in Fig. 4.6. The fiber orientation was displayed on a voxel-by-voxel basis and using cylinder glyphs. For the tensor field of 1TD and AVG method, the orientation of the tensors changes disorderly. In contrast, with PCATMIP, the orientation of tensors changes uniformly, as indicated by their colors varying from red on the anterior-lateral to green on the inferior-lateral. The fiber angles changes from positive on the endocardium to the negative on the epicardium. This means that the tensor field resulted from PCATMIP method allows better reflecting the fiber orientation rotation.

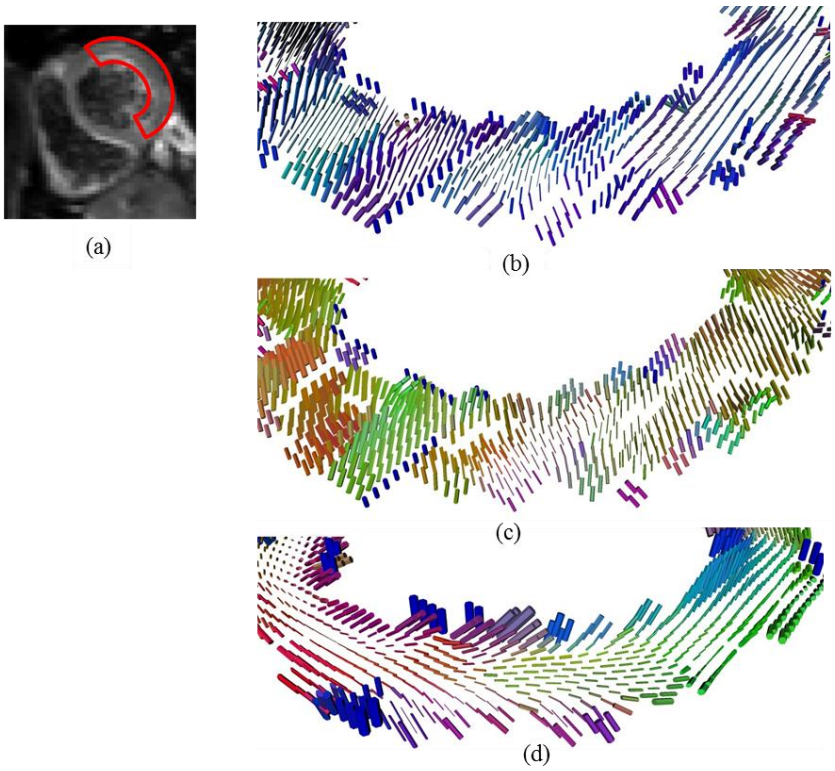

Fig. 4.6 3D visualizations of tensor field derived from (b) 1TD, (c) AVG and (d) PCATMIP zoomed from (a) the red ROI located in the lateral wall. Fiber orientation was seen on a short-axis slice. The r, g, b color of the tensors indicates the local orientation of the fiber. The transmural variation is visible in the LV for the PCATMIP result.

At last, the examples of in vivo 3D fiber architecture derived from 1TD (Fig. 4.7 (a) and (b)), AVG ((c) and (d)) and PCATMIP ((e), (f), and (g)) are presented. Using PCATMIP approach, fiber orientation of the LV shows a circularly symmetric pattern. For better depiction of the helical structure, a shutter located at the lateral wall viewed from the epicardial surfaces was applied (Fig. 4.8). Nevertheless, we can recognize in particular the main helical structure of the LV, demonstrating that the consistent spiral fiber architecture can be obtained from the tensor fields calculated using PCATMIP approach.

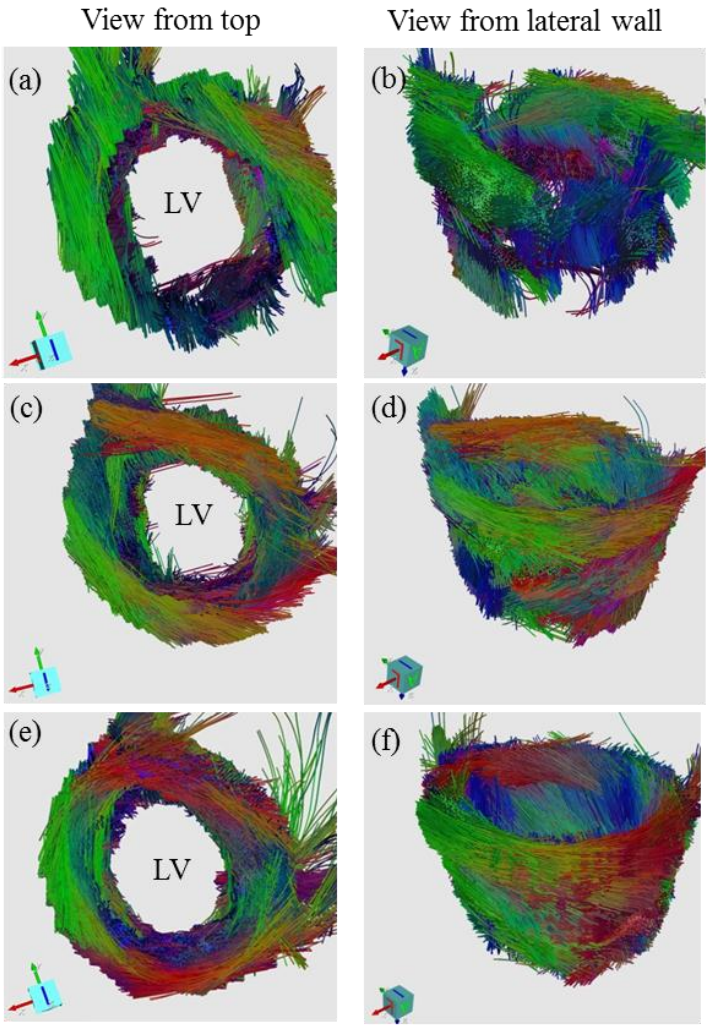

Fig. 4.7 In vivo 3D fiber tracts of a volunteer derived from 1TD ((a), (b)), AVG ((c), (d)) and PCATMIP ((e), (f)) method. The r, g, b color of the tracked fibers indicates respectively the x, y, z components of the local orientation of the fiber.

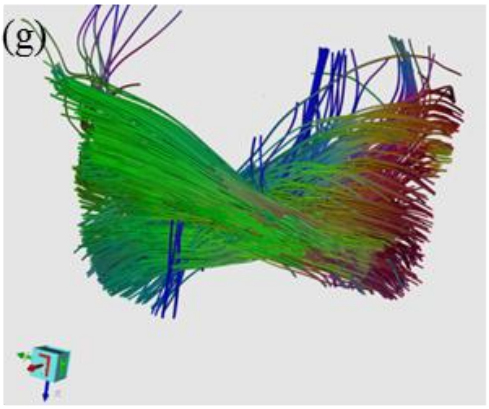

Fig. 4.8 A shutter fiber tracts of a volunteer derived from PCATMIP method.

4.5 Discussion

This study investigates in vivo human cardiac DTI in free-breathing conditions. It enables us to obtain coherent fiber tractography of the entire heart. And the HA distribution is consistent with the helical structure of the myocardial fibers (Nielles-Vallespin et al. 2012). The results demonstrate the capacity of PCATMIP to preserve the integrity of the directional information contained in the multi-directional DW acquisitions, which was not be the case of 1TD or AVG method.

Indeed the central challenge of in vivo cardiac DTI is the management of physiological motion. While some approaches have used dedicated MRI sequences to compensate for physiological motion (Tseng et al. 2000; Gamper et al. 2007), our approach differs from these in that it uses DW sequences available on clinical scanners and acquires data over multiple shifted TD acquisitions in diastole. Our results showed that signal loss due to cardiac motion can be, to some extent, overcome by the combined use of a dedicated acquisition method and adequate post-processing based on image registration and PCATMIP. Our study showed that PCATMIP permitted the recovery of DW signal intensities: minimizing spatially dependent signal loss observed at the multiple shifted diastolic acquisitions while also preserving directional diffusion information.

Image registration is of course mandatory to correct for interscans motion. Co-registration is by design only capable of correcting for in-plane motion and cannot compensate for larger through-plane motion, although it may appear to partially compensate. However, due to the existence of some through-plane motion, residual motion artifacts remained. Spatially variable through-plane motion will make spatially fresh magnetization enter the slice which results in a loss of coherence of tensor fields between slices. While the streamline-based tracking technique is the most commonly used in the human heart tractography studies and it appears to give excellent results if the principal eigenvector field is smooth and the fibers are strongly oriented along a certain direction. We should note that the tensor field is error prone in the sense that the residual motion of the DTI data would influence the direction of the principal eigenvector (Lazar et al. 2003). The streamline tracking by integrating the principle eigenvector from the tensor fields would result in an erroneous fiber structure. We can observe that the 3D fibers in Fig. 4.7 are sometimes discontinuous in some part of the LV, because the principal eigenvectors in these regions are so incoherent or sparse that it is very difficult to track the fibers correctly.

The DW images obtained by the 1TD method for the volunteers revealed spatially and temporally motion-induced signal loss. The hypothesis is that signal loss from imperfect 1TD acquisition could be compensated using the multiple shifted acquisition method combined with the PCATMIP post-processing. The PCATMIP post-processing over multiple shifted acquisitions clearly seems to preserve the directional diffusion information in the images and recover the helical fiber architecture of the heart.

The b value of 200 s/mm^2 was selected based on that it was sufficient to reveal the diffusion anisotropy in the myocardium. Larger b value decrease SNR and will induce much larger signal loss. Although with this lower b value, it is sufficient to extract the diffusion information to calculate helical fiber tracts and fiber architecture parameters. However, a

systematic study to define the optimal b value used in in vivo cardiac DTI is required and will be the subject of future work.

In this study, the mean global FA value obtained with PCATMIP (0.41 ± 0.09) was lower than the FA (about 0.6) reported by previous study (Nielles-Vallespin et al. 2012) in healthy volunteers at 3T scanner. At the same time, the mean global MD value obtained with PCATMIP (0.80 ± 0.2 $\times 10^{-3}$ mm2/s) was also smaller than MD (0.9 ± 0.3 $\times 10^{-3}$ mm^2/s) reported by previous study (Reese et al. 1995) and MD (1.0 $\times 10^{-3}$ mm^2/s) reported in (Nielles-Vallespin et al. 2012). It should be noted that the quantitative results in this study were related to the acquisitions at end diastole. We may consider differences between the data acquired at different cardiac phases. Indeed, even though not well understood yet, the myofiber re-organization of the fiber architecture in the human heart is dynamic during cardiac cycle and is related with the myocardial strain.

1TD or AVG method yielded a fiber architecture that is not consistent with the state of the art knowledge from histological and ex vivo DTI studies. While the HA range obtained from PCATMIP method in this study is coherent with previously published in vivo data (McGill et al. 2012; Nielles-Vallespin et al. 2012), although it is slightly narrower (approximately from 41° on the endocardium to -34° on the epicardium) than previously-reported ex vivo human cardiac studies (Greenbaum et al. 1981; Lombaert et al. 2012). The study reported by Lombaert et al. (Lombaert et al. 2012) of healthy ex vivo human hearts showed ranges of HA variations from $66^\circ \pm 15^\circ$ on the endocardium to $-41^\circ \pm 26^\circ$ on the epicardium. The distribution of HA of the histological study [Greenbaum *et al.*, 1981] of postmortem human heart varies from about 40° on the endocardium to about -40° on the epicardium. The study reported in (Nielles-Vallespin et al. 2012) of healthy in vivo human hearts showed ranges of HA variations from $22^\circ \pm 10^\circ$ on the endocardium to $-17^\circ \pm 6^\circ$ on the epicardium for breath-hold study; from $7^\circ \pm 7^\circ$ on the endocardium to $-14^\circ \pm 6^\circ$ on the epicardium for navigated acquisition free-breathing study. The study (McGill et al. 2012) showed that HA was about $39^\circ \pm 8^\circ$ on the endocardium and $-34^\circ \pm 8^\circ$ on the epicardium in patients. We need to consider many factors that may influence the HA range, i.e., in vivo and ex vivo data, data acquired at different cardiac phases, spatial resolution, motion artifacts and the used segmentation method. The narrower HA range may be caused by signal loss in the DW images due to residual motion and noise. Another possible cause of such narrower angle range may be related to the fact that the angles were obtained by averaging the coarser in-plane resolution voxels inside transmural layers. Since coarser resolution neighboring voxels have greater angle difference, the obtained angle has a smaller value after averaging.

This preliminary experiments show that the approach proposed in this paper (dedicated acquisition method combined with image registration and PCATMIP) has the potential to provide in vivo structure of the normal heart. Although seduced by its workflow for further integration in clinical trial protocol aiming at screening human cardiovascular disease in patients, it still has to demonstrate its accuracy and reproducibility.

The acquisition of multiple TD dataset leads to a total scan time of about 25 minutes for each volunteer, which is an acceptable acquisition time scale for clinical application. The approach presented here is easy to implement, does not require a reliable navigator

synchronization or RR interval. Therefore, its workflow is very suitable for the low patient compliance observed in clinical routine.

4.6 CONCLUSION

We have investigated in vivo cardiac DTI on healthy volunteers with free-breathing. To our best knowledge, this is the first reconstruction of whole human heart fiber architecture with free-breathing acquisitions. The combination of dedicated acquisition method, image registration and PCATMIP technique makes it possible to reconstruct myocardial fiber architecture. The obtained HA maps indicate myocardial fiber orientation of the LV which shows a circularly symmetric pattern, from about 41° on the endocardium to -34° on the epicardium. The 3D fiber architecture reproduces the typical helical organization known from in vivo and ex vivo human heart studies. Further use of the proposed in vivo cardiac DTI with free-breathing has the potentiality to become a powerful tool for studying the impact of cardiovascular disease on the fiber architecture in patients.

Chapter 5

Improved whole heart free-breathing in vivo cardiac DTI using wavelet-based image fusion (WIF) method

Contents

Abstract

The purpose of this chapter was to further study in vivo cardiac fiber architectures of the human heart by investigating a second method addressing motion problem - a wavelet-based image fusion (WIF) algorithm and a PCA noise removing method. In this framework, a comparison of DTI measurements between the PCATMIP and WIF methods is also performed; the tensor fields are calculated, from which the in vivo fiber architecture properties are derived and compared. Meanwhile, the 3D cardiac fiber architectures are reconstructed using the two methods. The comparison of FA values ($FA_{PCATMIP} = 0.45 \pm 0.10$, $FA_{WIF} = 0.42 \pm 0.05$, $P=0.063$) showed no significant difference, while MD values ($MD_{PCATMIP} = 0.83 \pm 0.12 \times 10^{-3}$ mm^2/s, $MD_{WIF} = 0.74 \pm 0.05 \times 10^{-3}$ mm^2/s, $P<0.05$) were significantly different. The myocardial fiber orientation of the LV is from -34° on the epicardium and to 41° on the endocardium for PCATMIP, and from -38° to 44° for WIF method. This is the first comparative study between different in vivo DTI methods on the same entire heart of healthy volunteers. By comparing the tensor fields and 3D fiber tracts, the better results are observed with the WIF method in comparison with the PCATMIP method.

Résumé en français

Le but de cette étude était de réaliser une étude plus approfondie de l'architecture de fibres in vivo du cœur humain en développant une deuxième méthode de correction du mouvement par l'utilisation d'un algorithme de fusion d'images basé sur l'ondelette (wavelet-based image fusion—WIF) et d'une technique de débruitage PCA. Dans ce cadre, une comparaison des mesures DTI entre la méthode PCATMIP et la méthode WIF est réalisée; les champs de tenseurs sont calculés, à partir desquels les propriétés de l'architecture des fibres in vivo sont comparées. En même temps, les architectures des fibres cardiaques 3D ont été reconstruites en utilisant les deux méthodes. La comparaison des valeurs FA ($FA_{PCATMIP}$ = 0.45 ± 0.10, FA_{WIF} = 0.42 ± 0.05, P=0.063) n'a pas montré de différence significative, tandis que les valeurs MD ($MD_{PCATMIP}$ = 0.83 ± 0.12 $\times 10^{-3}$ mm^2/s, MD_{WIF} = 0.74 ± 0.05 $\times 10^{-3}$ mm^2/s, P<0.05) étaient significativement différents. L'orientation des fibres du LV est de -34° sur l'épicarde et à 41° sur l'endocarde pour la méthode PCATMIP, et de -38° à 44° pour la méthode WIF. C'est la première étude comparative entre différentes méthodes de DTI cardiaque in vivo chez des volontaires sains. En comparant les champs de tenseurs et les architectures de fibres, la méthode WIF fournit de meilleurs résultats que PCATMIP.

5.1 Introduciton

Due to time constraints for the in vivo cardiac diffusion data acquisitions, the number of slices acquired is also very limited. It is therefore interesting to acquire a higher number of slices within an acceptable scan time and benefit from more slices to describe 3D myocardial fiber architectures.

The purpose of this study was to perform a quantitative investigation of in vivo cardiac fiber architectures of the human heart under free-breathing conditions. Recently, a robust multiple shifted acquisition method was proposed (Pai et al. 2010) to cope with human motion problem in cardiac DW imaging, which involves multiple-time-point DW images acquisitions in diastole of the cardiac cycle. The signal loss from one single phase acquisition could be compensated for during the next phase acquisition by repeating the sequence. In this work, we applied this special acquisition method to free-breathing DTI acquisition of the human heart. For that purpose, acquisition of DW images in 12 gradient directions was first performed; for each direction, 10 phase DW images corresponding to 10 time points during end diastole were acquired. We firstly applied a non-rigid registration (Vercauteren et al. 2009) to the datasets, and then the wavelet-based fusion approach was performed to the registered multiple-time-point DW images. At last, an effective method based on principal component analysis (PCA) with pixel grouping (Zhang et al. 2010) as a filter was employed to remove the noise. The final corrected DW images were then used to calculate the tensor fields, from which FA, MD, HA maps, and 3D fiber tracts were derived.

5.2 Material and method

5.2.1 Registration using Log-domain Diffeomorphic Demons

In this improved processing method, we use a symmetric Log-domain Diffeomorphic Demons (LDDD) [Vercauteren *et al.*, 2009]. The transformation ϕ is a function of the velocity field υ, such that $\phi = \exp(\upsilon)$. Thus, the LDDD algorithm can be formulated as a alternate optimization scheme of the following energy with respect to the velocity fields υ_c (hidden variable) and υ:

$$E(I_{ref}, I_{flo,}, v, v_c) = \frac{1}{\sigma_i^2}\left\|I_{ref} - I_{flo} \circ \exp(v_c)\right\|^2 + \frac{1}{\sigma_x^2}\left\|\log(\exp(-v) \circ \exp(-v_c))\right\|^2 + \frac{1}{\sigma_T^2}\left\|\nabla v\right\|^2, \quad (5.1)$$

where $\sigma_{i,x,T}$ are penalizing terms, I_{ref}, a reference image, I_{flo}, a floating image, υ, the velocity field such that $I_{flo} \circ \exp(v_c) \equiv I_{ref}$, and the velocity field υ_c, a hidden variable whose exponential is called the correspondence. The optimization of this energy is implemented in [Vercauteren *et al.*, 2009] with two consecutive smoothing steps which use two parameters. Both are widths of smmothing kernels, one for the smoothing of the update field, $\sigma_{K_{fluid}}$ =1.4,

and has a fluid behavior, and the second is for the smoothing of the displacement field, $\sigma_{K_{diff}}$ =1.0, and has an elastic behavior.

5.2.2 **State of the art of wavelet-based image fusion methods**

The wavelet transform is a mathematical tool that can detect local features in a signal process. It also can be used to decompose two-dimensional (2D) signals such as 2D gray-scale image signals into different resolution levels for multiresolution analysis. Wavelet transform has been used in many areas, such as texture analysis, data compression, feature detection, and image fusion. In this section, we briefly review and analyze the wavelet-based image fusion technique. Wavelet fusion techniques (Yang et al. 2010) are commonly used to combine multiple images into a single one, retaining important features from each, and providing a more accurate description of the object. At present, there are three major types of fusion operators: pixel level (Piella 2003), area level (Gunatilaka & Baertlein 2001), and region level (Goshtasby et al. 2007). 1) The pixel fusion rules directly decide the fused pixels according to a single pixel value in the corresponding position of each source image after transformation. This usually uses the pixel (or pixel absolute value) larger (or smaller), pixel weighted average method. As it is easy to realize and it is fast, it used to be widely used in every fusion area. However, it does not consider the correlation between adjacent pixels. 2) The area fusion rules, also called window fusion rules, decide the fused coefficient according to the relative position of the local windows. As it not only considers the source image (or the sub-band image) gray value, but it also considers the neighboring gray level value, it can reduce the sensitivity to the edge, and thus can get better vision characteristics. 3) Region rules are commonly used in the transform domain. The fusion measurement index often uses energy in the area of the image transform coefficient because the local characteristics of the images are often not expressed by a single pixel or local window, but by local area. So the regional fusion rules can be better than the former but with the computational cost. In the actual utilization process, the three fusion operators can mutually penetrate. Yang et al. (Yang et al. 2010) proposed an effective wavelet-based approach to fuse medical images. They used the Daubechies's db8 with a decomposition level of 3. Then they proposed a different fusion scheme for combining the coefficients: coefficients in low-frequency band are selected with a visibility-based scheme, and coefficients in high frequency bands are selected with a variance based method. Tian et al. (Tian et al. 2011) proposed an adaptive multi-focus image fusion using a wavelet-based statistical sharpness measure to combine a set of images that are captured from the same scene but with different focuses. In their studies, the local content information of the input images is evaluated. The different marginal distributions of the wavelet coefficients are observed for images with different focus levels. Then the wavelet coefficients distribution is evaluated using a locally adaptive Lapalcian mixture model. In their studies, the images are applied by a two level wavelet decomposition using a Daubechies's wavetlet with eight vanishing moments. Recently, Aganj et al. (Aganj et al. 2012) proposed a 3D wavelet fusion approach for the reconstruction of isotropic resolution MR images from orthogonal anisotropic-resolution scans. They transformed the input image

into two distinguishable parts and then selectively extract information from the input images by using the Haar wavelet basis.

5.2.3 **WIF processing scheme**

In our case, ideally, we would like to collect all the meaningful diffusion information from the input images (multiple TDs), while discarding the parts strongly affected by the bulk motion. In this subsection, to understand the concept and procedure of the WIF approach, a schematic diagram is first given in Fig 5.1. In general, the basic idea of image fusion based on wavelet transform is to perform the multiple scale decomposition on each source image; the coefficients of both the low-frequency band and high-frequency bands arethen fused with a certain pixel-level fusion rule at each scale. The most important is to combine the wavelet coefficients. As seen from Fig 5.2, the high-frequency bands distribution is different for the images with different motion effects levels. More specifically, the spreading of the wavelet coefficients distribution of the more motion-influenced image is narrower than that of a less motion influenced image. That is to say, the image with more motion effects yields more wavelet coefficients that are close to zero and less wavelet coefficient with large magnitudes, compared to images less influenced by motion. This motivates us to propose a fusion rule for high-frequency bands: we only select the information from the high-frequency band which yields wider spreading wavelet coefficients distribution. More specifically, for the coefficient to be chosen at the location k, we set a N×N (N=5) window centered on it for the local coefficients statistics. The high-frequency coefficients of the fused image (denoted as $C_F^H(k)$) is produced by combining those of the two source images (denoted as $C_A^H(k)$ and $C_B^H(k)$) as

$$C_F^H(k) = \begin{cases} C_A^H(k) \ \textit{if} \ \sigma_A(k) \geq \sigma_B(k), \\ C_B^H(k) \qquad \textit{otherwise}, \end{cases} \tag{5.2}$$

where $\sigma_A(k)$ and $\sigma_B(k)$ are the standard deviations (SD) of the high-frequency coefficients in the window of the two input images, respectively. The low-frequency wavelet coefficient reflects the global information of the entire images. Normally the signal loss is regional in DW image and the low-frequency coefficient does not fluctuate too much. However, at some TDs, the motion greatly induces the signal loss across the entire heart and the low-frequency coefficient will decrease. The low-frequency band represents the signal magnitude of the images. Therefore, for low-frequency bands, the largest absolute wavelet coefficient was selected at each pixel location from the source images to cope with the signal loss. By picking the coefficients pixel by pixel according to the fusion rule, we can obtain the combined wavelet coefficient. Then the fused image is obtained by performing the inverse wavelet transform from the combined wavelet coefficients. Therefore, as shown in Fig 5.1, the detailed fusion steps can be summarized as follows.

Step 1: The multiple TD DW images are decomposed into wavelet-transformed images, respectively, based on wavelet transformation. Each DW image is applied by a two-level wavelet decomposition using a Daubechies's wavelet with eight vanishing moments, which has been widely used in image fusion by many researchers (Yang et al. 2010; Tian et al.

2011). We may use other wavelet transforms, the different high frequency bands of the different wavelet transforms are shown in the discussion part. The transformed images with two-level decomposition will include one low-frequency portion (low-low band) and 6 high-frequency portions (low-high bands, high-low bands, and high-high bands).

Step 2: The transform coefficients of different bands are fused with the proposed fusion rule.

Step 3: The fused image is constructed by applying the inverse wavelet transform on the fused wavelet coefficients from Step 2.

Step 4: If there are more than two input images, they are combined one by one by iteratively applying the above steps 1-3.

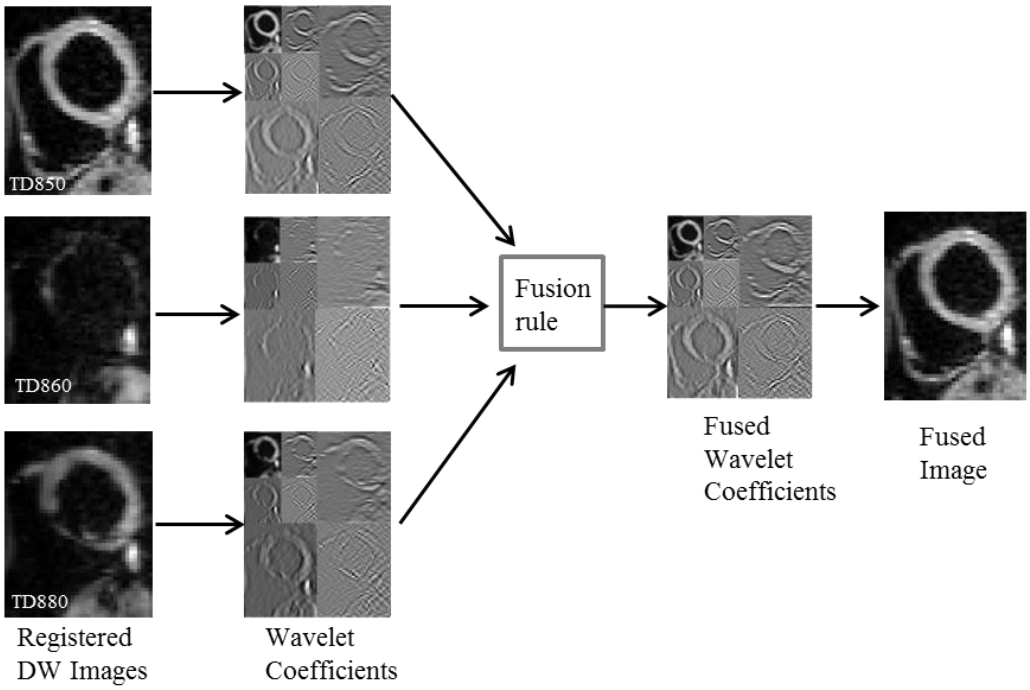

Fig. 5.1. The DW images fusion scheme using the wavelet transform in 2-level decomposition.

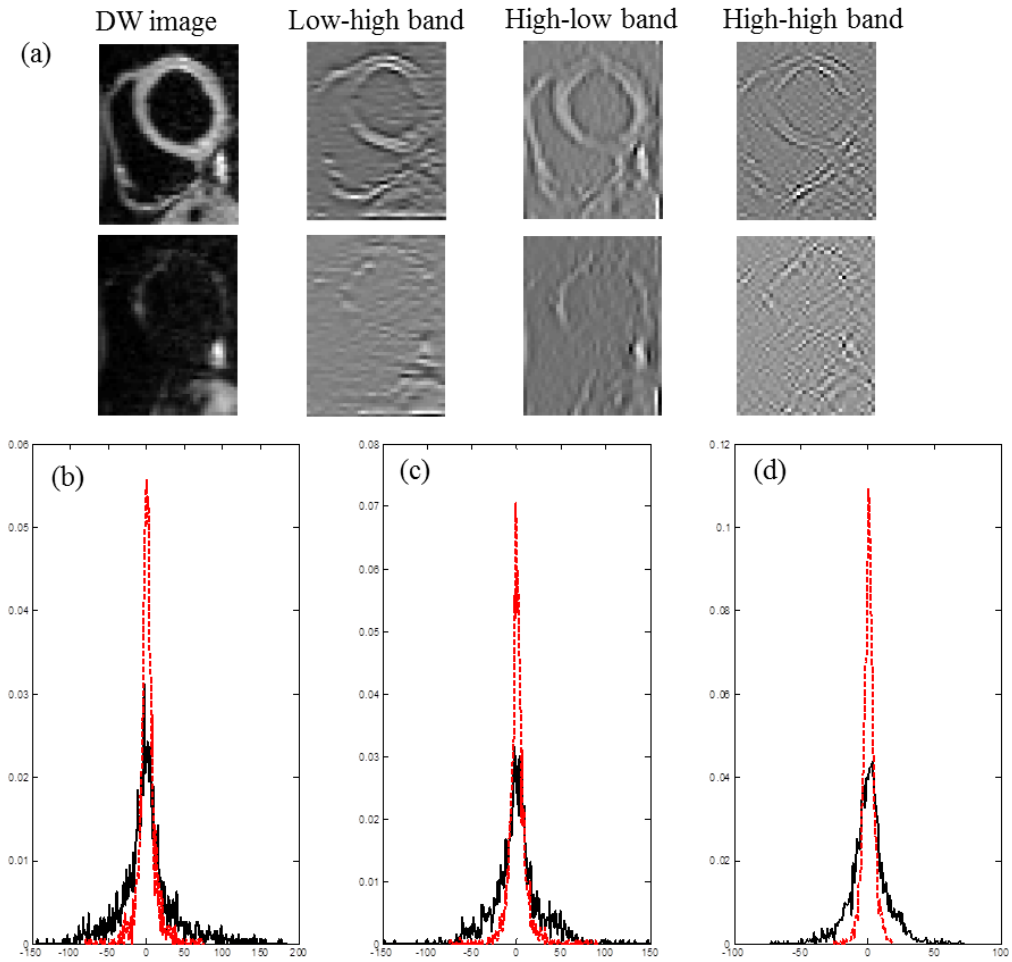

Fig. 5.2. The high-frequency hand distribution of the wavelet coefficients is different for DW images with different motion effects: (a) two TD images with their high-frequency hands, where the top row image is acquired with less motion and the bottom row image is acquired with great motion effects; (b)-(d) the histograms of wavelet coefficients of the image less influenced by motion (black line) and that of the image greatly influenced by motion (red line), respectively. (b) Low-high band; (c) high-low band; (d) high-High band.

5.2.4 **Denoising of DW images using PCA**

In vivo cardiac DTI is highly susceptible to noise. The noise, primarily at the level of DW images, can produce errors in the subsequent calculations of diffusion parameters. For the wavelet-based image fusion, not only the useful diffusion information but also the noise in the image was involved during the transformation. So removing the noise is crucial for practical utility of DTI in human hearts. We used a denoising method based on PCA with LPG approach (Zhang et al. 2010). For an underlying pixel to be denoised, we set a K×K window centered on it and denote all the pixels in the window as its nearest neighbors. The pixel and its nearest neighbors are modeled as a vector variable. Then we use anther L×L window centered on the pixel as a training block to find the training samples. In this way, there are

totally $(L-K+1)^2$ training samples for each pixel. However, there can be very different blocks from the given central K×K block in the L×L training window so that taking all the K×K blocks as the training samples will lead to inaccurate estimation of the PCA transformation matrix. Therefore, selecting the training samples that are similar to the central K×K block is necessary. Such selecting and grouping procedure guarantees that only the sample blocks with similar contents are used in the local statistics calculation for PCA transform estimation, so that the image local feature can be well preserved after coefficient shrinkage in the PCA domain to remove the noise.

We denote by $\vec{x}_0^v$ the column sample vector containing the pixels in the central block and denote by $\vec{x}_i^v$, i= 1,2 …, $(L-K+1)^2$-1, the sample vectors in the training block. Then it can be easily calculated that $e_i = \frac{1}{m}\sum_{k=1}^{m}(\vec{x}_0^v(k) - \vec{x}_i^v(k))^2$. We select $\vec{x}_i^v$ as a sample vector of $\mathbf{x}_v$ if e_i <T, where T is a preset threshold. We denote these sample vector as $\vec{x}_0^v, \vec{x}_1^v, \ldots, \vec{x}_{n-1}^v$. The training dataset for $\mathbf{x}_v$ is formed by

$$\mathbf{X}_v=[\vec{x}_0^v \vec{x}_1^v \ldots \vec{x}_{n-1}^v], \tag{5.2}$$

Suppose we select n sample vectors of $\mathbf{X}_v$. To make sure there are enough samples for computing the PCA transformation matrix, n could not be too small. In practice, we will use at least N·m training samples of $\mathbf{x}_v$ in denoising, where constant N=8~10. Usually, the N·m matched samples are robust to estimate the image local statistics, and they are enough to calculate the PCA transformation matrix.

Such selecting procedure guarantees that only the sample blocks with similar contents are used in the local statistics calculation for PCA transform estimation, so that the image local feature can be well preserved after coefficient compression in the PCA domain. In this study, we set K=5 as the central block and L=41 (which are the same as that used in (Zhang et al. 2010)) as the training block for the denoising procedure. Now the problem is how to estimate the noiseless dataset $\mathbf{X}$ from the noisy measurement $\mathbf{X}_v$. In the m×n dataset matrix $\mathbf{X}_v$ of Equation (5.2), it can be rewritten as

$$\mathbf{X} = [\overrightarrow{X_1}^T \overrightarrow{X_2}^T \ldots \overrightarrow{X_m}^T]^T, \tag{5.3}$$

where $\overrightarrow{X_i} = [x_i^0 x_i^1 \ldots x_i^{n-1}]$ is the *i*th row of the sample matrix $\mathbf{X}$. Then the covariance matrix is calculated as

$$\boldsymbol{\Omega} = \frac{1}{\mathrm{n}} XX^T. \tag{5.4}$$

The goal of PCA transform is to find an orthonormal transformation matrix $\mathbf{P}$ to decorrelate $\mathbf{X}$, i.e. $\mathbf{Y}=\mathbf{PX}$ so that the covariance matrix of $\mathbf{Y}$ is diagonal. Since the covariance matrix $\boldsymbol{\Omega}$ is symmetrical, it can be written as

$$\boldsymbol{\Omega} = \boldsymbol{\phi}\Lambda\boldsymbol{\phi}^T, \tag{5.5}$$

where $\boldsymbol{\phi} = [\phi_1 \phi_2 \ldots \phi_m]$ is the m×m orthonormal eigenvector matrix and $\Lambda = diag\{\lambda_1, \lambda_2, \ldots, \lambda_m\}$ is the diagonal eigenvalue matrix with $\lambda_1 \geq \lambda_2 \ldots \geq \lambda_m$. The terms $\phi_1, \phi_2, \ldots, \phi_m$ and $\lambda_1, \lambda_2, \ldots, \lambda_m$ are the eigenvectors and eigenvalues of $\boldsymbol{\Omega}$. By setting $\mathbf{P} = \boldsymbol{\phi}^T$, $\mathbf{X}$ can be decorrelated, i.e. $\mathbf{Y}=\mathbf{PX}$ and the convariance matrix of $\mathbf{Y}_v$ is

$$\boldsymbol{\Omega} = \frac{1}{\mathrm{n}} YY^T = \boldsymbol{\phi}\Lambda\boldsymbol{\phi}^T. \tag{5.6}$$

In the PCA transform domain, most energy of the noiseless dataset $\mathbf{Y}$ concentrates on the several most important compenents, while the energy of noise distributes much more evenly.

By removing the smaller eigenvalues in the diagonal eigenvalue matrix, and transform **Y** back to the spatial domain, we obtain the denoised results, as $\mathbf{X}=\mathbf{P}^{-1}\mathbf{Y}$. Applying the above procedure to each pixel leads to the full-denoised image.

5.2.5 Interpolation of diffusion tensors

Diffusion tensor interpolation is an important issue in the application of DTI to the human heart. Due to the low spatial resolution if the in vivo DW images, to improve the tensor resolution, the diffusion tensors were interpolated in the plane by a factor of two using the Log-Euclidean method, which avoids swelling effects. The resoluiotn of the interpolated tensor filed is improved (Fig. 5.3 and Fig. 5.4). The same effects can be seen from the 3D fiber tracts in Fig. 5.5.

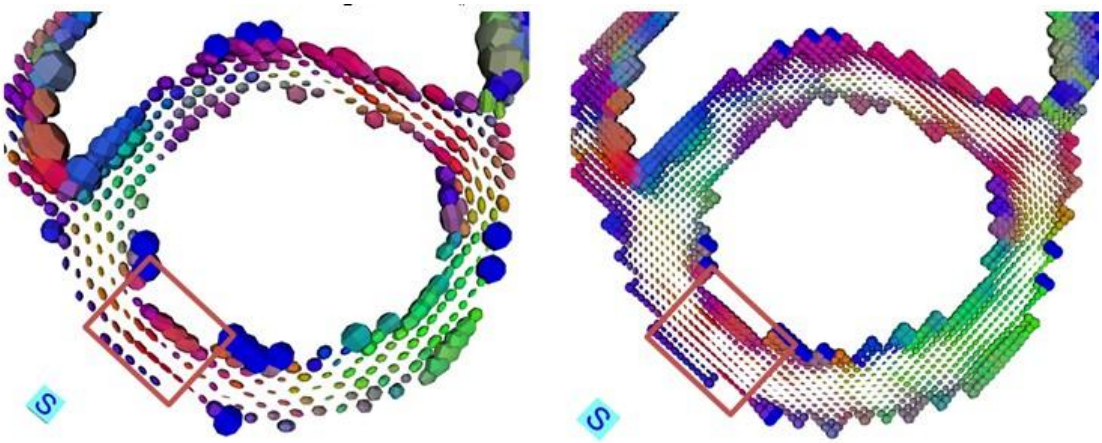

Fig. 5.3. Examples of tensor fields before (left) and after (right) the interpolation.

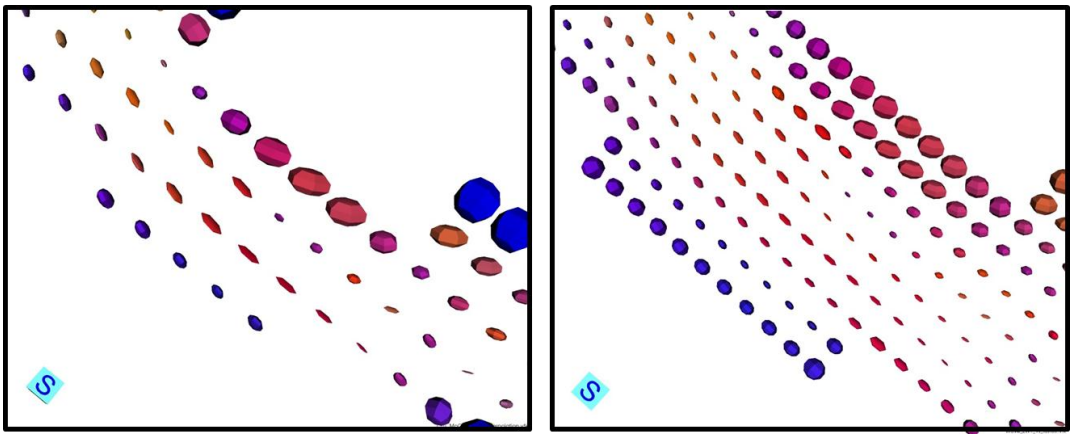

Fig. 5.4. Examples of tensor fields before (left) and after (right) the interpolation by zooming the ROI located in Fig. 5.3.

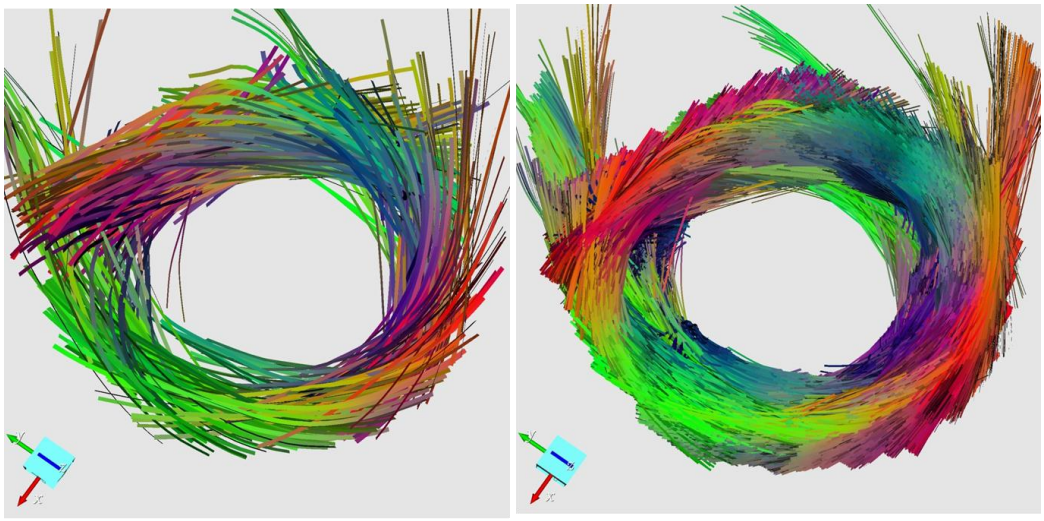

Fig. 5.5. Examples of 3D fiber tracts before (left) and after (right) the interpolation.

5.2.6 **Quantification of diffusion parameters**

A cardiac DTI post-processing program was built in house using MATLAB (R2010b, the Mathworks, Inc, Natick, MA, USA). 3D fiber tracts were constructed by integrating the principal eigenvector from the diffusion tensor fields using streamline algorithm. The criteria for stopping the tracking are: a lower-threshold of 0.05 on FA and a minimum fiber length of less than 20 voxels. 3D tensors were then visualized with cylinder glyphs.

5.3 Results using WIF method

Fig. 5.6 shows an example of in vivo cardiac DW images of a volunteer acquired near the heart base. Even though the acquisition windows were positioned at minimal in-plane and through-plane heart motion of the LV, intensity fluctuations arising due to residual heart and respiratory motion can be seen during free-breathing acquisitions. Fig. 5.6 (a) presents registered DW images of the 10 TD acquisitions of one diffusion gradient direction. The signal loss throughout the myocardium is visible. Fig. 5.6 (b) shows the fused DW image by applying wavelet-based fusion method to the 10 TD DW images. Fig. 5.6 (c) shows corrected DW images recovered from the raw images in 12 diffusion gradient directions and b0 image using fusion and denoising methods. The motion artifact contamination rate and noise was reduced, further improved the SNR.

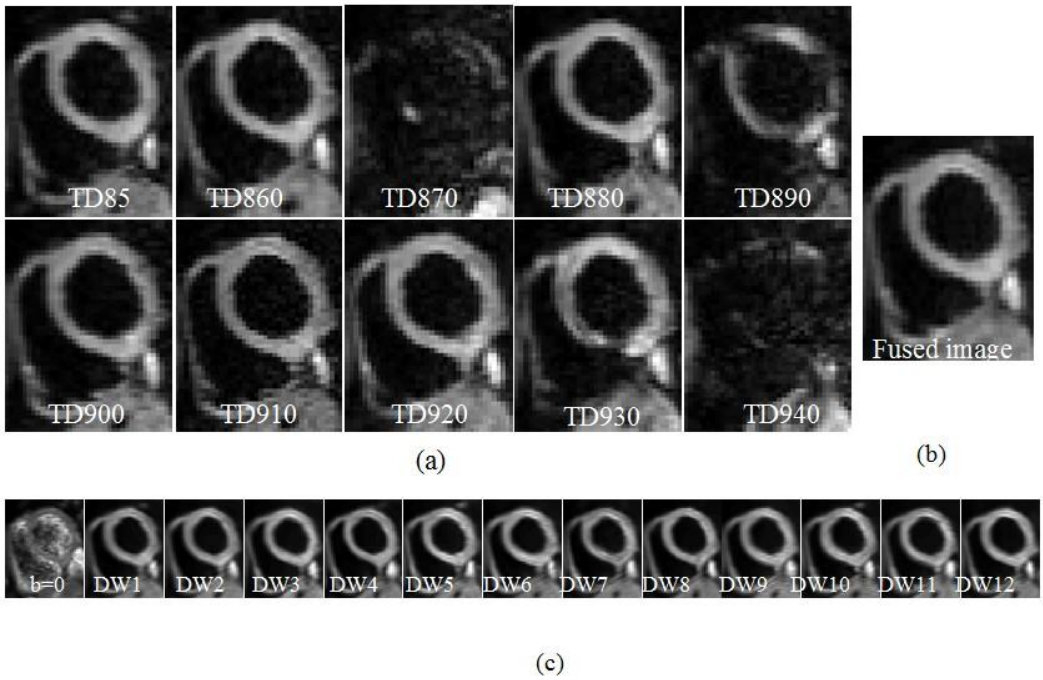

Fig. 5.6. (a) Free-breathing short-axis DW images resulting from one diffusion prepared acquisition performed at 10 TDs in diastole on a volunteer. Visible spatial signal intensity fluctuation resulting from spatially variable intrascan motion. (b) Corresponding processed DW images using wavelet-based image fusion. (c) DW images corresponding to 12 diffusion gradient directions as well as b0 image were fused using wavelet transformation.

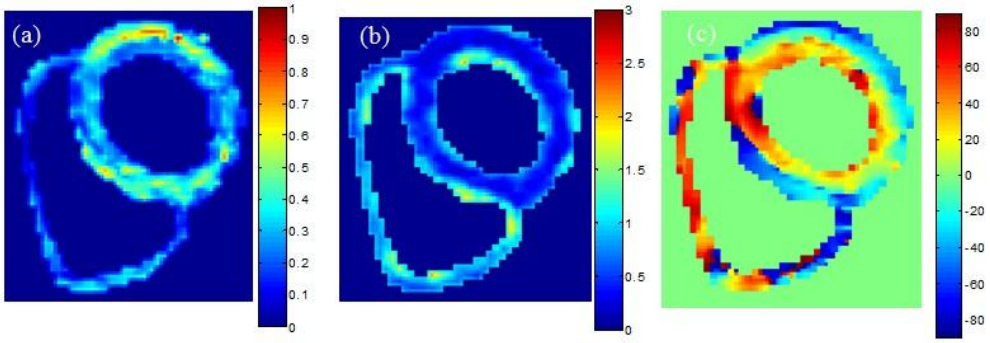

Fig. 5.7. FA, MD, and HA maps calculated from a volunteer.

Fig. 5.7 (a) and (b) illustrate FA and MD maps of a volunteer, respectively. The mean ± SD of FA and MD values in the LVs of all the volunteers are summarized in Figure 4. Both FA and MD values were defined as the mean values over the 10 slices of each subject. The FA values were 0.369 ± 0.017, 0.373 ± 0.020, 0.476 ± 0.019, 0.461 ± 0.043, 0.393 ± 0.012, 0.437 ± 0.03 for each volunteer. The MD values are $0.714 \pm 0.041 \times 10^{-3}mm^2/s$, $0.687 \pm 0.060 \times 10^{-3}mm^2/s$, $0.783 \pm 0.057 \times 10^{-3}mm^2/s$, $0.775 \pm 0.059 \times 10^{-3}mm^2/s$, $0.759 \pm 0.054 \times 10^{-3}mm^2/s$,

$0.737 \pm 0.050 \times 10^{-3}mm^2/s$ for each volunteer. The mean values over the 6 subjects are 0.419 ± 0.045 and $0.742 \pm 0.050 \times 10^{-3}mm^2/s$ for FA and MD, respectively.

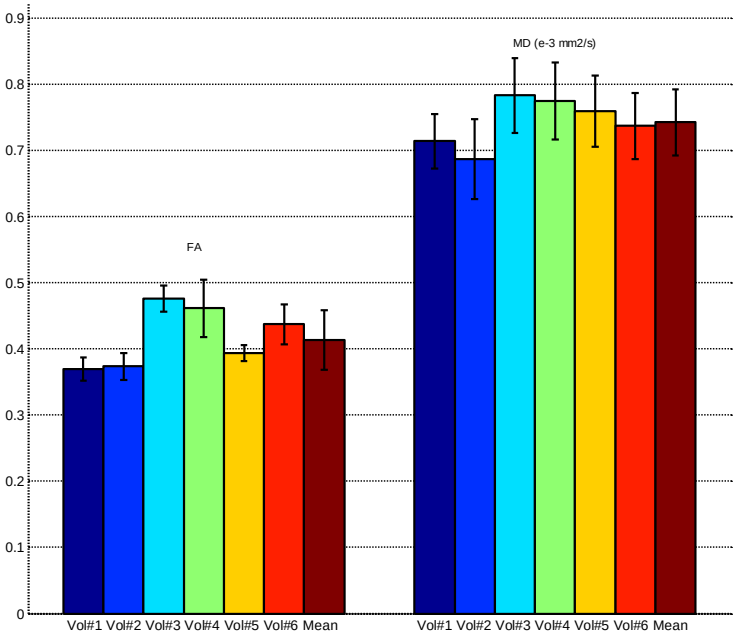

Fig. 5.8. Mean ± SD FA and MD values in the LVs of all the volunteers and mean over the 6 volunteers.

Fig. 5.7 (c) shows the HA map of a volunteer. The mean HA values for all the volunteers range from 35.3° ± 9.0° in the endocardial layer, through 20.0° ± 6.3° in the mid-endocardial layer, 2.4° ± 7.3° in the mid-wall layer and -14.6° ± 5.9° in the mid-epicardial layer, to -31.4° ± 7.5° in the epicardial layer in Fig. 5.9(b). The transmural course of the HA appears to be linear from endocardium to epicardium. Endocardial fiber orientations were assigned a positive angle and epicardial fiber orientations a negative angle, as originally described by Streeter (Streeter et al. 1969) with zero angle being aligned with the local circumferential direction.

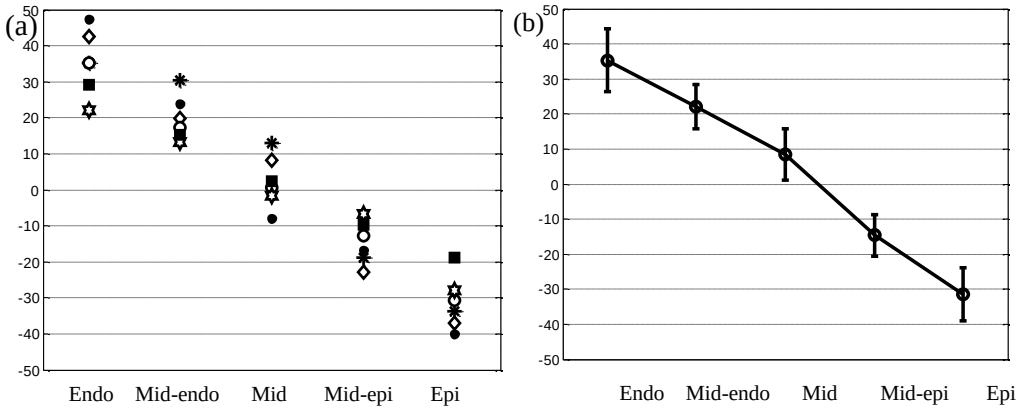

Fig. 5.9. HA in the LV. (a) Plot of HA values for each volunteer. (b) Mean ± SD of HA values over all volunteers.

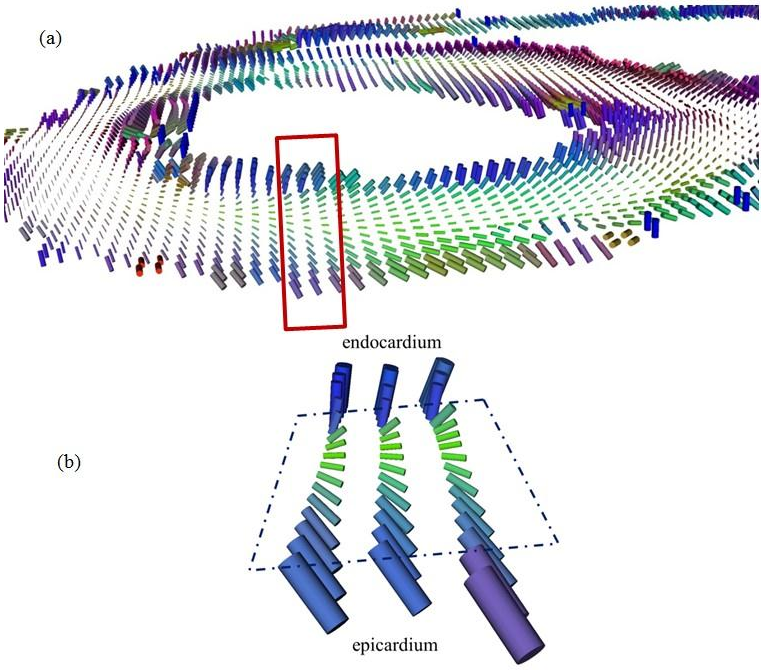

Fig. 5.10. Tensor fields of a volunteer. (a) Fiber orientation of LV seen from lateral wall. (b) Tensor fiber zoomed from the ROI located at lateral wall in (a). The helical pattern of the cardiac fiber is clearly depicted by the principal direction of the cylinders glyph. Color indicates the local orientation of the fiber.

Fig. 5.10 illustrates the tensor fields from lateral wall view. The orientation of the cylinder glyphs is determinated by the primary eigenvector and the shapes are parameterized by the eigenvalues and eigenvectors. The continuous variation in a circular sense of fiber angles inside the LV wall was observed in Fig. 5.10 (a). The fiber angles vary with the curvature of the LV and rotate with a smooth progression from one color to the other when turning around the LV. This variation of fiber angles reflects the spiral-shaped muscle structure of the heart. The transmural variation was visible in the LV in Fig. 5.10 (b). The orientations of the fiber angle show clearly distributions of positive angles on the endocardium and of negative angles on the epicardium. The values for the mid-wall show distributions about zero. The rotation of the fiber angle was clearly seen between the endocardium and epicardium.

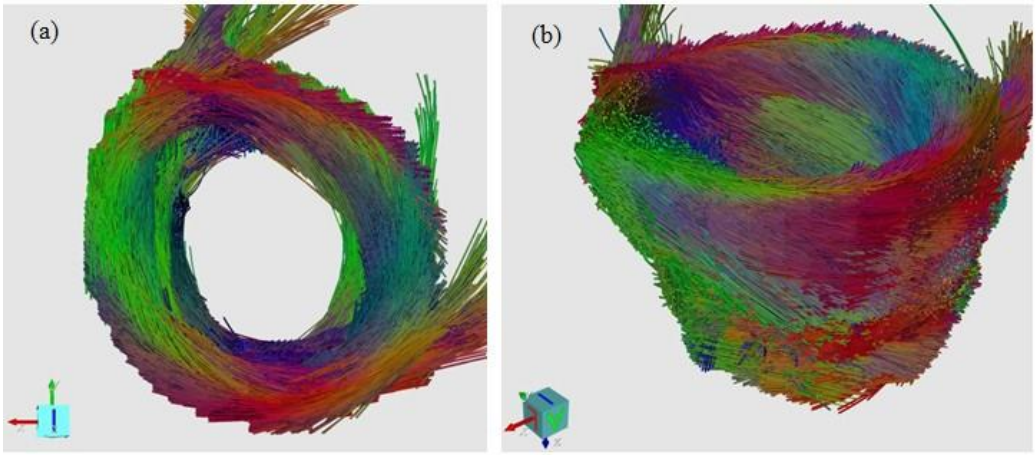

Fig. 5.11. The 3D fiber tracts of a volunteer. (a) Short-axis view from the heart base. (b) Longitudinal view from lateral wall. The r, g, b colors of the fibers indicate the x, y, z components of the local orientation of the fiber, respectively.

3D views of typical fiber tracts derived from the DTI data are shown in Fig. 5.11. The 3D fiber tracts provide a representation of the cardiac fiber architecture as well as its variability in terms of fiber orientations. The color of the fibers is determinate by the primary eigenvector.

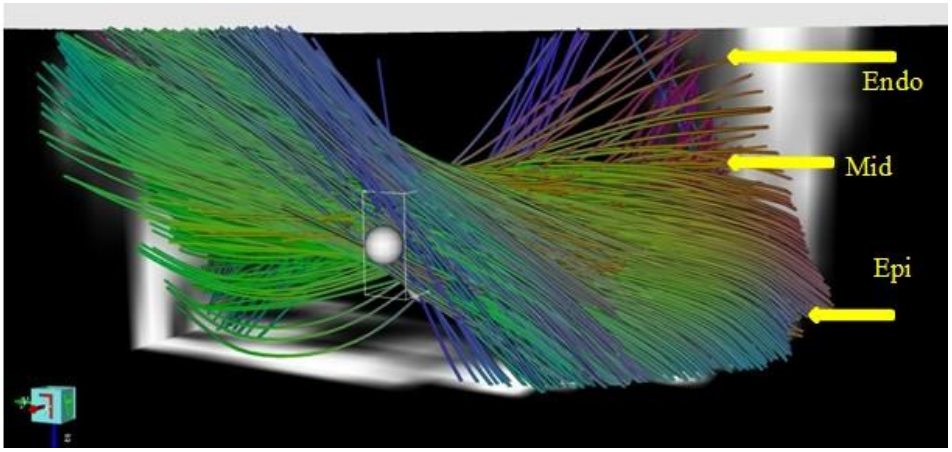

Fig. 5.12. Cardiac fiber architecture of a volunteer viewed more finely from part of the fiber located at the lateral wall. Fiber tracts have positive angles in the endocardium and negative angles in the epicardium. The fiber tracts in the mid-myocardium have nearly zero angles.

For better depiction of the helical structure, a shutter located at the lateral wall viewed from the epicardial surfaces was shown in Fig. 5.12 and Fig. 5.13. Through the myocardium a evolution in myofiber angle was seen, confirming what was observed in the visualization of the helix angle in Fig. 5.7(c) and of tensor field in Fig. 5.10(b).

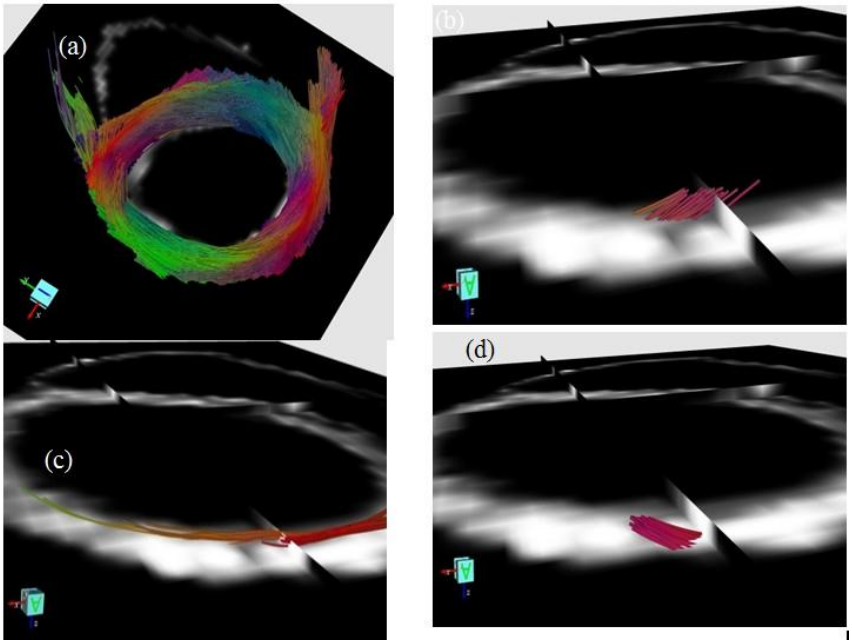

Fig. 5.13 Myofiber architecture from DTI data on a healthy volunteer viewed more finely at different locations of cardiac wall. (a) Viewed from short-axis; (b) viewed in the endocardium; (c) viewed in the mid-wall; (d) viewed in the epicardium.

5.4 Comparison diffusion parameters of PCATMIP and WIF method

Fig. 5.14 shows the FA and MD maps obtained using PCATMIP and Wavelet-based fusion method. Fig. 5.15 show the FA and MD values compared between the two methods. The FA and MD values were defined by averaging over all the slices and over all the volunteers. and the results show that there is no difference for the FA ($P>0.005$). But there is significant difference for the MD with $P = 0.026$.

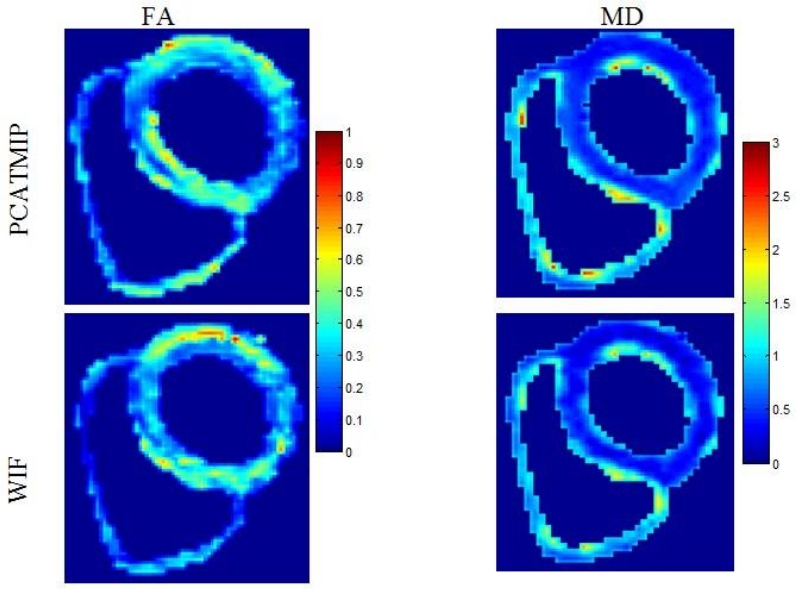

Fig. 5.14. Comparison of FA and MD maps between the two methods.

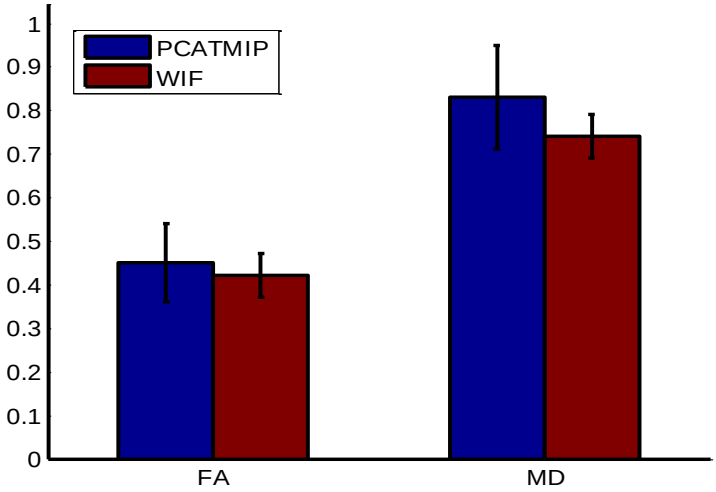

Fig. 5.15. Comparison of FA and MD values between the two methods.

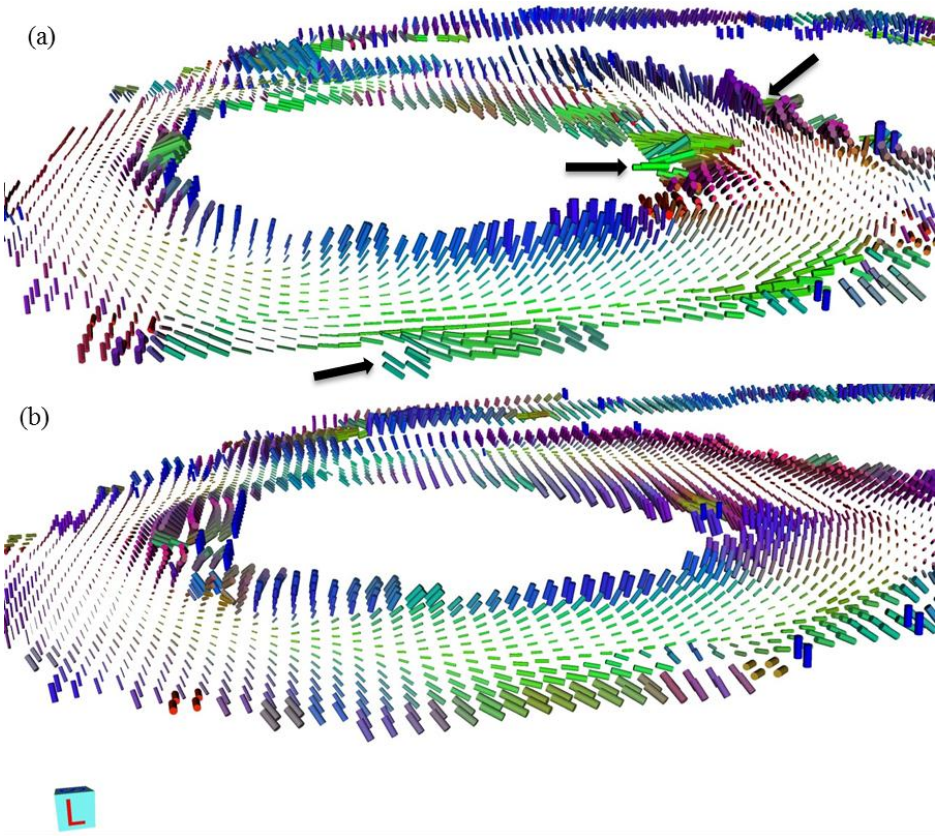

Fig. 5.16. 3D visualizations of tensor field derived from (a) PCATMIP and (b) WIF methods. The helical pattern of the cardiac fiber is clearly depicted by the principal eigenvector. The red, green, and blue colors of the tensors indicate the local orientation of the fiber.

The tensor fields calculated using the two methods are shown in Fig. 5.16. The tensors obtained from wavelet transformation are much ordered and less influenced by the noise, especially in the septum.

Fig. 5.17 shows the fiber tractographies. The fibers obtained using wavelet-based fusion method are smooth that that obtained using PCATMIP, especially on the endocardium and epicardium. Fig. 5.17(d) shows the fiber angles on the epicardium are much negative than that on the epicardium in Fig. 5.17(b). Fiber angles in Fig. 5.17(d) are positive than that in Fig. 5.17(b) on the endocardium.

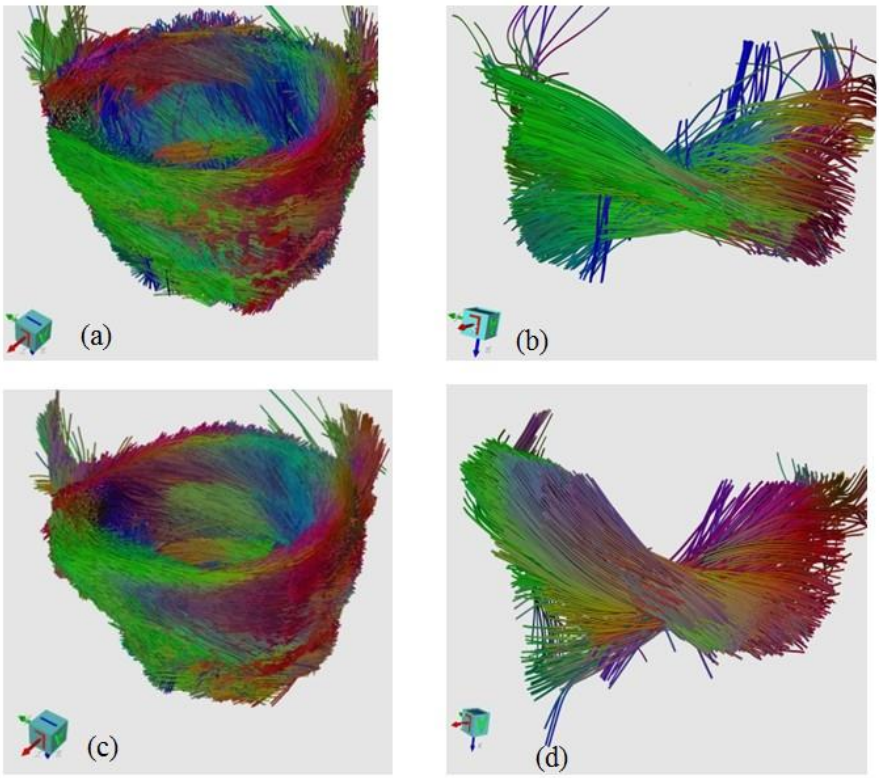

Fig. 5.17. 3D fiber tracts calculated using the two methods. (a) Short-axis view and (b) a shutter fiber tracts using PCATMIP. (c) Short-axis view and (d) a shutter fibers using wavelet transformation.

The fiber shutters located at the lateral wall of the heart comparison betweem the two methods are shown in Fig 5.18. The top row shows the fiber shutters obtained from PCATMIP. The bottom row shows the fibers obtained from WIF method.

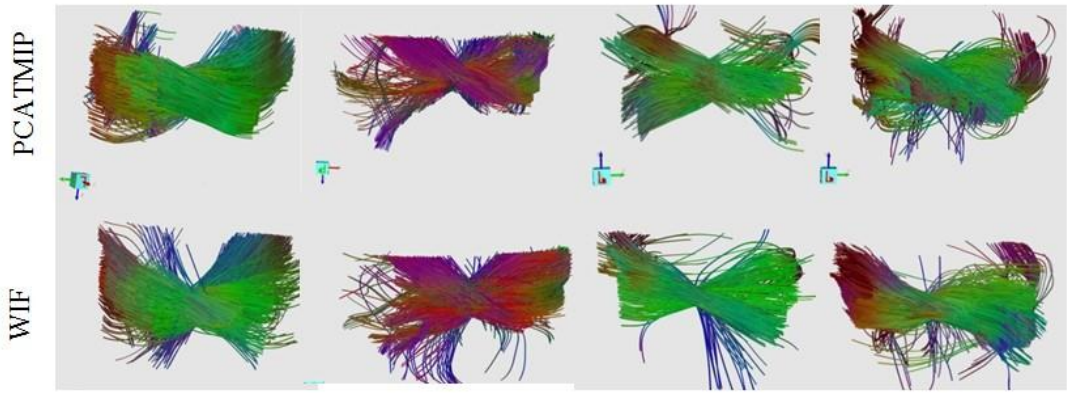

Fig. 5.18. Fiber shutters located at the same location of the same heart comparison betweem PCATMIP and WIF methods. Top: results from PCATMIP method. Bottom: results from WIF method.

5.5 Discussion

This study investigates in vivo human cardiac DTI under free-breathing by using different post-processing methods. It enables us to obtain coherent fiber tractography of the entire heart. And the HA distribution is consistent with the helical structure of the myocardial fibers fibers (Nielles-Vallespin et al. 2012) The results demonstrate the capacity of PCATMIP and WIF methods to preserve the integrity of the directional information contained in the multiple-directional DW acquisitions. WIF combined with the denoising method provides us better fiber tractography.

In vivo DTI of the human heart is challenging due to motion and the intrinsically low SNR of the DW images. Studies from several groups show that in vivo cardiac DTI in human is possible (Wu et al. 2006) and it can be performed in healthy volunteers with good reproducibility. The previous study (Nielles-Vallespin et al. 2012) showed that using STEAM sequence with a biofeedback respiratory gated based approach could minimize the effect of motion for cardiac DTI acquisitions. However, respiratory gated strategies imply increased acquisition time, since only 30-40% of the whole respiratory cycle (Ehman et al. 1984) is actually used for the acquisitions. Moreover, STEAM sequence inherently doubles the total scan time compared with spin-echo sequences since encoding and decoding must take place in two consecutive cardiac cycles. Although cardiac DTI can still be obtained in multiple breath-hold acquisitions, the scan duration of multiple slices imaging is not realistic. Three contiguous slices were acquired in 12-20 mins using both the multiple breath-hold and respiratory-gated approaches. And previous study (Toussaint et al. 2013) showed that the total scan time was 10-15 minutes per DTI slice which depends on navigator efficiency. Therefore, free-breathing acquisition without respiratory gating is preferred to increase acceptance in practice. In our study, the total scan time of multiple shifted TD acquisitions is about 25 minutes for 10 DTI slices covering the entire LV.

Although the multiple shifted TD acquisitions were collected at end diastole where in-plane and through-plane heart motion of the LV were minimal, the cardiac and respiratory motions could not be completely eliminated due to free-breathing acquisitions. Even small differences

in respiratory position due to motion will cause significant misregistration of the images. Image registration is of course mandatory to correct for interscan motion. Image registration is by design only capable of correcting for in-plane motion and cannot compensate for larger through-plane motion, although it may appear to partially compensate. And residual motion can contaminate measurements of cardiac DTI which could result in some loss of coherence of tensor fields between slices. Moreover, the fiber directions were obtained based only on the largest eigenvectors of the diffusion tensors. The diffusion tensors in the heart have ratios of about 1.5-1.8 between axial diffusivity and radial diffusivity. It was more difficult to determine the fiber structure, which was obtained based on the primary eigenvectors because they had magnitudes that were closer to the secondary or tertiary eigenvectors in value (compare this with the brain, which has a difference of a ratio 10 between the primary, and secondary or tertiary eigenvalue). Therefore, a small motion can easily invert the order of the three eigenvectors. And the tensor field is error prone in the sense that the residual motion of the DTI data would influence the direction of the principal eigenvector (Lazar et al. 2003). The streamline tracking by integrating the principle eigenvector from the tensor fields would result in an erroneous fiber structure.

In this work, we adopt two image fusion approaches, which allow us to fuse registered DW images acquired at different TDs. PCATMIP provides the high SNR by picking the highest signal intensity from the input images. While WIF splits the image into sub-images of low and high frequencies, enabling us to easily pick the desired information from each image. Our study has shown that by selecting the wavelet coefficient following the proposed fusion rule can preserve the meaningful diffusion information. Further applying denoising method, this processing scheme can reconstruct a better helical myofiber pattern.

In this study, the images are fused by a two level wavelet decomposition using a Daubechies's wavetlet with eight vanishing moments. The key point here is that we need to find the wavelets suitable for the shape of the heart. Obviously, the Haar is not a good one for our case. Other universal wavelets such as Biorsplines and symlets can also be used in this study. The statistical histograms of the high-frequency bands are compared between different wavelets. The results show that each wavelet has the similar distribution. That is, the distributions of the coefficients are not changed between different wavelets (images with less motion has a larger stand deviation and images with more motion has a smaller stand deviation). Our criterion to choose the high-frequency coefficients are not effected by different wavelets. The spreading of high frequency distribution between different wavelets can be seen in Fig. 5.19. Tensor fields and 3D fibers obtained from different wavelets are illustrated in Fig. 5.20. The tensor is nearly the same. This means that several wavelets can satisfy our fusion requirements in this study.

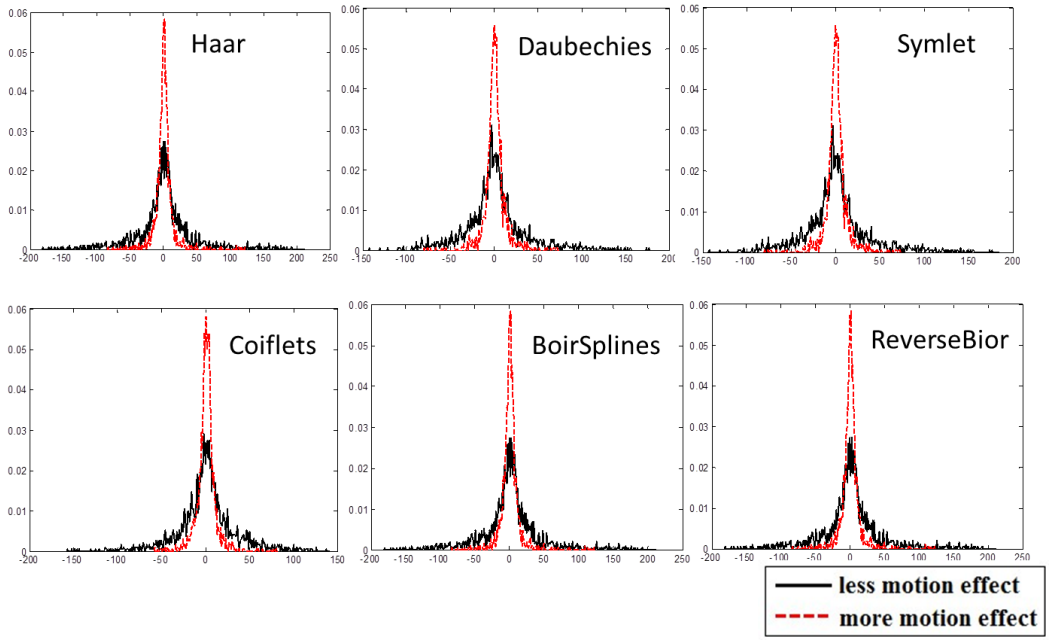

Fig. 5.19. Comparison between different wavelets for the distribution of high-frequency band.

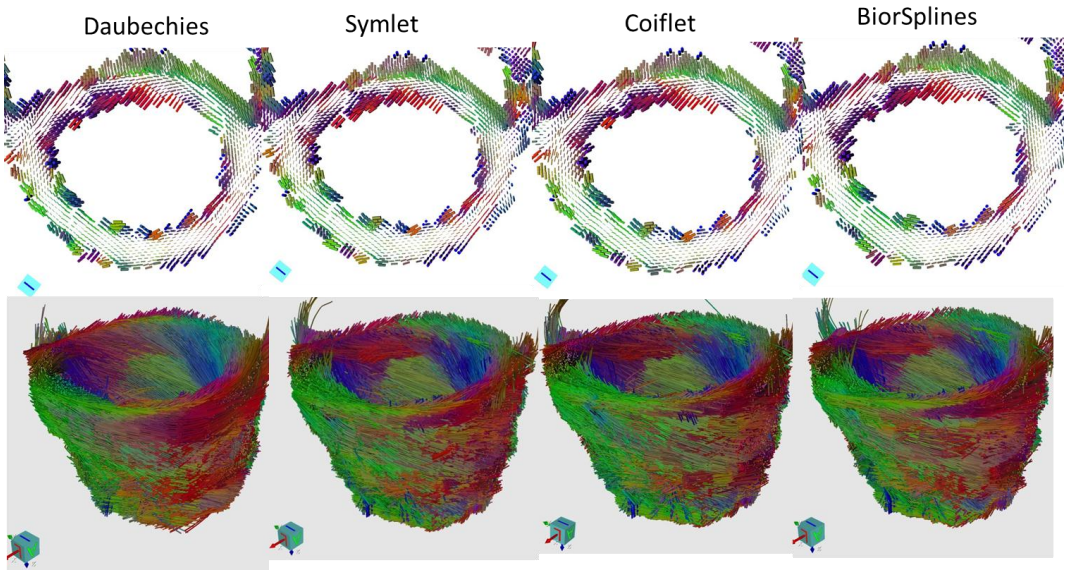

Fig. 5.20. Tensor and fiber comparison between different wavelets reconstruction.

The process of fiber tracking is also sensitive to noise. High frequency noise in the images makes the tensor fields irregular. Therefore, the track that follows a path of fibers might change from one to another neighboring path. One could reduce this noise by several acquisition averages. In our work, we depended on compressing the coefficients in the PCA domain to remove noise. This method models a pixel and its nearest neighbors as a vector variable and performs noise reduction on the vector instead of the single pixel. From the comparison of fiber tracking results from filtered and unfiltered data (Fig. 5.21), the noisy

fiber can be seen in the epicardial and endocardial regions (Fig. 5.21(a)). We can see in Fig. 5.21(b) that the denoising procedure clearly enables the reduction of data errors.

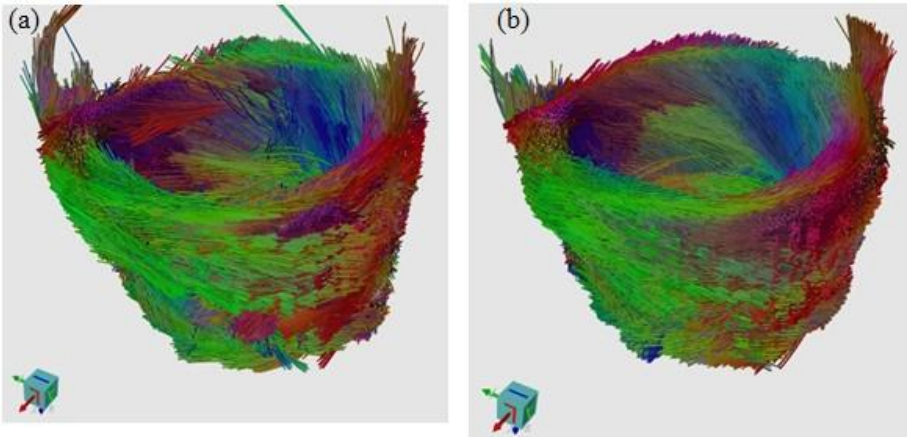

Fig. 5.21. Fiber comparison between unfiltered and filtered data: (a) the fiber tracts for the unfiltered case where some noisy oscillation can be seen in the endocardial and epicardial regions, whereas (b) the strong smooth fiber tracts shows the result for the filtered data.

Even with the motion and noise difficulties in DTI, the cardiac fiber structure in our study compares well with previous ex vivo (Lombaert et al. 2012) and in vivo (Nielles-Vallespin et al. 2012) studies. Our values of myocardial FA ($FA_{PCATMIP}$ =0.45 ± 0.10, FA_{WIF} = 0.42 ± 0.05) and MD ($MD_{PCATMIP}$ = 0.83 ± 0.12 × $10^{-3}mm^2/s$, MD_{WIF} = 0.74 ± 0.05 × $10^{-3}mm^2/s$) are close to a previous study (0.60 ± 0.04 and 0.8 ± 0.2 × $10^{-3}mm^2/s$ for with breath-holding acquisitions and 0.60 ± 0.03 and 0.9 ± 0.2 × $10^{-3}mm^2/s$ for navigator free-breathing acquisitions) in healthy volunteers (Nielles-Vallespin et al. 2012) at 3T scanner. It should be noted that the quantitative results in this study were related to the acquisitions at end diastole. We may consider differences between the data acquired at different cardiac phases. Although not well understood yet, the cardiac fiber architecture in the human heart is dynamic during cardiac cycle and is related with the myocardial strain. While the HA range obtained in this study is approximately from 41° on the endocardium to -34° on the epicardium for PCATMIP and from 44° to -38° for WIF method. WIF method gives a wider HA range which is more in agreement with ex vivo literature (Lombaert et al. 2012). The study reported in (Nielles-Vallespin et al. 2012) of healthy in vivo human hearts showed ranges of HA variations from 22° ± 10° on the endocardium to -17° ± 6° on the epicardium for breath-hold study; from 7° ± 7° on the endocardium to -14° ± 6° on the epicardium for navigated acquisition free-breathing study. While the HA range is slightly narrower than previously-reported ex vivo human cardiac study (HA variations from 66° ± 15° on the endocardium to -41° ± 26° on the epicardium) (Lombaert et al. 2012). We need to consider many factors that may influence the HA range, i.e., in vivo and ex vivo data, data acquired at different cardiac phases, spatial resolution, motion artifacts. The segmentation algorithm used to extract the HA values in each layer imposes averaging, and might account for the narrower range seen in HA. Comparison between different segmentation algorithms to extract robust quantitative HA data will be a very important issue for the future cardiac DTI in the clinical application.

This preliminary experiments show that the approach proposed in this paper (dedicated acquisition method combined with post-processing) has the potential to reduce physiological motion effects. Although this work still has to demonstrate its reproducibility, these preliminary experiments show its feasibility and potential to provide in vivo structure of the normal heart. The technique presented here may have important implications for the in vivo study of heart structure in disease. It does not require reliable navigator synchronization and could be easy to implement. The acquisition of multiple TD dataset leads to a total scan time of about 25 minutes for each volunteer, which is an acceptable acquisition time scale for clinical applications.

5.6 Conclusions

We have proposed the combined use of multiple shifted TD acquisitions and post-processing involving image registration, wavelet-base fusion and PCA domain denoising for in vivo human cardiac DTI with free-breathing. The results showed that such in vivo cardiac DTI is feasible in an acceptable scan time, which suggests its use for studying in vivo cardiac fiber architectures. Meanwhile, to our best knowledge, this is also the first comparative study of the fiber architectures of entire human hearts in vivo with free-breathing obtained using different methods. The obtained HA maps indicate that the myocardial fiber orientation of the LV which shows a circularly symmetric pattern, from about 41° on the endocardium to -34° on the epicardium for PCATMIP and from 44° to -38° for WIF. The fiber tractographies provided by WIF are more continuous than those obtained from PCATMIP, which demonstrates that the WIF processing scheme has a better ability of retrieving diffusion information and removing noise. This new workflow will be used in the future to analyze in vivo fiber architectures and study the impact of cardiovascular disease on the fiber architecture in patients.

PART III

General Conclusion

Chapter 6

General Conclusions and perspectives

6.1 Conclusions

The myocardial structure-function relation is the key to understand the fuctional design of the ventricular myocardium. In this thesis, we have established noninvasive MRI methods to quantify in vivo myocardial diffusion and 3D cardiac fibers. We have presented new methods for diffusion MRI in the beating human heart, which can reduce the effects of resoiratory and cardiac motion. The methods address the problem of motion artefacts of diffusion MRI in the beating heart that was not well addressed by the previously proposed methods in healthy volunteers.

In this thesis, we have proposed a multimodal approach to assessing the effects of cardiac motion on in vivo diffusion tensor parameters of the human heart. With the aid of the ground-truth provided by the combined use of PLI data, simulated DW images and motion information derived from DENSE imaging, the proposed cardiac motion model has been shown to elegantly allow us to investigate the relationship between cardiac motion and in vivo diffusion tensor parameters. We found that cardiac motion resulted in large signal loss in DW images, an overestimation of both FA and MD, and a reduced range of fiber angles between the endocardium and epicardium.

We have investigated in vivo cardiac DTI on healthy volunteers under free-breathing conditions. To our best knowledge, this is the first reconstruction of the entire human heart fiber architecture with free-breathing acquisitions. The combination of dedicated acquisition method, image registration and PCATMIP technique makes it possible to reconstruct myocardial fiber architecture. The combined use of dedicated acquisition method, wavelet-based image fusion method and the PCA denoising technique provides better fiber tracts than PCATMIP. The combined approaches stand as our solution to both reduce motion-induced signal loss and increase final image quality. The obtained HA maps indicate myocardial fiber orientation of the LV, which shows a circularly symmetric pattern. The 3D fiber architecture reproduces the typical helical organization known from in vivo and ex vivo human heart studies. Further use of the proposed in vivo cardiac DTI with free-breathing has the potentiality to become a powerful tool for studying the impact of cardiovascular disease on the fiber architecture in patients.

For the whole chain of our post-processing, we need to do the image registration using MOCO from Siemens or LDDD proposed by Vercauteren, the registration time is about 20 min to finish between DW images at different TD and directions. For the denoising procedure of WIF method, it costs 10 min for each slice. Therefore, the total processing time is about 4 hours for each volunteer including 10 slices covering the whole heart.

6.2 Perspectives

This thesis has enabled our work to range from theoretical study of cardiac motion to in vivo DTI tractography including imaging prcessing. However, this work is far from complete. The study in this thesis found that it is feasible to obtain the entire in vivo cardiac fiber tractography under free-breathing acquisitions in an acceptable scan time (about 25 minutes per volunnteer). But the reproducibility on a large population needs to be further validated.

The workflows in this thesis can reduce motion effects on diffusion parameters. However, they cannot eliminate motion influence. Therefore, a future work would be to acquire DTI data with fewer artefacts through designing appropriate diffusion sequences (e.g. fast imaging method). One of most interesting points is the possibility to access b values (>350 s/mm^2). Consequently, tissue characterization would be more accurate. To date, the resolution of in vivo cardiac DTI is still too low (2.6 mm in the plane and 6-7 mm thickness). Thus, one important work is to develop acquisition technique to obtain higher resolution DTI data (e.g. SSFP sequence). With higher spatial resolution, we can obtain the fiber tracts that could be much coherent with ex vivo histological studies. It should be noted that the quantitative results in this study are related to the acquisitions at end diastole. We may consider differences between the data acquired at different cardiac phases. Indeed, even though not well understood yet, the myofiber re-organization in the in vivo human heart is dynamic during cardiac cycle and is related with the myocardial strain. Therefore, another interesting work in the future would be to perform the time-resolved cardiac tractographies over the entire cardiac cycle. The ability to map myocardial fiber structure and its dynamics, especially combining them with myocardial strain imaging techniques, could provide new insights into the structure-function relationship in the heart, and its changes in the presence of disease.

6.3 Author's publications

Journals

- **Wei HJ**, Viallon M, Delattre BM, Wang LH, Pai VM, Wen H, Xue H, Guetter C, Croisille P, Zhu YM. Assessment of cardiac motion effects on the fiber architecture of the human heart *in vivo*. IEEE TMI 2013; 32(10):1928-1938.
- Delattre BM, Viallon M, **Wei HJ**, Zhu YM, Feiweier, Pai VM, Wen H, Croisille P. In vivo cardiac diffusion-weighted magnetic resonance imaging: quantification of normal perfusion and diffusion coefficients with intravoxel incoherent motion imaging. *Invest Radiol*. 2012; 47(11):662-70.
- Delattre BM, Viallon M, Xue H, Guetter C, Jolly MP, **Wei HJ**, Zhu YM, Feiweier T, Pai VM, Wen H, Croisille P. Intravoxel Incoherent Motion Modeling Applied to Cardiac Diffusion-Weighte MRI: Free-Breathing Acquisitions of Healthy Volunteers. Invest Radiol**.** *submitted.*

Conference Proceedings

- **Wei HJ**, Viallon M, Delattre BM, Pai VM, Wen H, Xue H, Guetter C, Croisille P, Zhu YM. Quantitative analysis of cardiac motion effects on *in vivo* diffusion tensor parameters. ISMRM 21 Scientific Sessions, Salt City, 2013; **Oral presentation #0482.**
- **Wei HJ**, Viallon M, Delattre BM, Pai VM, Wen H, Xue H, Guetter C, Croisille P, Zhu YM. In vivo diffusion tensor imaging of the human heart with free-breathing in healthy subjects. ISMRM 21 Scientific Sessions, Salt City, 2013; **Oral presentation #0575.**
- **Wei HJ**, Viallon M, Delattre BM, Pai VM, Wen H, Xue H, Guetter C, Croisille P, Zhu YM. Quantitative investigation of cardiac motion effects on in vivo diffusion tensor parameters: a simulation study. SCMR, San Francisco, 2013; p244.
- **Wei HJ**, Viallon M, Delattre BM, Pai VM, Wen H, Xue H, Guetter C, Croisille P, Zhu YM. In vivo cardiac diffusion tensor imaging in free-breathing conditions. SCMR, San

Francisco, 2013; p231.

- **Wei HJ**, Viallon M, Delattre BM, Croisille P, Zhu YM. Three-Dimension Fiber Architecture of the Human Heart In Vivo. Imagrie du vivant, Lyon, 2012.
- Delattre BM, Viallon M, **Wei HJ**, Zhu YM, Feiweier, Pai VM, Wen H, Croisille P. Intravoxel Incoherent Motion applied to Cardiac diffusion weighted MRI using breath-hold acquisitions in healthy volunteers. SCMR, Orlando, 2012, p261.
- Delattre BM, Viallon M, Xue H, Jolly MP, Guetter C, **Wei HJ**, Zhu YM, Feiweier, Pai VM, Wen H, Croisille P. Intravoxel incoherent motion modeling applied to cardiac diffusion weighted MRI: towards free breathing acquisition in healthy volunteers. ISMRM 20th Scientific Sessions, Melbourne, 2012.

Bibliographies

Aganj, I. et al., 2012. A 3D wavelet fusion approach for the reconstruction of isotropic-resolution MR images from orthogonal anisotropic-resolution scans. *Magnetic resonance in medicine*, 67(4), pp.1167–1172.

Aletras, A. et al., 1999. DENSE: displacement encoding with stimulated echoes in cardiac functional MRI. *Journal of Magnetic Resonance*, 137(1), pp.247–252.

Arsigny, V. et al., 2006. A log-Euclidean framework for statistics on diffeomorphisms. *Medical image computing and computer-assisted intervention : MICCAI*, 9(Pt 1), pp.924–31.

Assaf, Y. et al., 2008. Three-dimensional water diffusion in impermeable cylindrical tubes: theory versus experiments. *NMR in biomedicine*, 21(8), pp.888–898.

Axer, M. et al., 2011. High-resolution fiber tract reconstruction in the human brain by means of three-dimensional polarized light imaging. *Frontiers in neuroinformatics*, 5, p.34.

Basser, P., 1995. Inferring microstructural features and the physiological. *NMR in biomedicine*, 8, pp.333–344.

Basser, P., Mattiello, J. & LeBihan, D., 1994a. Estimation of the effective self-diffusion tensor from the NMR spin echo. *Journal of magnetic resonance. Series B*, 103(3), pp.247–254.

Basser, P., Mattiello, J. & LeBihan, D., 1994b. MR diffusion tensor spectroscopy and imaging. *Biophysical journal*, 66(1), pp.259–267.

Basser, P. & Pierpaoli, C., 1996. Microstructural and physiological features of tissues elucidated by quantitative-diffusion-tensor MRI. *Journal of Magnetic Resonance. Series B*, 111(3), pp.209–219.

Bernstein, M.A., King, K.F. & Zhou, X.J., 2004. *Handbook of MRI Pulse Sequences*, Burlington: Elsevier Academic Press.

Le Bihan, D. et al., 2001. Diffusion tensor imaging: concepts and applications. *Journal of Magnetic Resonance Imaging*, 13(4), pp.534–546.

Le Bihan, D., 2003. Looking into the functional architecture of the brain with diffusion MRI. *Nature reviews. Neuroscience*, 4(6), pp.469–480.

Le Bihan, D., 1995. Molecular diffusion, tissue microdynamics and microstructure. *NMR in Biomedicine*, 8(7-8), pp.375–386.

Buckberg, G. et al., 2008. Cardiac mechanics revisited: the relationship of cardiac architecture to ventricular function. *Circulation*, 118(24), pp.2571–87.

Callot, V. et al., 2003. In vivo study of microcirculation in canine myocardium using the IVIM method. *Magnetic resonance in medicine*, 50(3), pp.531–40.

Cerqueira, M. et al., 2002. Standardized Myocardial Segmentation and Nomenclature for Tomographic Imaging of the Heart. *Circulation*, 105(4), pp.539–542.

Costa, K., Holmes, J. & Mcculloch, A., 2001. Modelling cardiac mechanical properties in three dimensions. *Philosophical Transactions of the Royal Society of London. Series A: Mathematical, Physical and Engineering Sciences*, 359(1783), pp.1233–1250.

Dammers, J. et al., 2012. Automatic identification of gray and white matter components in polarized light imaging. *NeuroImage*, 59(2), pp.1338–1347.

Dammers, J. et al., 2010. Signal enhancement in polarized light imaging by means of independent component analysis. *NeuroImage*, 49(2), pp.1241–1248.

Delattre, B. et al., 2012. In vivo cardiac diffusion-weighted magnetic resonance imaging: quantification of normal perfusion and diffusion coefficients with intravoxel incoherent motion imaging. *Investigative radiology*, 47(11), pp.662–70.

Delattre, B., 2011. Spatio-temporal Sampling Strategies and Spiral Imaging for Translational Cardiac MRI. *PhD thesis*.

Descoteaux, M. et al., 2011. Multiple q-shell diffusion propagator imaging. *Medical image analysis*, 15(4), pp.603–621.

Dou, J. et al., 2009. Cardiac diffusion MRI without motion effects. *Magnetic resonance in medicine*, 48(1), pp.105–114.

Edelman, R. et al., 1994. In vivo measurement of water diffusion in the human heart. *Magnetic resonance in medicine*, 32(3), pp.423–428.

Ehman, R. et al., 1984. Magnetic resonance imaging with respiratory gating: techniques and advantages. *American journal of roentgenology*, 143(6), pp.1175–82.

Einstein, A., 1956. Investigations on the Theory Brownian Movement. , pp.1–9.

Ennis, D.B. et al., 2008. Accessment of regional systolic and diastolic dysfunction in familial hypertrophic cardiomyopathy using MR tagging. *Magnetic resonance in medicine*, 50(3), pp.638–642.

Farnell, L. & Gibson, W.G., 2004. Monte Carlo simulation of diffusion in a spatially nonhomogeneous medium: correction to the Gaussian steplength. *Journal of Computational Physics*, 198(1), pp.65–79.

Ferreira, P.F. et al., 2013. Cardiovascular magnetic resonance artefacts. *Journal of Cardiovascular Magnetic Resonance*, 15(1), p.41.

Fillard, P., Gerig, G. & Lyon, E., 2003. Analysis Tool for Diffusion Tensor MRI. *Medical Image Computing and Computer-Assisted Intervention:MICCAI*, 2879, pp.967–968.

Firmin, D. & Keegan, J., 2001. Navigator echoes in cardiac magnetic resonance. *Journal of cardiovascular magnetic resonance*, 3(3), pp.183–93.

Fischer, S. et al., 1995. Limitations of stimulated echo acquisition mode (STEAM) techniques in cardiac applications. *Magnetic resonance in medicine*, 34(1), pp.80–91.

Gamper, U., Boesiger, P. & Kozerke, S., 2007. Diffusion imaging of the in vivo heart using spin echoes–considerations on bulk motion sensitivity. *Magnetic resonance in medicine*, 57(2), pp.331–337.

Goshtasby, A. et al., 2007. Pixel- and region-based image fusion with complex wavelets. *Information Fusion*, 8(2), pp.119–130.

Greenbaum, R. et al., 1981. Left ventricular fibre architecture in man. *British heart journal*, 45(3), pp.248–63.

Griswold, M.A. et al., 2002. Generalized autocalibrating partially parallel acquisitions (GRAPPA). *Magnetic resonance in medicine*, 47(6), pp.1202–1210.

Groot, S. & Mazur, P., 1962. *Non-equilibrium thermodynamics*,, Amsterdam: Dover Publications.

Guetter, C. et al., 2011. Efficient symmetric and inverse-consistent deformable registration through interleaved optimization. In *IEEE ISBI*. pp. 590 –593.

Gunatilaka, A.H. & Baertlein, B.A., 2001. Feature-level and decision-level fusion of noncoincidently sampled sensors for land mine detection. *IEEE Transactions on Pattern Analysis and Machine Intelligence*, 23(6), pp.577–589.

Hahn, E., 1950. Spin Echoes. *Physical Review*, 80(4), pp.580–594.

Hashemi, R., 2004. *Mri*,

Van Heeswijk, R.B. et al., 2012. Motion compensation strategies in magnetic resonance imaging. *Critical reviews in biomedical engineering*, 40(2), pp.99–119.

Helm, P. et al., 2005. Ex vivo 3D diffusion tensor imaging and quantification of cardiac laminar structure. *Magnetic resonance in medicine*, 54(4), pp.850–9.

Hooks, D. et al., 2002. Cardiac microstructure: implications for electrical propagation and defibrillation in the heart. *Circulation research*, 91(4), pp.331–338.

Hooks, D. et al., 2007. Laminar arrangement of ventricular myocytes influences electrical behavior of the heart. *Circulation research*, 101(10), pp.103–12.

Hüppi, P.S. & Dubois, J., 2006. Diffusion tensor imaging of brain development. *Seminars in fetal & neonatal medicine*, 11(6), pp.489–497.

Jouk, P. et al., 2007. Analysis of the fiber architecture of the heart by quantitative polarized light microscopy. Accuracy, limitations and contribution to the study of the fiber architecture of the ventricles during fetal and neonatal life. *European journal of cardio-thoracic surgery*, 31(5), pp.915–21.

Jouk, P. et al., 1995. Mapping of the orientation of myocardial cells by means of polarized light and confocal scanning laser microscopy. *Microscopy research and technique*, 30(6), pp.480–490.

Kingsley, P.B., 2006. Introduction to diffusion tensor imaging mathematics: Part II. Anisotropy, diffusion • weighting factors, and gradient encoding schemes. *Concepts in Magnetic Resonance Part A*, 28A(2), pp.123–154.

Knight, F.B., 1961. On The Random Walk And Brownian Motion. *The American Mathematical Monthly*, 54(7), pp.369–391.

Landman, B. et al., 2008. Diffusion tensor imaging at low SNR: nonmonotonic behaviors of tensor contrasts. *Magnetic resonance imaging*, 26(6), pp.790–800.

Langlet, C., 2006. Geometric and Variational Methods for Diffusion Tensor MRI Processing. *PhD thesis*.

Larsen, L. et al., 2007. Polarized light imaging of white matter architecture. *Microscopy research and technique*, 70(10), pp.851–63.

Lazar, M. et al., 2003. White matter tractography using diffusion tensor deflection. *Human brain mapping*, 18(4), pp.306–321.

Lee, V. et al., 2002. Cardiac Function: MR Evaluation in One Breath Hold with Real-time True Fast Imaging with Steady-State Precession. *Radiology*, 222(3), pp.835–842.

Legrice, I. et al., 1995. Laminar structure of the heart: ventricular myocyte arrangement and connective tissue architecture in the dog. *Am J Physiol Heart Circ Physiol*, 269(2), pp.H571–582.

Legrice, I., Hunter, P. & Smaill, B., 1997. Laminar structure of the heart: a mathematical model. *Am J Physiol Heart Circ Physiol*, 272(5), pp.H2466–2476.

Levitt, M.H., 2002. *Spin dynamics: basics of nuclear magnetic resonance.* 2nd ed., Wiley.

Ling, J. et al., 2012. Head injury or head motion? Assessment and quantification of motion artifacts in diffusion tensor imaging studies. *Human Brain Mapping*, 33(1), pp.50–62.

Lombaert, H. et al., 2012. Human Atlas of the Cardiac Fiber Architecture: Study on a Healthy Population. *IEEE Transactions on Medical Imaging*, 31(7), pp.1436–1447.

Mall, F.P., 1911. On the muscular architecture of the ventricles of the human heart. *American Journal of Anatomy*, 11(3), pp.211–266.

McGill, L. et al., 2012. Reproducibility of in-vivo diffusion tensor cardiovascular magnetic resonance in hypertrophic cardiomyopathy. *Journal of cardiovascular magnetic resonance*, 14, pp.15–22.

Moratal, D. et al., 2008. k-Space tutorial: an MRI educational tool for a better understanding of k-space. *Biomedical imaging and intervention journal*, 4(1), p.e15.

Mori, S. et al., 2002. Imaging Cortical Association Tracts in the Human Brain Using Diffusion-Tensor-Based Axonal Tracking. *Magnetic resonance in medicine*, 223, pp.215–223.

Mori, S. & Barker, P.B., 1999. Diffusion Magnetic Resonance Imaging : its principle and applications. *The anatomical record.*, 257, pp.102–109.

Nielles-Vallespin, S. et al., 2012. In vivo diffusion tensor MRI of the human heart: Reproducibility of breath-hold and navigator-based approaches. *Magnetic resonance in medicine*.

Nielles-vallespin, S. et al., 2013. Time-resolved In Vivo Cardiac Diffusion Tensor MRI of the Human Heart. *ISMRM*, 347(1969), pp.1–1.

Pai, V. et al., 2010. PCATMIP: Enhancing signal intensity in diffusion-weighted magnetic resonance imaging. *Magnetic resonance in medicine*, 65, pp.1611–1619.

Palm, C. et al., 2010. Towards Ultra-High Resolution Fibre Tract Mapping of the Human Brain - Registration of Polarised Light Images and Reorientation of Fibre Vectors. *Frontiers in human neuroscience*, 4, pp.1–16.

Park, H., Kim, D. & Cho, Z., 1987. Gradient reversal technique and its applications to chemical-shift-related NMR imaging. *Magnetic resonance in medicine*, 4(6), pp.526–536.

Piella, G., 2003. A general framework for multiresolution image fusion: from pixels to regions. *Information Fusion*, 4(4), pp.259–280.

Pierpaoli, C. & Basser, P.J., 1996. Toward a quantitative assessment of diffusion anisotropy. *Magnetic resonance in medicine*, 36(6), pp.893–906.

Price, W.S., 1997. Pulsed- field gradient nuclear magnetic resonance as a tool for studying translational diffusion: Part 1. Basic theory. *Concepts in Magnetic Resonance*, 9(5), pp.299–336.

Price, W.S. & Price, W.S., 1998. Pulsed-field gradient nuclear magnetic resonance as a tool for studying translational diffusion. Part 2. Experimental aspects. *Concepts in Magnetic Resonance*, 10(4), pp.197–237.

Rapacchi, S. et al., 2009. In vivo cardiac NMR Diffusion Weighted Imaging (DWI) for the human heart : tackling motion issue with temporal Maximum Intensity Projection (tMIP) -DWI and first results in humans. In *Proc. Intl. Soc. Mag. Reson. Med.* Hawaii, USA, p. 4718.

Rapacchi, S. et al., 2011. Low b-value diffusion-weighted cardiac magnetic resonance imaging: initial results in humans using an optimal time-window imaging approach. *Investigative Radiology*, 46(12), pp.751–758.

Reese, T. et al., 1995. Imaging myocardial fiber architecture in vivo with magnetic resonance. *Magnetic resonance in medicine*, 34(6), pp.786–791.

Reese, T., Wedeen, V. & Weisskoff, R., 1996. Measuring Diffusion in the Presence of Material Strain. *Journal of Magnetic Resonance. Series B*, 112(3), pp.253–258.

Roger, V.L. et al., 2011. Heart disease and stroke statistics--2011 update: a report from the American Heart Association. *Circulation*, 123(4), pp.e18–e209.

Rushmer, R., CRYSTAL, D. & WAGNER, C., 1953. The Functional Anatomy of Ventricular Contraction. *Circulation Research*, 1(2), pp.162–170.

Rüssel, I. et al., 2009. Left ventricular torsion: an expanding role in the analysis of myocardial dysfunction. *JACC. Cardiovascular imaging*, 2(5), pp.648–55.

Schülen, V. et al., 1996. Evaluation of K-space segmented cine sequences for fast functional cardiac imaging. *Investigative radiology*, 31(8), pp.512–22.

Skare, S. et al., 2000. Noise considerations in the determination of diffusion tensor anisotropy. *Magnetic resonance imaging*, 18(6), pp.659–669.

Sosnovik, D.E. et al., 2009. Diffusion MR tractography of the heart. *Journal of cardiovascular magnetic resonance*, 11, p.47.

Stanisz, G.J. et al., 2005. T1, T2 Relaxation and Magnetization Transfer in Tissue at 3T. *Magnetic resonance in medicine*, 512(4), pp.507–512.

Stejskal, E.O. & Tanner, J.E., 1965. Spin Diffusion Measurements: Spin Echoes in the Presence of a Time-Dependent Field Gradient. *The Journal of Chemical Physics*, 42(1), pp.288–293.

Streeter, D. et al., 1969. Fiber Orientation in the Canine Left Ventricle during Diastole and Systole. *Circulation Research*, 24(3), pp.339–347.

Streeter, D., 1979. Gross Morphology and Fiber Geometry of the Heart. In *In handbook of physiology:The cardiovascular system*. USA: Oxford University Press, pp. 61 – 112.

Summers, P. et al., 2006. A preliminary study of the effects of trigger timing on diffusion tensor imaging of the human spinal cord. *American journal of neuroradiology*, 27(9), pp.1952–1961.

Tian, J. et al., 2011. Multi-focus image fusion using a bilateral gradient-based sharpness criterion. *Optics Communications*, 284(1), pp.80–87.

Tijssen, R.H.N., Jansen, J.F.A. & Backes, W.H., 2009. Assessing and minimizing the effects of noise and motion in clinical DTI at 3 T. *Human Brain Mapping*, 30(8), pp.2641–2655.

Torrent-Guasp, F., 1973. *The cardiac muscle*, Madrid: Guadarrama.

Torrent-Guasp, F. et al., 2005. Towards new understanding of the heart structure and function. *European journal of cardio-thoracic surgery*, 27(2), pp.191–201.

Torrey, H., 1956. Bloch Equations with Diffusion Terms. *Physical Review*, 104(3), pp.563–565.

Toussaint, N. et al., 2010. In vivo human 3D cardiac fibre architecture: reconstruction using curvilinear interpolation of diffusion tensor images. *Medical Image Computing and Computer-Assisted Intervention: MICCAI* ., 13(Pt 1), pp.418–425.

Toussaint, N. et al., 2013. In Vivo Human Cardiac Fibre Architecture Estimation using Shape-based Diffusion Tensor Processing. *Medical Image Analysis*, 17(8), pp.1243–1255.

Tseng, W. et al., 1999. Cardiac diffusion tensor MRI in vivo without strain correction. *Magnetic resonance in medicineedicine*, 42(2), pp.393–403.

Tseng, W. et al., 2006. Imaging myocardial fiber disarray and intramural strain hypokinesis in hypertrophic cardiomyopathy with MRI. *Journal of Magnetic Resonance Imaging*, 23(1), pp.1–8.

Tseng, W. et al., 2000. Myocardial fiber shortening in humans: initial results of MR imaging. *Radiology*, 216(1), pp.128–139.

Vercauteren, T. et al., 2009. Diffeomorphic demons: efficient non-parametric image registration. *NeuroImage*, 45(1), pp.S61–72.

Viallon, M. et al., 2011. Head-to-head comparison of eight late gadolinium-enhanced cardiac MR (LGE CMR) sequences at 1.5 tesla: from bench to bedside. *Journal of magnetic resonance imaging*, 34(6), pp.1374–87.

Wang, L. et al., 2012. Multiscale modeling and simulation of the cardiac fiber architecture for DMRI. *IEEE Transactions on Bio-Medical Engineering*, 59(1), pp.16–19.

Wu, M. et al., 2006. Diffusion tensor magnetic resonance imaging mapping the fiber architecture remodeling in human myocardium after infarction: correlation with viability and wall motion. *Circulation*, 114(10), pp.1036–45.

Wu, M. et al., 2009. Sequential changes of myocardial microstructure in patients postmyocardial infarction by diffusion-tensor cardiac MR: correlation with left ventricular structure and function. *Circulation. Cardiovascular imaging*, 2(1), pp.32–40.

Xu, D. et al., 2003. Spatial normalization of diffusion tensor fields. *Magnetic resonance in medicine*, 50(1), pp.175–82.

Yang, Y. et al., 2010. Medical image fusion via an effective wavelet-based approach. *EURASIP J. Adv. Signal Process*, 2010, pp.44:1–44:13.

Zhang, L. et al., 2010. Two-stage image denoising by principal component analysis with local pixel grouping. *Pattern Recogn.*, 43(4), pp.1531–1549.

Zhukov, L. & Barr, A.H., 2003. Heart-muscle fiber reconstruction from diffusion tensor MRI. *In proceeding of: Visualization, 2003. VIS 2003. IEEE*, (4), pp.597–602.

FOLIO ADMINISTRATIF

THESE SOUTENUE DEVANT L'INSTITUT NATIONAL DES SCIENCES APPLIQUEES DE LYON

NOM : WEI **DATE de SOUTENANCE :** 20/11/2013

Prénoms : Hongjiang

TITRE : In vivo diffusion tensor imaging (DTI) for the human heart under free-breathing conditions

NATURE : Doctorat **Numéro d'ordre :** 2013-xxxx-xxxx

École doctorale : École Doctorale Électronique, Électrotechnique, Automatique

Spécialité : Image et System

RESUME :L'orientation des fibres myocardiaque est à la base du comportement électro-mécanique du cœur, et connue pour être altérée dans diverses maladies cardiaques telles que la cardiopathie ischémique et l'hypertrophie ventriculaire. Cette thèse porte principalement sur l'imagerie in vivo du tenseur de diffusion (diffusion tensor imaging—DTI) en vue d'obtenir la structure des fibres myocardiques du cœur humain dans des conditions de respiration libre. L'utilisation de DTI pour l'étude du cœur humain in vivo est un grand défi en raison du mouvement cardiaque. En particulier, l'acquisition DTI avec respiration libre sans recourir au gating respiratoire est très difficile à cause des mouvements à a fois respiratoire et cardiaque. Pour aborder ce problème, nous proposons de nouvelles approches consistant à combiner des acquisitions à retards de déclenchement multiples (trigger delay-TD) et des méthodes de post-traitement. D'abord, nous réalisons des acquisitions avec multiples TD décalés en fin de diastole. Ensuite, nous développons deux méthodes de post-traitement. La première méthode s'attaque au problème d'effets de mouvement physiologique sur DTI cardiaque in vivo en utilisant les techniques de recalage et de PCATMIP (Principal Components Analysis filtering and Temporal Maximum Intensity Projection). La deuxième méthode traite le problème de mouvement par l'utilisation d'un algorithme de fusion d'images basé sur l'ondelette (wavelet-based image fusion—WIF) et d'une technique de débruitage PCA (Principal Components Analysis). Enfin, une comparaison des mesures DTI entre la méthode PCATMIP et la méthode WIF est réalisée ; les champs de tenseurs sont calculés, à partir desquels les propriétés de l'architecture des fibres in vivo sont comparées. Les résultats montrent qu'en utilisant les approches proposées, il est possible d'étudier l'impact du mouvement cardiaque sur les paramètres de tenseur de diffusion, et d'explorer les relations sous-jacentes entre les propriétés de tenseur de diffusion mesurées et le mouvement cardiaque. Nous trouvons aussi que la combinaison des acqusiitions avec des TD multiples décalés and des post-traitements d'images peut compenser les effets de mouvement physiologique, ce qui permet d'obtenir l'architecture 3D du cœur humain dans des conditions de respiration libre. Les résultats suggèrent de nouvelles solutions au problème de perte du signal due au mouvement, qui sont prometteuses pour obtenir les propriétés de l'architecture des fibres myocardiques du cœur humain in vivo, dans des conditions cliniques.

MOTS-CLES :

L'imagerie de lumière polarisée; L'orientation de fibre; L'IRM de diffusion ; Cœur ; *in vivo*

Laboratoire (s) de recherche: Creatis (CNRS UMR 5520, INSERM U1044)

Directeur de thèse : ZHU Yuemin

Président de jury :

Composition du jury :

FROUIN Frédérique, LIU Wanyu, ROUGON Nicolas, CROISILLE Pierre, FELBLINGER Jacques, VIALLON Magalie, ZHU Yuemin